# Nanoelectronics and Its New Materials – A NEW ERA OF NANOSCIENCE

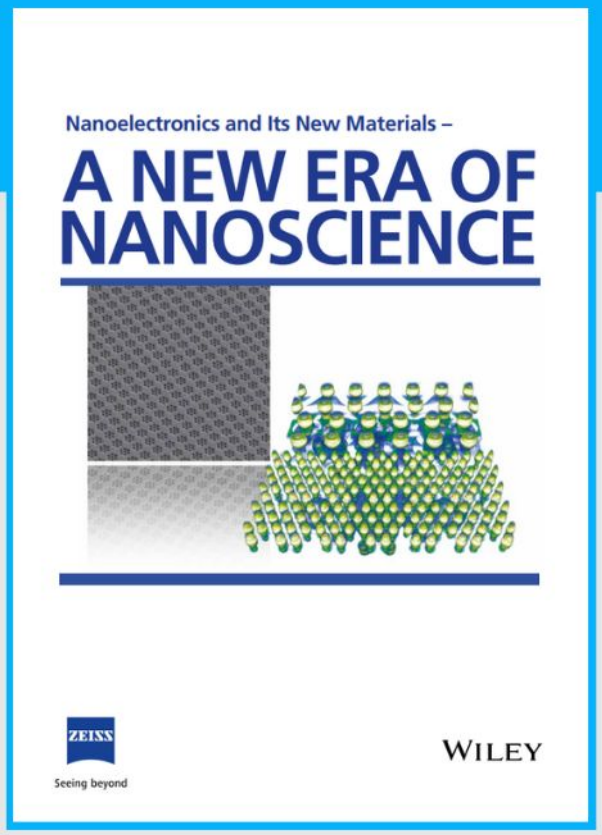


**Discover the recent advances in electronics research and fundamental nanoscience.**

Nanotechnology has become the driving force behind breakthroughs in engineering, materials science, physics, chemistry, and biological sciences. In this compendium, we delve into a wide range of novel applications that highlight recent advances in electronics research and fundamental nanoscience. From surface analysis and defect detection to tailored optical functionality and transparent nanowire electrodes, this eBook covers key topics that will revolutionize the future of electronics.

To get your hands on this valuable resource and unleash the power of nanotechnology, simply download the eBook now. Stay ahead of the curve and embrace the future of electronics with nanoscience as your guide.

ZEISS

Seeing beyond

WILEY

Check for updates



ADVANCED FUNCTIONAL MATERIALS
www.afm-journal.de

# A Review of Acoustic Devices Based on Suspended 2D Materials and Their Composites

*Zhaoyi Wan, Huazhan Liu, Yuebin Zheng, Yuhua Ma, Kehai Liu, Xu Zhou,* Chang Liu,* Kaihui Liu,* and Enge Wang*

**Acoustic devices play an increasingly important role in modern society for information technology and intelligent systems, and recently significant progress has been made in the development of communication, sensing, and energy transduction applications. However, conventional material systems, such as polymers, metals and silicon, show limitations to fulfill the evolving requirements for high-performance acoustic devices of small size, low power consumption, and multifunctional capabilities. 2D materials hold the promise in overcoming the development bottleneck of acoustic devices aforementioned, given their atomic-thin thickness, extensive surface area, superior physical properties, and remarkable layer-stacking tunability. By suspending the 2D materials, mechanical and thermal disruption from substrate will be eliminated, which will enable the development of new classes of acoustic devices with unprecedented sensitivity and accuracy. In this review, the recent progress of acoustic devices based on suspended 2D materials and their composites, especially applications in the audio frequency, static pressure, and ultrasonic frequency range, is briefly summarized, emphasizing the advantageous properties of suspended 2D materials and related outstanding device performance. Together with the development of 2D membrane synthesis, transfer, as well as microelectromechanical fabrication process, suspended 2D materials will shed light on the next-generation high-performance acoustic devices.**

## 1. Introduction

An acoustic wave is a type of mechanical wave that carries energy and information through the vibration of a medium with the motions of atoms and molecules. Acoustic devices, consisting of apparatus for emitting and receiving acoustic waves, play a crucial role in various fields, such as microphones,[1–7] speakers,[8–14] hearing aids,[15] industrial monitoring,[16] oceanography[17] and ultrasonic imaging systems.[18] In the realm of information technology and intelligent systems, there is also a pressing demand for acoustic devices that possess high performance, small size, low power consumption, and multifunctional capabilities.[19–22] In recent years, significant progress has been made in the development of acoustic devices, thanks to the exploration of various diaphragm materials,[23] the optimization of design[24] and fabrication techniques.[25] However, conventional material systems, including metals, polymers, ceramics, and silicon, show difficulties to fulfill the evolving

Z. Wan, C. Liu, E. Wang
International Centre for Quantum Materials
Collaborative Innovation Centre of Quantum Matter
Peking University
Beijing 100871, China
E-mail: liu.chang@pku.edu.cn

H. Liu, K. Liu
State Key Laboratory for Mesoscopic Physics
Frontiers Science Centre for Nano-optoelectronics
School of Physics
Peking University
Beijing 100871, China
E-mail: khliu@pku.edu.cn

The ORCID identification number(s) for the author(s) of this article can be found under https://doi.org/10.1002/adfm.202303519

**DOI: 10.1002/adfm.202303519**

Y. Zheng, K. Liu, K. Liu, E. Wang
Songshan Lake Materials Laboratory
Institute of Physics
Chinese Academy of Sciences
Dongguan 523808, China

Y. Ma, X. Zhou
Guangdong Provincial Key Laboratory of Quantum Engineering and Quantum Materials
School of Physics
South China Normal University
Guangzhou 510006, China
E-mail: xuzhou2020@m.scnu.edu.cn

K. Liu
Peking University Yangtze Delta Institute of Optoelectronics
Nantong 226000, China

E. Wang
School of Physics
Liaoning University
Shenyang 110036, China

 © 2023 Wiley-VCH GmbH

16163028, 0, Downloaded from https://onlinelibrary.wiley.com/doi/10.1002/adfm.202303519 by Peking University Health, Wiley Online Library on [07/10/2023]. See the Terms and Conditions (https://onlinelibrary.wiley.com/terms-and-conditions) on Wiley Online Library for rules of use; OA articles are governed by the applicable Creative Commons License

requirements of next-generation acoustic devices. The physical properties of the material directly determine the operational principle and performance characteristics of acoustic devices, encompassing parameters such as Young's modulus, mechanical strength, dielectric constant, carrier mobility and heat capacity, etc. The utilization of conventional millimeter-thick materials is impeded by their high area density and damping characteristics, posing constraints on the improvement of critical performance indicators, such as response bandwidth and signal distortion.[26] The scaling down of device dimensions usually leads to a rise in thermal noise, further limiting their sensitivity of acoustic devices.[27]

2D materials hold immense promise in tackling the aforementioned challenges, given their atomic layer thickness, extensive surface area, superior physical properties, and remarkable layer-stacking tunability.[28–30] Ultrathin 2D materials exhibit unique characteristics that distinguish them from their bulk counterparts, which have enabled the development of new classes of acoustic devices with unprecedented sensitivity and accuracy.[28] Specifically, their large lateral size and ultrathin thickness result in ultrahigh specific surface area, making them well-suited for sensing applications.[31] Especially for graphene, the high Young's modulus and low absorption enable the fabrication of flexible and transparent acoustic devices. The extremely light weight, combined with a low-stress state, enables almost effortless vibration in response to sound waves in the air, which yields a flat and broad frequency response, making it a promising candidate for an ideal microphone diaphragm. Due to the weak van der Waals (vdW) interlayer interaction, the convenient manipulation of layer-stacking of 2D materials has positioned them as potential candidates for tunable electromechanical nanoresonators.[32] In addition, the ultrathin nature of 2D materials allows them to be integrated with modern silicon-based technologies such as the complementary metal oxide semiconductor (CMOS) fabrication process. Furthermore, compared with substrate supported material, suspended 2D materials yield superior advantages in terms of deformation and transduction mechanisms for acoustic devices.[33] Upon eliminating the interaction with the substrate (such as mechanical and thermal disruption), the substrate no longer hinders the material's vibration, deformation, and recovery process, thereby enabling the suspended material to respond independently and realize its full potential for high-performance acoustic devices.[29]

In this review, we summarize the progress of acoustic devices based on suspended 2D materials and their composites, emphasizing the advantageous properties of suspended 2D membranes and related outstanding device performance (**Figure 1**). We start by briefly introducing the synthesis and suspension techniques for the 2D membrane. Then applications in different operating frequency ranges have been reviewed in detail. Although acoustic devices that operate at different frequency ranges may share common underlying principles, the manner in which 2D materials behave as sensitive vibrational elements varies considerably across the quasi-static to ultrasonic range. Therefore, the properties of interest for 2D materials also differ markedly. Specifically, in the audio frequency range, the use of suspended 2D materials as the diaphragms of speakers/microphones results in excellent performances such as high sound pressure level (SPL), high sensitivity, broad bandwidth, flat response and high signal-to-noise ratio, etc. As for static pressure sensors, suspended 2D materials can be utilized as the deformable membrane to achieve ultrahigh sensitivity per unit area and improved response linearity through low-cost array design. In the ultrasonic frequency range, suspended 2D materials possess advantages in high resonance frequency, high quality factor, and remarkable tunability for nanoelectromechanical (NEMS) resonators, which can be utilized in mass, thermal and other advanced sensing technologies. Meanwhile, we also survey some relevant progress based on 2D material composites, which can address some of the challenges existing in current acoustic devices based on pure 2D material, such as the imperfect fabrication process, in order to enhance the performance of relative acoustic devices.

## 2. Suspension of 2D Membranes and Device Fabrication

High quality vibrating membranes play an essential role in acoustic devices and directly influences their acoustic performance. Nowadays, various kinds of new diaphragm materials have been utilized in order to enhance the stability and sensitivity of acoustic devices, among which the high performance 2D materials have been explored in detail, accompany with the development of synthesis methods such as chemical vapor deposition method (CVD), physical vapor deposition method (PVD), molecular beam epitaxial (MBE), atomic layer deposition and slurry method, etc. CVD and slurry methods are commonly utilized due to their potential for large-scale synthesis with lower costs, which will be introduced in the following sections detailly. After the synthesis, the membrane should be transferred with proper methods to avoid wrinkles and cracks, and suspended as vibrating diaphragms for acoustic devices. Advanced transfer techniques such as the "stamp" transfer (also known as the "dry method") and the polymer assisted transfer (also known as the "wet method") have been developed to achieve either on-chip integration with miniaturized electronics or large area suspended membrane-based acoustic devices. Here we briefly introduce the synthesis of large area 2D materials membranes and transfer methods with up-to-date progress and discuss how they can be integrated with acoustic devices. Importantly, we provide a thorough overview of prestress regulation techniques for suspended 2D material-based membranes. These techniques represent the latest advancements and have received increasing attention in previous work, which indeed plays a crucial role in enhancing the performance of advanced acoustic devices, including sensitivity, bandwidth, stability, and service life. We will discuss them detailly in Section 2.4.

### 2.1. Synthesis of 2D Material Based Membranes

The CVD method is a technology that utilizes the vapor phase reaction containing target chemical elements to generate thin films on the substrate, possessing the advantages of simplicity, controllability as well as cost-efficiency for production of large area 2D material films.[34–37] Nowadays, the growth of large area graphene on metal substrates (such as copper (Cu)) has been realized. Researchers have found that domains of graphene grown

 © 2023 Wiley-VCH GmbH

16163028, 0, Downloaded from https://onlinelibrary.wiley.com/doi/10.1002/adfm.202303519 by Peking University Health, Wiley Online Library on [07/10/2023]. See the Terms and Conditions (https://onlinelibrary.wiley.com/terms-and-conditions) on Wiley Online Library for rules of use; OA articles are governed by the applicable Creative Commons License

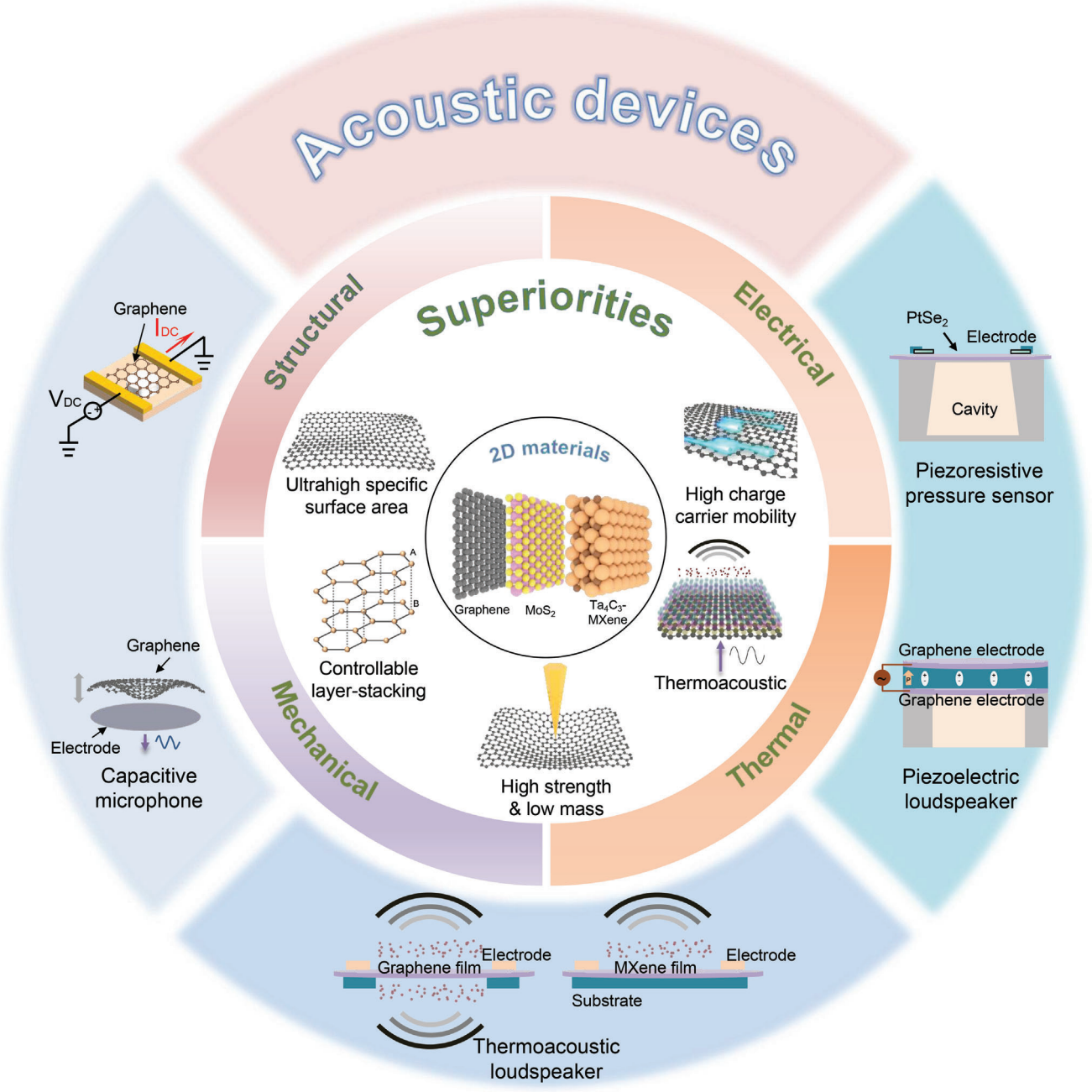


**Figure 1.** Overview of the superior properties and corresponding acoustic devices associated with suspended 2D materials and their composites.

on Cu(111) surface could be directed with the same orientation and seamlessly stitched into large area single crystal graphene sheet.[38–40] Typically, Xu et al. referred this method and successfully manufactured a single crystal graphene sheet on annealed Cu(111) surface with a size of more than half a meter (**Figure 2**a shows the mechanism of the process).[41] The growth of graphene on other metal substrates has also been realized using similar methods.[42–45] Attempts of graphene growth on semiconductor or insulator substrates such as silicon, silicon dioxide or germanium are also explored in detail,[46–49] making it possible for the in-situ growth of graphene films on miniaturized electronics devices. Moreover, large area monolayer and multilayer transition metal dichalcogenides (TMDs) such as $MoS_2$ and $WSe_2$ have been synthesized using the CVD method. In 2017, Yu et al. succeeded in growing monolayer $MoS_2$ on a 2-inch sapphire substrate using the step-edge-guided CVD method (Figure 2c).[50] Li et al. and Wang et al. further developed this method and realized wafer-scale growth of single crystal TMDs.[51,52] These wafer-scale synthesis methods are conducive to the production of large area membranes used for acoustic diaphragms. Direct synthesis of suspended TMDs membranes has also been realized recently,[53] which effectively avoids pollution and

 © 2023 Wiley-VCH GmbH

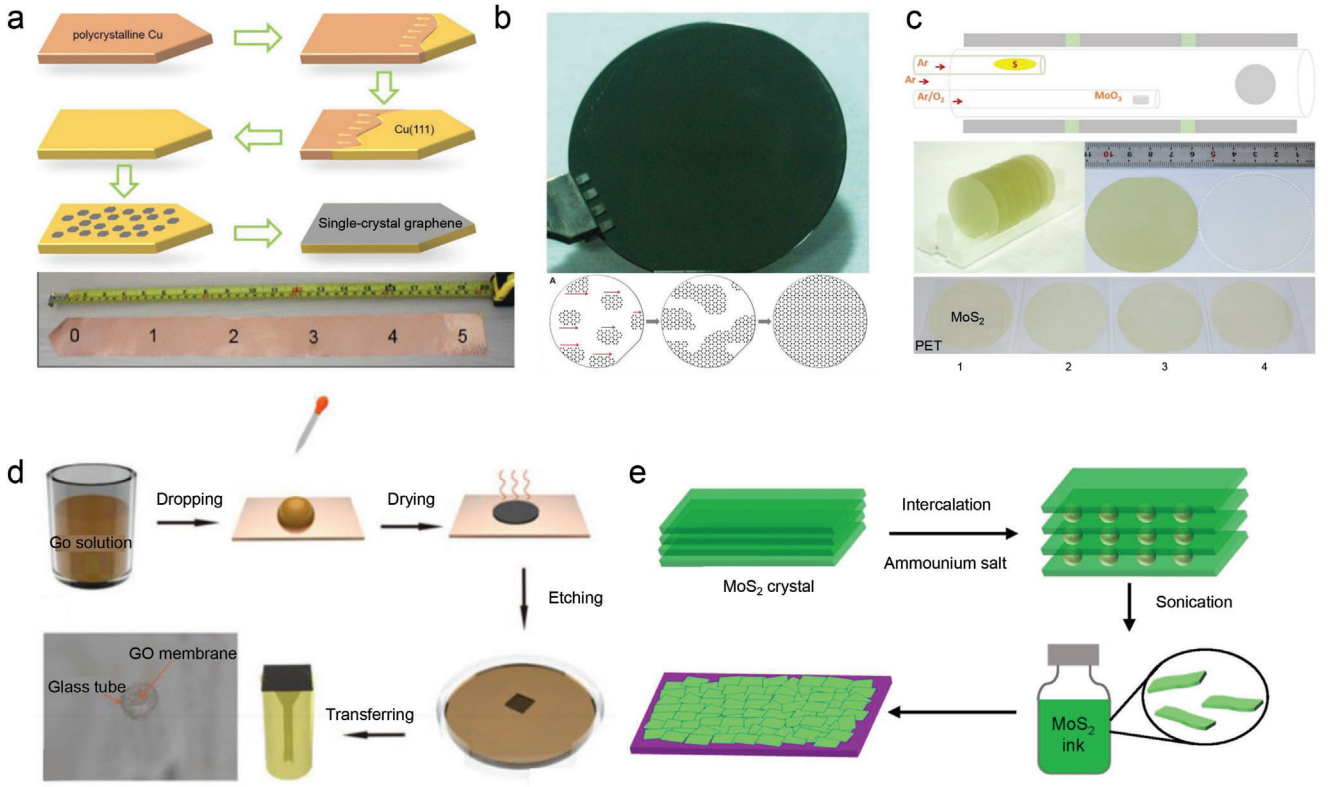


**Figure 2.** Synthesis of 2D materials by different methods. a) Process of monolayer graphene growing on Cu(111) foil by CVD. Length of the single crystal graphene is meter-scale and it is limited by the current furnace tube and the length of the Cu foil. Reproduced with permission.[41] Copyright 2017, Elsevier B.V. and Science China Press. b) Monolayer graphene grown on germanium substrate by CVD. Reproduced with permission.[49] Copyright 2014, The American Association for the Advancement of Science. c) Illustration of the chemical vapor deposition furnace and growing process of monolayer $MoS_2$. Bottom illustration shows the stacked $MoS_2$ of monolayer, bilayer, trilayer and four layers. Reproduced with permission.[50] Copyright 2017, American Chemical Society. d) Synthesis and transferring process of graphene oxide membrane. The transferred GO membrane and the fiber composed a highly sensitive fiber-optic microphone. Reproduced with permission.[54] Copyright 2017, IEEE. e) Intercalation of bulk $MoS_2$ crystal and film made by slurry method. The flakes stack on each other and the van der Waals interaction makes the film highly stretchable. Reproduced with permission.[61] Copyright 2018, Springer Nature Limited.

mechanical damages during the transfer process for suspension of the acoustic diaphragm.

As for slurry method, the slurry containing 2D material flakes, such as graphene and TMDs, can be directly spin-coated into large area membranes.[54–57] These slurry can be prepared by oxidation[58] or intercalation of 2D materials including graphite, $MoS_2$, $WS_2$, and etc.[59–61] Graphene oxide (GO) and other graphene derivative are typical materials, which could be made into membranes utilizing slurry methods, as shown in Figure 2d. The common synthesis method for GO is the Hummers method.[55] Graphite powder undergoes oxidation reaction in potassium permanganate mixed with concentrated sulfuric acid, resulting in the formation of brown GO flakes. These flakes are then dispersed in a solvent to create GO ink, which can be spin-coated onto a substrate. After spin-coating, the flakes from ink will stack with each other and form into a film during the solvent evaporation. As for intercalation, electrochemical method is commonly utilized, and recently, Lin et al. intercalated into $MoS_2$ crystal (cathode) with tetraheptylammonium bromide molecules in acetonitrile solvent, so as to exfoliate them into thin layers. Then they spin-coated the $MoS_2$ slurry on a substrate and produced a stretchable large area semiconductor film (Figure 2d) with good mechanical and electrical properties.[61]

### 2.2. Transfer Methods for Suspension

Advanced 2D materials need to be peeled off from their grown substrate to be made into suspended vibrating diaphragms for possible acoustic devices. Here in this section, we mainly discuss the transfer method including polymer assisted wet transfer method and the dry transfer method using polydimethylsiloxane (PDMS) stamps, and also review the latest developments of suspension process for large area 2D materials. It is worth noting that transferred materials are susceptible to wrinkling and internal stress introduced by some unavoidable sharp corners or undulations, which will be discussed in Section 2.4.

The dry transfer method does not need to dissolve the substrate. This method is suitable for 2D materials with weak adhesion to the substrate (such as vdW adhesion) .[62–64] 2D materials can be peeled off directly on the PDMS and transferred to the target substrate (including the substrate with holes) through a point-to-point method with a certain area typically of


© 2023 Wiley-VCH GmbH

16163028, 0, Downloaded from https://onlinelibrary.wiley.com/doi/10.1002/adfm.202303519 by Peking University Health, Wiley Online Library on [07/10/2023]. See the Terms and Conditions (https://onlinelibrary.wiley.com/terms-and-conditions) on Wiley Online Library for rules of use; OA articles are governed by the applicable Creative Commons License

16163028, 0, Downloaded from https://onlinelibrary.wiley.com/doi/10.1002/adfm.202303519 by Peking University Health, Wiley Online Library on [07/10/2023]. See the Terms and Conditions (https://onlinelibrary.wiley.com/terms-and-conditions) on Wiley Online Library for rules of use; OA articles are governed by the applicable Creative Commons License

several tens of micrometers (shown in **Figure 3**a). Only polymer stamps (such as PDMS) with the relatively clean surface are utilized in this process so that there is less pollution introduced. This method is most efficient in fabricating small acoustic devices with suspended diaphragms. Another capillary-force-assisted transfer method is also developed and 2D materials such as TMDs can be transferred through water invasion, implying that the capillary adhesion between PDMS and 2D materials hydrophobic surfaces is strong enough to overcome the vdW force between TMDs and substrate.[65–67] By using dry method, the materials can be easily separated from the substrate without any etching process. However, dry method inevitably leads to uneven strain distribution during material contact, making it challenging to transfer large area films. What's more, for some materials grown by CVD, it is also difficult to achieve peeling on polymers because of the relative strong adhesion with the substrate, so the usage of this method is sometimes limited.

Wet transfer is suitable for 2D materials with stronger adhesion with the substrate, and it's necessary to etch the substrate in order to release the membrane. It enables transfer of larger area membrane.[66,68–71] For 2D materials such as graphene grown on Cu substrate, their interaction is strong and it is not accessible to directly exfoliate them from the substrate. So the wet transfer method with polymethyl methacrylate (PMMA) as a temporary supporting substrate was utilized (Figure 3c). After etching the Cu substrate, the graphene supported by PMMA layer could be then attached to the target substrate, such as substrates with holes. PMMA can then be removed by acetone. However, especially for the suspended structure, the introduction of acetone causes unavoidable cracks on the film due to the change in surface tension caused by the evaporation of acetone. This problem can be further handled by utilizing critical point dryer (CPD). Before the drying procedure, acetone is replaced by alcohol and then alcohol is replaced by liquid $CO_2$. Here supercritical drying is performed to make the $CO_2$ reach its critical point during the drying process through the control of pressure and temperature, and complete its transition from liquid phase to a supercritical fluid. In the supercritical state, there is no interface between gas and liquid, so the supercritical fluid would be gradually expelled from the chamber. With the assistance of CPD, structural damages of 2D membranes caused by capillary force and stretch of the film could be avoided a lot, which contributes to large area membrane suspension.

Recently, researchers have developed novel approaches for transferring large-sized 2D materials and improving the diameter to thickness ratio of suspended 2D materials gradually. Wang et al. developed an inverted floating method (IFM) that improved upon the previous PMMA-assisted transfer and successfully achieved the suspended transfer of monolayer graphene with a diameter of 200 μm.[72] Akbari et al. used a similar IFM for transferring thin films and further controlled the internal stress through vacuum thermal annealing, successfully producing large-area suspended ultraclean monolayer and bilayer graphene membranes with diameters of up to 600 μm and 750 μm.[73] The transfer of even larger-area suspended thin films primarily relies on the newly developed sublimation-assisted transfer method. Carvalh et al. coated CVD-produced graphene with anthracene in a vacuum evaporator (pressure at $5 \times 10^{-2}$ millibars, temperature at 130 °C, heating for 30 minutes). They separated the graphene/anthracene film from the copper substrate by electrochemical bubbling in a 0.4 M NaCl solution (at a voltage of 4 V), then removed the NaCl impurities from the film and sublimated the anthracene film on the graphene film at 115 °C (at $5 \times 10^{-2}$ millibars). The success rate of the transfer using this sublimation-assisted transfer process is close to 100%, achieving suspended graphene with a thickness of 10 layers and a diameter of 4 mm, which is at least two orders of magnitude larger than previous literature.[74] What is even more astonishing is that Nam et al. utilized camphor as a support layer and gradually sublimated it using ethanol vapor at 75 °C, achieving a ultralarge suspension of graphene with amazingly thickness of ≈20 nm and diameter of $100 \times 100$ mm$^2$ after 48 h.[75] These suspended graphene membranes with ultrahigh diameter to thickness ratios are crucial for the fabrication of high-performance acoustic devices.

### 2.3. Micromachining Fabrication Process

In this era of information and intelligence, functional devices such as acoustic chips, acoustic photoelectric sensors, micro/nanoelectromechanical systems (MEMS/NEMS) and micro/nanoresonators based on suspended materials are developed towards high-performance and miniaturization with low power consumption and multi-functions. Different fabrication strategies have been developed and here we only briefly discuss the "bottom-up" strategy and the "sacrificial layer" strategy in the followings.

Bottom-up strategy aims at fabricating the device from the bottom layer to the upper layer and forming a cavity[76,77] (Figure 3h). The craft begins from a bare silicon wafer and a layer of silicon dioxide is grown on it by plasma enhanced chemical vapor deposition as an insulator. The pattern on the mask is transferred to the photoresist by ultraviolet lithography. The patterned photoresist performs as a temporary mask for subsequent physical etching. Then holes are etched with reactive ion etching until the insulator is penetrated. After that, the bottom electrode is constructed with the electron beam deposition followed by solving the photoresist with acetone. After transferring the membrane, the microscale gold electrode should be deposited or transferred onto the edge of the material to form the top electrode. Through this method a simple MEMS/NEMS acoustic device is built up which is able to be driven by alternating current.

Sacrificial layer strategy is more complex (Figure 3i).[78] In this route, the risk of diaphragm collapse during transfer could be minimized by setting the wet etching as the final step. Before the wet etching step, 2D material is supported by solid substrate. The sacrificial layer strategy relies on a silicon on insulator (SOI) wafer in which two doped silicon layers and one silicon dioxide sacrificial layer consists of a sandwich combination. After depositing the $Si_3N_4$ on both sides, photolithography operations are conducted to form the cavity and back hole. Here the $Si_3N_4$ works as a stop layer in chemical mechanical polishing and $Si_3N_4$ on the other side is for protection in the following anisotropic etching on the thick silicon. The thick crystal silicon wafer crystal has different directions and the etching rate at <111> is faster than in other directions. Since the normal direction of the SOI is <100>, the wafer is etched by KOH to the residual of frustums which

 © 2023 Wiley-VCH GmbH

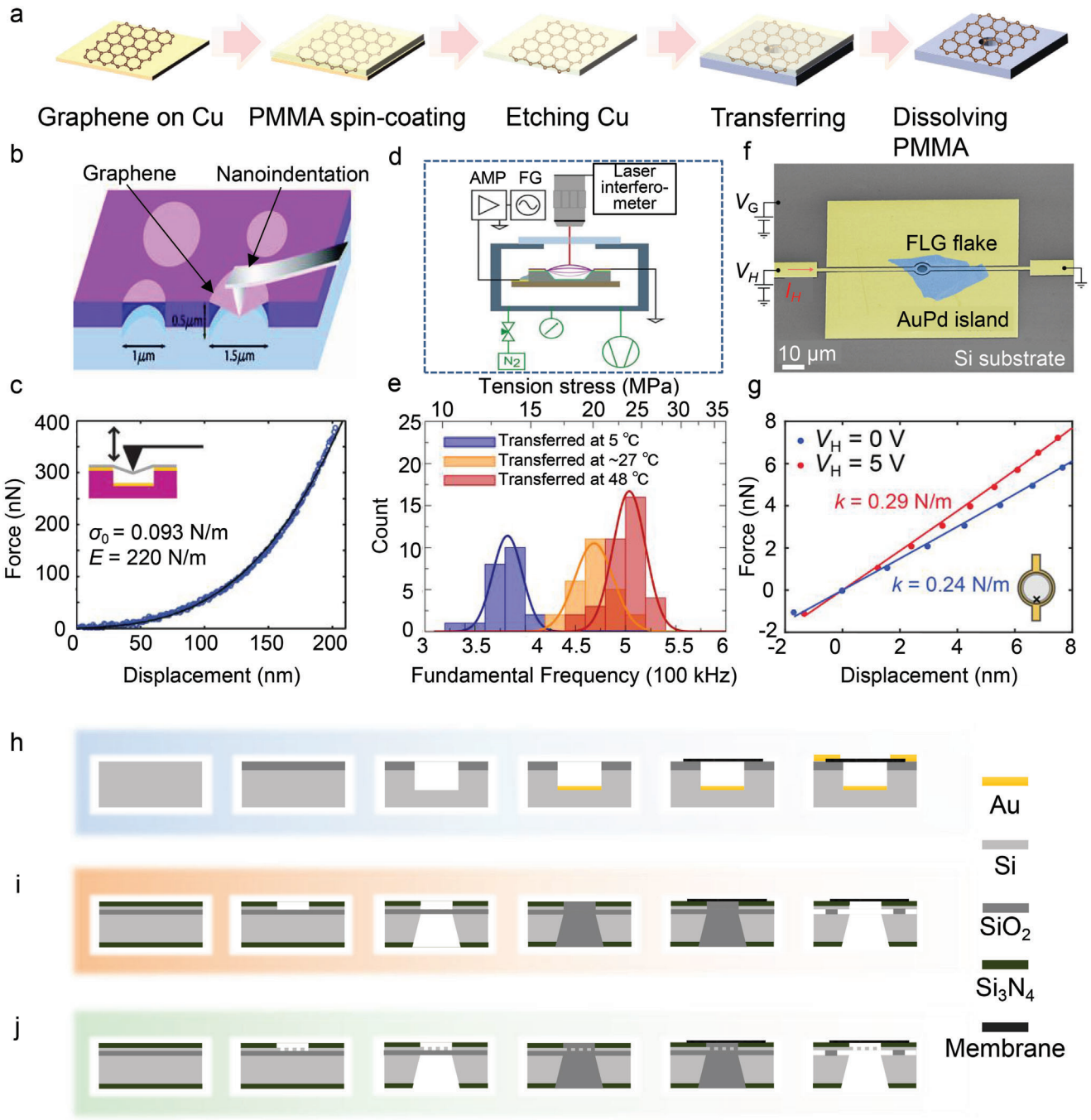


**Figure 3.** Demonstration of material transfer process, prestress characterizing and tuning method of suspended 2D materials, and fabrication of the MEMS/NEMS structure. a) Polymer assisted wet transfer process. b) Schematic of nanoindentation on suspended graphene membrane. Before indentation, the graphene film undergoes non-contact AFM scanning, and mechanical testing is conducted at a constant displacement rate, followed by load reversal. This process is typically repeated multiple times to verify that the deformation of the graphene film remains within the elastic range and that no slippage occurs. Reproduced with permission.[85] Copyright 2008, The American Association for the Advancement of Science. c) Force–distance curve acquired by applying point load with the AFM tip at the center of 2.3 μm radius device. The black line is a fit of a theoretical equation for a prestressed membrane under a point load. Reproduced with permission.[86] Copyright 2018, American Physical Society. d) Experimental setup for prestress measurement of the electrostatic resonator. A sinusoidal voltage waveform sourced from a function generator (AG) is amplified by a high-voltage amplifier (AMP) to drive the device placed in a custom vacuum cell. Time–domain deflection profiles are recorded via a laser interferometer, then frequency-domain signal acquired through fast Fourier transformation to identify the fundamental resonance frequency and prestress can be determined according to theoretical equation. Reproduced with permission.[89] Copyright 2021, American Chemical Society. e) Histograms of fundamental mode frequencies $f_{1,1}$ and corresponding prestress of membrane resonators stamped onto the target substrate at different temperatures. Due to the pronounced thermal expansion of the PDMS stamp, the membranes' prestress shifted to higher values with increasing temperature. Reproduced with permission.[89] Copyright 2021, American Chemical Society. f) False-colored scanning electron micrograph of an on-chip heater device, which is composed of a ring-shaped AuPd heater


© 2023 Wiley-VCH GmbH

16163028, 0, Downloaded from https://onlinelibrary.wiley.com/doi/10.1002/adfm.202303519 by Peking University Health, Wiley Online Library on [07/10/2023]. See the Terms and Conditions (https://onlinelibrary.wiley.com/terms-and-conditions) on Wiley Online Library for rules of use; OA articles are governed by the applicable Creative Commons License

share the same bottom angle of 54.7°. Then the cavities would be filled with silicon dioxide via low pressure chemical vapor deposition. After chemical mechanical polishing to the stop layer at both sides, the membrane could be transferred to the surface. In the end, the sample should be soaked in buffered oxide etch (BOE) to etch away the sacrificial silicon dioxide. Since transfer is operated on a flat surface, it is much more possible to avoid the inner stress and realize suspension of larger scale.

The above sacrificial layer method can be used in possible acoustic device fabrication process using suspended 2D materials as vibrating membranes. For example, considering the demand for capacitive acoustic devices, we propose a possible scheme based on the sacrificial layer method (Figure 3j). The main process is similar to the general sacrificial layer method, but the highly doped conductive silicon layer in the middle of the SOI substrate is retained and the vent holes are micromachined on it. With this strategy, the suspended 2D material can be combined with the existing MEMS/NEMS structure, which has great potential for future miniaturized acoustic devices.

### 2.4. Prestress Regulation Techniques for Suspended 2D Membranes

It is widely known that inappropriate internal stress or prestress can result in the cracking or wrinkling of the 2D materials, which in turn has an adverse impact on the overall integrity of the materials.[79,80] Moreover, the prestress plays a pivotal role in determining dynamic response performance of 2D material membranes, drums or ribbons, particularly with respect to the vibration fundamental frequency and sensitivity of the suspended ones.[29] One of the key principles in tuning tunable 2D material resonators is to regulate the fundamental frequency of the diaphragm by controlling its prestress.[81,82] Besides, as the prestress of 2D material diaphragm arises, dislocations begin to emerge in the diaphragm sample and gradually become the predominant means of energy dissipation,[83] which possibly increase the noise performance of resonators. Additionally, excessive prestress may restrict the sensitivity of acoustic devices.[29] Thus, characterizing the prestress and attempting to tune it is an important strategy for exploiting the performance of 2D materials based acoustic devices.

Prestress characterization can be categorized into contact and noncontact methods. Among the established contact measurement instruments are atomic force microscopy (AFM) and nanoindentation,[84] which employ a probe that comes into contact with the surface of 2D materials to obtain the force–displacement or stress–strain curves. The curves are then fitted to the theoretical deformation equation to obtain the prestress, in accordance with statistical laws.[85] These methods can also be applied to measure other mechanical properties of 2D materials, including Young's modulus, fracture strength, hardness, and fatigue curves.[86,87] However, these methods suffer from certain disadvantages, such as a narrow scanning range, significant influence from the probe material, an inability to confirm the contact point between the probe and the material accurately, and a lack of efficiency in mechanically characterizing large suspended films. Moreover, potential pitfalls exist, such as the possibility of the probe damaging the materials during testing.

Noncontact prestress characterization methods are primarily based on electrostatic or optical techniques. Typically, an electrode plate is added to one end of suspended 2D material membrane, followed by an actuation voltage.[88,89] The membrane is deformed due to electrostatic force, and the deformation is then measured using a laser displacement meter or an optical profilometer.[90] The prestress is subsequently fitted according to the deformation equation, with note taken that the deformation equation used here should be employed for surface force rather than the point force equation used in AFM.[91] However, there is a risk that the voltage may be too high and exceed the deformation limit of the membrane, causing it to break. Nonetheless, the electrostatic excitation method is a simple and straightforward way of characterizing prestress in large-area suspended membranes. It is worth noting that stress also has a significant impact on the Raman spectroscopy of 2D materials.[92,93] Del Corro's study revealed that the direction of the shift is related to the type of stress, and that the Raman characteristic peaks are blue-shifted when graphene is subjected to compressive stress due to the reduction of carbon atom spacing, while they are red-shifted when subjected to tensile stress.[94] Nonetheless, implementing the Raman spectroscopy method for fast and real-time characterization of the prestress of 2D materials can be challenging.

Studies on techniques for tuning the prestress of 2D materials have concentrated on the transfer and utilization processes. Due to the significant thermal expansion of the PDMS stamp, nearly $3 \times 10^{-4}$ $K^{-1}$ ,[95] the prestress of films adhering to the stamp's surface is affected during heating or cooling. Based on this property, Hartmann et al. were able to adjust the average prestress of suspended films composed of graphene oxide/silk fibroin from approximately 14 MPa to around 28 MPa by increasing the temperature during the final transfer step from 5 °C to 48 °C.[89] Kim et al. have discovered, through in situ optical microscopy, that when trapped water evaporates through the pinned solid-liquid-gas, the film is drawn towards the center of the water droplet, resulting in the generation of biaxial compressive strain in the film layer.[96] Therefore it is an intriguing notion to utilize solvents with varying surface tensions to modify the prestress in the film after suspension during wet transfer. Once the device has been fabricated, electrostatic regulation via an actuation voltage presents a feasible option for controlling the prestress of 2D materials,[97] similar to the technique described in prestress characterization. However, it is worth noting that due to the Joule dissipation of electrons in the displacement current through the resonator, the

structure with suspended few-layer graphene flake and the surrounding AuPd islands. The heater voltage ($V_H$) is applied to one end of the chip while the other end is grounded. As a result, a temperature increase is induced in the chip due to the dissipated power ($V_H I_H$). Reproduced with permission.[99] Copyright 2018, American Chemical Society. g) Two AFM force-deflection curves taken near the edge of the drum (black cross in the inset) at two heater voltages: 0 V (blue) and 5 V (red). The slope of each curve characterizes the spring constant of the drum, which is intimately linked to its prestress. By increasing the applied heater voltage, the prestress of the graphene drum will increase and thus be precisely tuned. Reproduced with permission.[99] Copyright 2018, American Chemical Society. h) Bottom-up fabrication strategy of suspended 2D materials based acoustic device. i) Sacrificial layer fabrication strategy of suspended 2D materials. j) Sacrificial layer fabrication strategy of suspended 2D materials based capacitive microphone.


© 2023 Wiley-VCH GmbH

16163028, 0, Downloaded from https://onlinelibrary.wiley.com/doi/10.1002/adfm.202303519 by Peking University Health, Wiley Online Library on [07/10/2023]. See the Terms and Conditions (https://onlinelibrary.wiley.com/terms-and-conditions) on Wiley Online Library for rules of use; OA articles are governed by the applicable Creative Commons License

16163028, 0, Downloaded from https://onlinelibrary.wiley.com/doi/10.1002/adfm.202303519 by Peking University Health, Wiley Online Library on [07/10/2023]. See the Terms and Conditions (https://onlinelibrary.wiley.com/terms-and-conditions) on Wiley Online Library for rules of use; OA articles are governed by the applicable Creative Commons License

electrostatically induced approach is often accompanied by a decrease in the quality factor.[98] To address this, Davidovikj et al. proposed a thermally induced prestress control method that increases the planar tension of graphene nanodrums by Joule heating of the metal suspension ring.[99] This method resulted in a 10% increase in the resonant frequency along with a 32% increase in the quality factor. Moreover, Yang et al proposed an integration system between the graphene ribbon with silicon micro actuators, allowing precise control of in-plane prestress of the suspended ribbon.[83] Nevertheless, the aforementioned prestress tuning techniques have seldom been implemented on large scale 2D materials, thus warranting further investigation in this area.

In summary, great progress has been made in the synthesis of large area 2D material-based membranes, accompanied with a variety of methods that utilize advanced instruments and fabrication protocols to minimize wrinkles and damage to the membranes during the transfer process. Furthermore, the importance of prestress in suspended 2D material-based membranes has gained increasing attention with potential approaches for regulating prestress during suspension. However, current transfer techniques still face bottlenecks and a reliable method with high throughput is still waiting for exploration, such as achieving precise control over prestress and complete avoidance of wrinkles. The fabrication of suspended few-layer or even single-layer 2D material with millimeter or centimeter scale still remains a significant challenge. However, with continuous advancements in synthesis, transfer, and prestress control technologies, it is expected that larger diameter to thickness ratios can be achieved in suspended 2D material-based membranes, which will greatly facilitate the development of higher-performance next-generation acoustic devices.

## 3. Acoustic Transducers in Audio Frequency

The sensitivity of the human ear to sound varies with sound frequencies. The human can hear sounds within the range of 20 Hz to 20 kHz, which is called the audio frequency range. Sounds below 20 Hz are called infrasonic sounds and sounds above 20 kHz are called ultrasonic sounds.[10] An audio frequency acoustic device produces or processes sound waves within the audio range, which can be generally divided into two types: speakers and microphones, used for sound generation and detection, respectively. Traditional electronic industries have developed mature production procedures for these transducers. However, with the continuous development of wearable, portable, and integrated electronic devices, the demand for smaller, more energy-efficient, and more stable transducers is increasing.[100,101] This demand for miniaturization, energy efficiency, and stability has become a bottleneck for traditional electronics industries. The development of 2D materials holds great promise in addressing these challenges. With their large mechanical modulus, flexibility, and extremely thin layers, 2D materials can be prepared into higher quality acoustic devices.[102,103] In the following sections, we will discuss recent developments in 2D material-based audio frequency acoustic transducers in detail.

### 3.1. Speakers: The Main Type of Sound Generator

There are four main types of speakers: electrostatic, electrodynamic, piezoelectric, and thermoacoustic. Electrostatic speakers use a thin, electrically charged diaphragm sandwiched between two metal grids to produce sound waves[11] (**Figure 4**a). An electrodynamic speaker emits sound by vibrating due to the generated AC Ampere force when its current changes periodically in a magnetic field (Figure 4b).[104] A piezoelectric speaker vibrates directly due to the strain caused by AC current, which is called the inverse piezoelectric effect[105] (Figure 4c). These three types of speakers all require a diaphragm structure to produce sound, which can be made from 2D materials (Figure 4d). Thermoacoustic speakers, on the other hand, require a stationary heating film instead of a vibrating diaphragm, and will be discussed in Section 3.1.3. (Figure 7a).

The sound generation process can be simplified as follows: for the sake of simplicity, let us assume that the vibrating diaphragm is circular and produces periodic pressure fluctuations (as shown in Figure 4d). Based on the Helmholtz equation and Rayleigh integral,[106] SPL generated at the distance $z$ from the center of the diaphragm can be expressed as follows,

$$P\ (z) = \rho\left(2\pi f\right)^2 \int_0^a \frac{w\,(r)}{\sqrt{z^2 + r^2}} \tag{1}$$

where $\rho$ represents the mass density of the fluid medium outside the membrane, $f$ denotes the vibration frequency of the diaphragm, $a$ is the radius of the diaphragm, $r$ is the distance from the center of the diaphragm to the vibration point, $w(r)$ represents the vibration amplitude at the point, and $z$ denotes the vertical distance from the sound receiver to the center of the diaphragm. The sound pressure detected by the receiver is represented by $P(z)$. If we simplify the system as a vibrating piston, the effective sound pressure $P_{\text{eff}}(z)$ measured by receiver can be given by,

$$P_{\text{eff}}\ (z) = \frac{\sqrt{2}\pi\rho A w f^2}{z} \tag{2}$$

where $A$ is the effective area of the diaphragm. By convention, we define the reference sound pressure as 20 μPa, denoted as $P_{\text{ref}}$. Then, we can define the SPL as the logarithm of the ratio between the actual pressure and reference pressure, measured in decibels (dB), expressed as follows,[107]

$$\text{SPL (dB)} = 20 \log\left(\frac{P_{\text{eff}}\,(z)}{P_{\text{ref}}}\right) \tag{3}$$

We aim for an optimal speaker performance, which is partly defined by a higher sound pressure level produced at a certain position. According to Equation (2), we can conclude that, for a given material with mass density $\rho$, a larger radiation area $S$ and vibration amplitude $w$ lead to higher output SPL. This is particularly important given the relatively lower sound frequency $f$ in the audio range.

Another important feature of speaker is bandwidth. A flatter and broader output bandwidth across the frequency range indicates a wider vocal range,[108,109] potentially indicating two another demands for the speaker's diaphragms: high tunability[110]


© 2023 Wiley-VCH GmbH

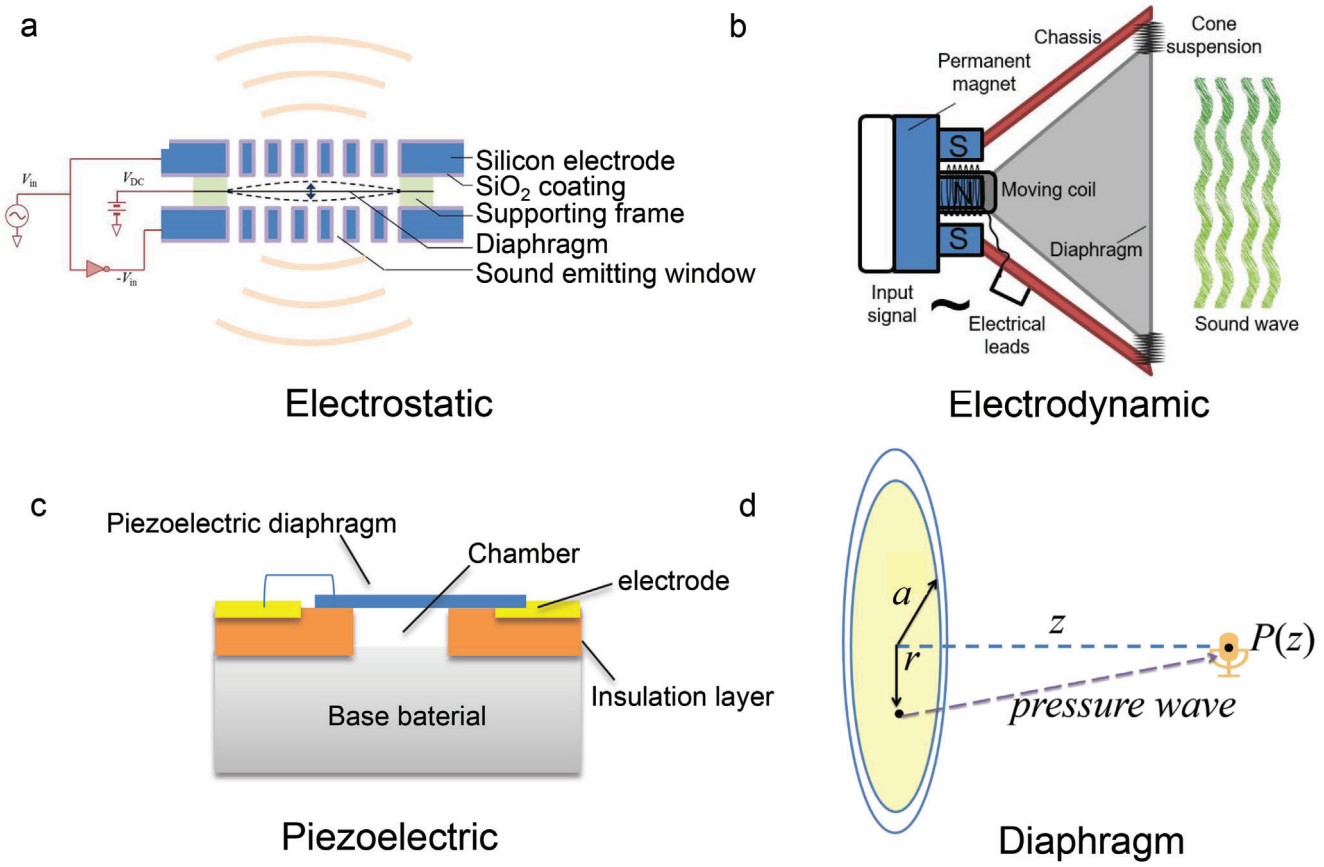


**Figure 4.** Basic structures of various kinds of speakers. a) Electrostatic speaker, where the diaphragm vibrates through AC change of electrostatic force. $V_{in}$ and $V_{DC}$ are input and gate voltage. Reproduced with permission.[111] Copyright 2013, AIP Publishing. b) Electrodynamic speaker, where the diaphragm is driven by AC ampere force in magnetic field to produce sound. c) Piezoelectric speaker, with the diaphragm made of piezoelectric materials actuated by AC changes of current through inverse piezoelectric effect. d) Simplified speaker circular diaphragm structure, with the radiated sound pressure $P(z)$ at vertical distance z from the center of the diaphragm.

and suitable damping coefficient.[111] These help to tune the fundamental vibrating frequency of the diaphragm far beyond the working range and reduce its vibration peaks.[112] To qualitatively illustrate the role of damping, considering the equivalent model of a lumped parameter system, damping is approximated as a resistance acting on the particle in proportion to velocity. The general formula for forced damping vibration is given as follows,

$$mw'' + bw' + kw = F(\tau) \tag{4}$$

where $m$ is the equivalent mass of the vibration system, $w$ is the displacement of the vibration system, $k$ is spring constant of diaphragm material, $\tau$ is the time, $b$ is defined as the damping coefficient, and $F(\tau)$ is the function of external force such as periodic electrostatic force. There is a certain relationship between damping coefficient $b$ and damping ratio $\zeta$,

$$\zeta = \frac{b}{2\sqrt{mk}} \tag{5}$$

Damping ratio $\zeta$ is closely related to quality factor $Q$, which is given by the following equation,

$$Q = \frac{\omega_0}{\Delta\omega} \tag{6}$$

where $\omega_0$ is the natural angular frequency of the vibration system, $\Delta\omega$ is the bandwidth (also named as half power bandwidth) of the vibration system. The quality factor $Q$ is represented by the damping ratio $\zeta$ with the following relationship,

$$Q = \frac{1}{2\zeta} \tag{7}$$

From Equation (5) we know the smaller mass and spring constant (also named rigidity) leads to larger damping ratio at the same condition. From Equation (7) it is clear that when the damping is small or close to zero, the quality factor $Q$ of the vibration system is large, indicating a high vibration peak shown on the spectrum. On the contrary, when the damping is large, the quality factor $Q$ of the vibration system is small, so a more flat and broad frequency response on the output spectrum will be given, which is crucial for high-quality audio devices. In comparison to traditional bulk materials, 2D materials possess ultralight mass


© 2023 Wiley-VCH GmbH

16163028, 0, Downloaded from https://onlinelibrary.wiley.com/doi/10.1002/adfm.202303519 by Peking University Health, Wiley Online Library on [07/10/2023]. See the Terms and Conditions (https://onlinelibrary.wiley.com/terms-and-conditions) on Wiley Online Library for rules of use; OA articles are governed by the applicable Creative Commons License

16163028, 0, Downloaded from https://onlinelibrary.wiley.com/doi/10.1002/adfm.202303519 by Peking University Health, Wiley Online Library on [07/10/2023]. See the Terms and Conditions (https://onlinelibrary.wiley.com/terms-and-conditions) on Wiley Online Library for rules of use; OA articles are governed by the applicable Creative Commons License

and low rigidity, so they are definitely promising candidates for these demands.

#### 3.1.1. Electrostatic Speakers Based on 2D Materials and Their Composites

Electrostatic driving is a commonly used method for speakers that typically consists of an air chamber, a coil actuator, and a diaphragm[11] (Figure 4a). The diaphragm, made of 2D material, is suspended between excitation electrodes and initially biased with a direct current (DC) voltage, $V_{DC}$. When there is no input signal, the forces exerted by the upper and lower electrodes on the diaphragm are balanced. When an excitation voltage, $V_{in}$, is applied, the resulting force per unit area on the diaphragm, $F$, is the difference between the opposing forces of the two electrodes, $F_1$ and $F_2$. This can be expressed as,

$$F = F_1 - F_2 = \frac{\epsilon V_{DC} V_{in}}{d^2} \tag{8}$$

where $\epsilon$ denotes the permittivity of air and $d$ represents the plate spacing. This resulting force is proportional to the input voltage, $V_{in}$, and exhibits a linear response in the speaker, resulting in lower acoustic disturbance. The spring constant $k$ and effective spring constant $k_{eff}$ are given by,

$$k_{eff} = 4\pi\sigma_0 t \tag{9}$$

$$k = \frac{k_{eff}}{\text{Diaphragm area}} = \frac{4\sigma_0 t}{a^2} \tag{10}$$

where $\sigma_0$ is the initial internal stress of the diaphragm and $t$ is the thickness of diaphragm. Due to the potential of being fabricated with high diameter to thickness ratio, 2D material-based diaphragms always possess lower spring constant than normal bulk materials,[14] which triggers larger deformation of 2D material-based diaphragms. This larger deformation of the diaphragm contributes to the SPL of speaker. Combined with the good tunability and damping properties[13] of 2D materials, a broader and flatter bandwidth of speaker can be also achieved.[8] The three main types of 2D materials used for preparing electrostatic speakers diaphragm are introduced as follows.

*Graphene Diaphragm Electrostatic Speakers*: Graphene is one of the earliest developed 2D suspended diaphragm materials that illustrates the possibility of producing speakers with higher SPL output, flatter bandwidth, and better energy efficiency with 2D suspended materials. Zhou et al. were among the first to complete the preparation of a graphene suspended speaker.[11] They used methane gas flow to grow graphene films on a nickel substrate in a CVD tubular furnace at 1000 °C, then etched the substrate with $FeCl_3$ to stand the diaphragm (as shown in Figure 4a) with a diameter of about 7 mm and a thickness of around 60 µm (the photo of the speaker diaphragm is shown in **Figure 5**a). A standard acoustic test was conducted on this speaker within the frequency range of 20 to 20000 Hz (the results are shown in Figure 5b). Compared with the commercial Sennheiser MX-400 speaker, the graphene speaker has optimal SPL output and avoiding sharp resonances in the range of 5–20 kHz.

Air damping of the electrostatic speaker is also enhanced by utilizing graphene diaphragm, potentially contributing to the more broad and flat acoustic output. Depositing an insulating $SiO_2$ layer on the electrode can further prevent the diaphragm from short circuit failure. Based on the above research, Infineon Technologies AG provided detailed technologies to prepare graphene electrostatic speakers in 2016,[113] and the patent of Zhou and Zettl in 2020 further improved the original fabrication methods.[114]

*Graphene Oxide (GO)-Based Electrostatic Speakers*: GO materials, due to their oxygen-group functionalization, have cross-linked chemical bonds within the originally packed graphene sheets, which make them more conducive to being prepared into large-area and low-thickness diaphragms. This is because of their improvement in mechanical properties, as compared to graphene, which relies on vdW interactions.[56,115] Moreover, GO diaphragms can be formed through a self-assembly process, which is more cost-effective and safer than the expensive CVD method used for graphene production. Various solvents such as water, isopropanol, and DMF can be used for preparing GO diaphragms in solvent casting, wet spinning, electrochemistry, and other methods.[116] In some of these methods, the concentration of GO in the solvent can be precisely controlled to determine the diaphragm thickness for quantitative control of their fabrication.[117,118]

Moreover, speaker diaphragms based on GO can demonstrate excellent mechanical stability and suitable damping characteristics. In some cases, the synthesized GO diaphragms have Young's modulus exceeding 30 GPa, which can be further enhanced by cross-linking with borate ion, polyethylene imine, or other chemical groups to form cross-linked GO (X-GO) films, achieving a Young's modulus higher than 80 GPa.[112,119] Additionally, the unique viscoelastic properties of GO and X-GO result in a higher damping ratio compared to other traditional speaker diaphragms such as metal diaphragms. It is indicated that the damping ratio of microspeakers with GO and X-GO diaphragms is respectively 39% and 46% higher than those with aluminum diaphragms. Insufficient damping typically leads to unpleasant ringing when the excitation spectrum signal overlaps with the resonant frequency of the speaker diaphragm. Therefore, GO and X-GO diaphragms further optimize the acoustic performance of the speakers with their larger damping ratio.

All of these desirable properties make GO a promising material for utilization in higher quality acoustic devices. In 2016, Gaskell et al. proposed a method for using GO film to prepare speaker diaphragms for the first time.[120] This resulted in an output SPL with a flat acoustic response from 20 Hz to nearly 40 kHz and a figure of merit as high as 6.5–9.5 $m^4/(kg\ s)$, comparable to Beryllium (it's known that Beryllium diaphragm possesses almost the highest figure of merit among common diaphragm materials). In 2022, Hu et al. also suggested a representative electrostatic speaker based on the diaphragm made of borate cross-linked oxide graphene and GO.[112] The X-GO films can be synthesized using a flow directed vacuum filtration method or vacuum assisted self-assembly (VASA) method to achieve the thickness of approximately 100 µm (Figure 5c). The damping ratio of X-GO film was tested and compared with common diaphragm materials such as Ti, Al, and polyethylene terephthalate (PET), revealing a significantly higher value. It's shown that their material

 © 2023 Wiley-VCH GmbH

16163028, 0, Downloaded from https://onlinelibrary.wiley.com/doi/10.1002/adfm.202303519 by Peking University Health, Wiley Online Library on [07/10/2023]. See the Terms and Conditions (https://onlinelibrary.wiley.com/terms-and-conditions) on Wiley Online Library for rules of use; OA articles are governed by the applicable Creative Commons License

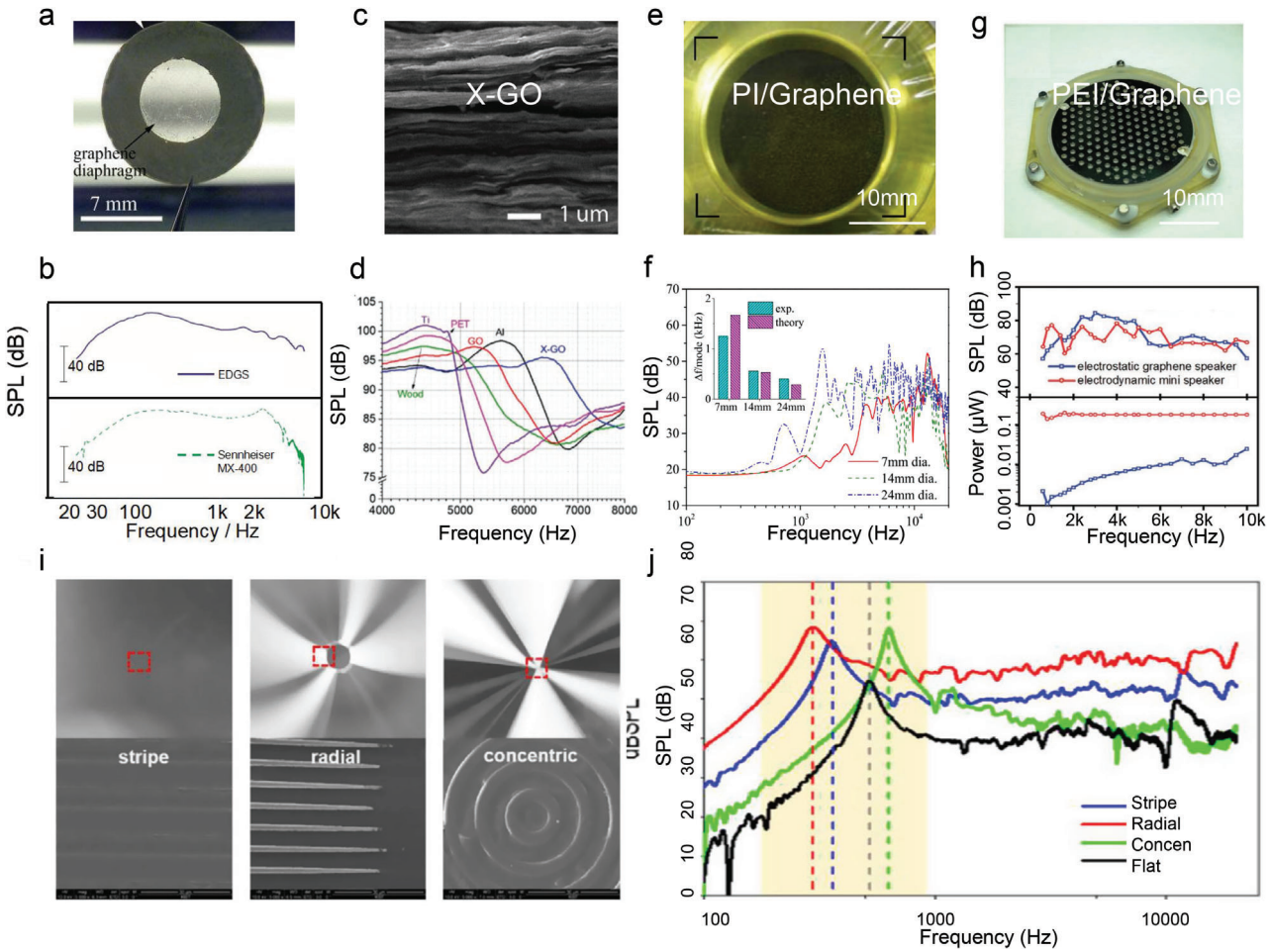


**Figure 5.** Physical diagram of electrostatic speakers and its performance test results. a) Structure of the graphene electrostatic speaker. Reproduced with permission.[11] Copyright 2013, AIP Publishing. b) SPL output of the graphene speaker (EDGS) compared with the commercial Sennheiser MX-400 speaker. The bandwidth and output SPL is higher than commercial Sennheiser MX-400 speaker. Reproduced with permission.[11] Copyright 2013, AIP Publishing. c) Structure and d) output SPL of speakers with diaphragms made by GO, X-GO and other materials. GO and X-GO shows wider bandwidth with weaker resonance peak in audio frequency, exhibiting flatter bandwidth output. Reproduced with permission.[112] Copyright 2021, Wiley-VCH. e) Structure and f) SPL output of graphene/PI diaphragm. As the diameter of diaphragm enlarges, the bandwidth becomes broader, however the wiggles in higher frequency increased which is harmful to generate high quality sound. Reproduced with permission.[129] Copyright 2018, IOP Publishing, Ltd. g) Structure and h) SPL output of graphene/PEI diaphragm. The composited diaphragm microphone possesses higher SPL than commercialized mini speakers on average, with much smaller energy consumption. Reproduced with permission.[130] Copyright 2020, Wiley-VCH. i) Speaker diaphragms with three types of micro-decoration patterns and j) corresponding SPL output. Increase in SPL and change of resonant peak can be controlled by selection of micro-decoration patterns. Reproduced with permission.[131] Copyright 2023, American Chemical Society.

performance index (MPI, which is proportional to the loss coefficient and positively correlated with the elastic modulus, reflecting the acoustic properties of the material) was between 0.11–0.19 $m^4\ kg^{-1}\ s^{-2}$, considerably higher than that of the traditional diaphragms (with MPI around 0.01–0.05 $m^4\ kg^{-1}\ s^{-2}$), which is believed to be caused by the interlayer friction and cross-linking strengthening within X-GO structure. These demonstrates their excellent suitability for high-quality speaker diaphragms. The standard SPL test proves the broad bandwidth output of X-GO diaphragm (Figure 5d). Other relevant works from McGill University and Ora Graphene Audio have also developed the cost-reduction and industrialization methods for the further applications of GO and X-GO speaker diaphragms.[120]

*Graphene–Polymer Composites (GPC) Electrostatic Speakers*: GPC materials are formed by compositing graphene with various types of polymers such as polystyrene, polymethylmethacrylate, polypropylene, and polyamide. The mechanical properties of GPC are significantly enhanced compared to both the precursor graphene and individual polymers.[121,122] They have been developed in frontier fields such as actuators,[123] biosensors,[124] and thermal radiators.[125]

A review article in 2012 found that by adding only 3% to 5% graphene, Young's modulus of the polymer can be increased by 3 to 5 times without altering the mass density and flexibility of the original polymer, highly enhancing their mechanical stability.[126] Given the challenges associated with preparing large-area suspended diaphragms consisting of a few layers or single-layer graphene, such as defects and grain boundaries that easily lead to breakage during transfer process,[127] GPC diaphragms may offer a more stable material to address these issues.[128]

 © 2023 Wiley-VCH GmbH

16163028, 0, Downloaded from https://onlinelibrary.wiley.com/doi/10.1002/adfm.202303519 by Peking University Health, Wiley Online Library on [07/10/2023]. See the Terms and Conditions (https://onlinelibrary.wiley.com/terms-and-conditions) on Wiley Online Library for rules of use; OA articles are governed by the applicable Creative Commons License

It has been shown that GPC improves the maximum vibration amplitude and stability of speaker diaphragms, enhancing their SPL output and flattening their bandwidth output. In 2016, a patent by He et al. (CN106060721A) developed the GPC diaphragm fabricated in dilution coating method and enhanced the SPL output of speaker by around 2 to 6 dB within the range of 20 Hz to 40000 Hz. The newly developed GPC diaphragms are more resistant to breakdown compared to original graphene diaphragms. In 2017, Apple's patent (US20170006382A1) also demonstrated the reinforcement effect of GPC on the diaphragm. The impact of some parameters such as radius on the acoustic performance of GPC diaphragms has been studied afterward. Lee et al. fabricated a speaker with a double-layer graphene and polyimide (PI) composite GPC diaphragm and illustrate the impact of radius on its acoustic performance.[129] Through PMMA mediated transfer methods, graphene grown on the Cu substrate is released onto PI substrate to form the diaphragm (shown in Figure 5e). Experiment results (Figure 5f) showed that a larger radius of diaphragm negatively impacts its acoustic output stability in higher frequencies while contribute to the SPL output in lower frequencies (as shown in the wiggling blue line in Figure 5f). Khan et al. further investigated the role of diameter to thickness ratio on the acoustic performance of the diaphragm.[130] They significantly reduced the diaphragm's thickness with utilization of polyetherimide (PEI) as a thin base material with the thickness of 350 nm and fabricated a GPC diaphragm with the diameter of 25 mm, achieving a large diameter to thickness ratio of around $10^5$ (as shown in Figure 5g). The Young's modulus of this GPC diaphragm reaches a high value of 3.33 GPa so that only 1 mg GPC is able to support more than 30000 mg load if distributed uniformly. This enhanced mechanical properties may be attributed to the increased adhesion energy by $\pi$–$\pi$ interaction between the aromatic rings of PEI and single layer graphene (SLG). Experiment results show that in the range of more than 2 kHz, the output SPL of this diaphragm is on average 7.7 dB higher than that of mobile phone speakers in the same range (as shown in Figure 5h). The power consumption of this GPC speaker is significantly lower than that of a conventional mobile phone speaker across all frequency ranges, particularly at 600 Hz, demonstrating a mere 1% energy consumption compared to electric speakers.

In the above experiments, the resonance frequencies of the diaphragms are often tuned into the higher frequency range (larger than $10^3$ Hz) in order to avoid overlapping with the acoustic working range at lower frequencies, thereby making the audio range acoustic signal output from the speaker more uniform and stable. However, in some cases, the resonance peak at low frequencies (1 to 500 Hz) can improve the acoustic output performance of the speakers in the low octave range, which is mainly determined by the ratio of the diaphragm's spring constant and damping coefficient. Lee et al. synthesized different GPC materials to investigate this phenomenon, aiming to explore approaches to improve the low-frequency performance of the speaker.[131] First, they calculated the resonant frequency of the diaphragm, which is mainly influenced by parameters such as polymer composition thickness, Young's modulus and surface stress of the diaphragm of GPC, etc. This can be approximately expressed as follows,

$$f_{\mathrm{mn}} = \frac{\beta_{\mathrm{mn}}^2}{2\pi a^2}\sqrt{\frac{Et^2}{12\rho_{\mathrm{m}}(1-\nu^2)}} \tag{11}$$

where $N$ is graphene's layer number, $\beta_{\mathrm{mn}}$ is the modified Bessel function, $\rho_{\mathrm{m}}$ is the diaphragm's mass density, $t$ is the diaphragm's thickness, $\nu$ is Poisson's ratio and $E$ is the diaphragm's Young's modulus.

Comparing GPC diaphragms with PI, PET, and polyethylene naphthalene (PEN) components, it is evident that the thinner GPC diaphragm is able to create higher resonant SPL output which is in proportion to its vibration amplitude. The 25 μm PI/Graphene film exhibits the highest fundamental frequency SPL among all the GPC diaphragms. Next, Lee et al. studied the influence of substrates' micro-decoration patterns on their low frequency resonance. They found that the integration of micro-patterns such as striped square, radial circle, and concentric pattern significantly increased the SPL of 25 μm diaphragms by around 15 dB compared to those without pattern modifications (as shown in Figure 5i,j). Radio pattern is more special to tune the resonance frequency from 523.36 Hz to 293 Hz with an upgraded SPL output. So another method to enhance the low frequency resonant performance of speakers is to employ special surface pattern designs on their diaphragms. Other studies have also shown the significance of surface micropatterns, as indicated by refs.[132–134] These works warrant further in-depth research particularly for suspended 2D material systems.

In summary, electrostatic speakers based on suspended 2D materials possess the advantages of large dynamic range (DR), high SPL, and good energy conversion efficiency due to their light mass density, large diameter to thickness ratio, and high flexibility. However, some intrinsic weaknesses of electrostatic speakers such as the high voltage used to generate vibration pose safety hazard for their utilization.[135] In situations where the use of high voltage needs to be avoided, it is necessary to consult other types of speakers.

#### *3.1.2. Other Types of Electric Sound Generators Based on 2D Materials and Their CompositesElectrodynamic Speakers*

The well-known moving-coil speakers (also named as electrodynamic speakers) are based on the electromagnetic induction principle where a coil is embedded to the speaker's diaphragm. A periodic Ampere force excites the periodic motion of the coil, leading to the vibration of the attached diaphragm,[5] as shown in Figure 4b. This is the most general type of speakers in traditional electronics, invented by General Electric Company of the United States in the middle of the 20th century. It possesses the advantages of high SPL, simple structure, and small distortion.[136] However, the coil structure is heavy and inevitably has many microscopic burrs, making it difficult to integrate with the newly developed ultrathin, super-light 2D diaphragms.

By redesigning the structure of the electrodynamic speaker, researchers have successfully embedded a coil structure within

 © 2023 Wiley-VCH GmbH

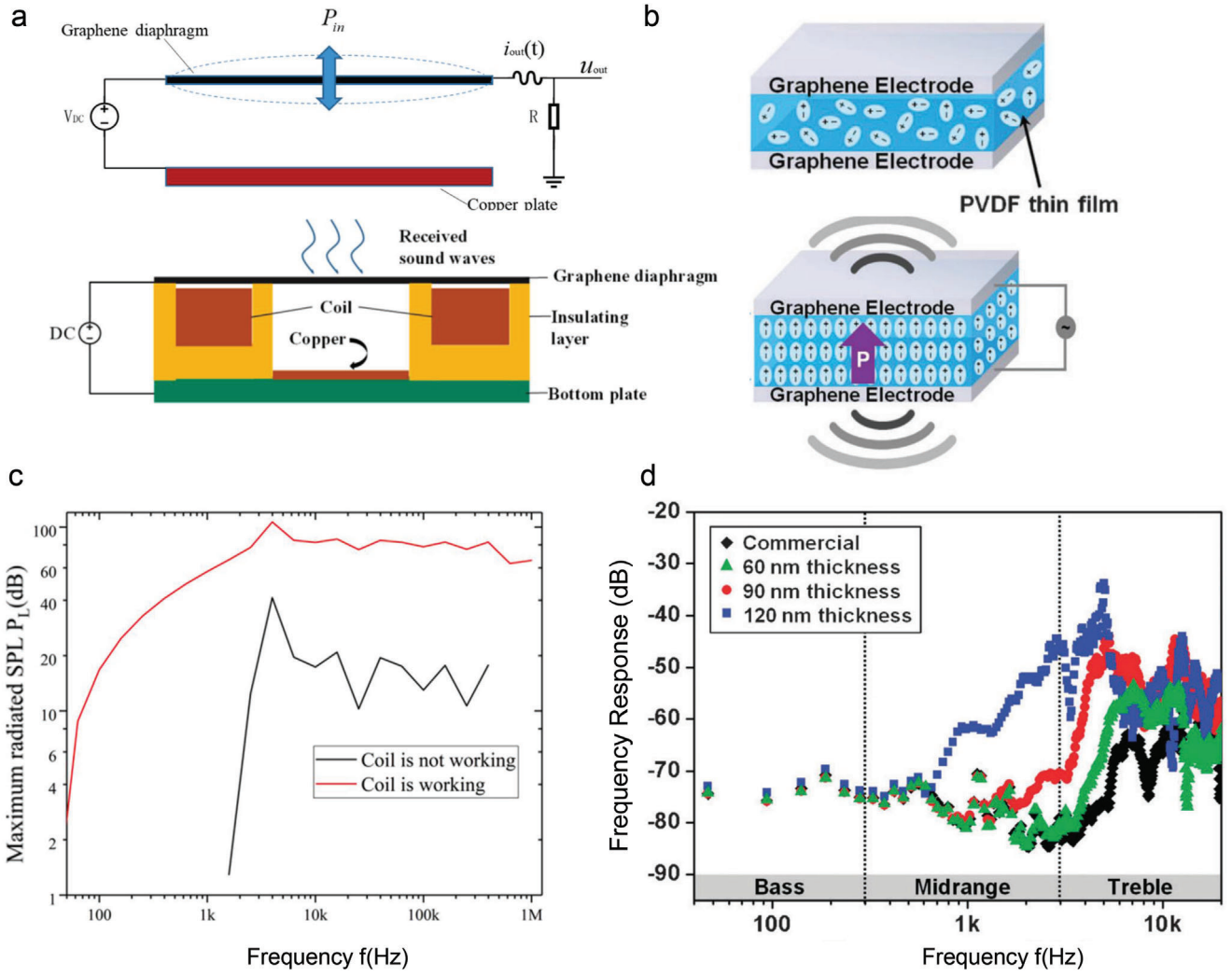


**Figure 6.** Other types of electric speakers based on suspended 2D materials. a) Structure of electrodynamic graphene speaker based on suspended graphene diaphragm. The implanted coil structure provides a magnetic field that generate Ampere force for the energetic graphene diaphragm. Reproduced with permission.[5] Copyright 2021, Elsevier B.V. b) Structure of the piezoelectric speaker with a graphene/PVDF GPC diaphragm. It generates sound via inverse piezoelectric effect. Reproduced with permission.[138] Copyright 2011, Royal Society of Chemistry. c) SPL output of the electrodynamic graphene speaker. It shows that the working coil generates higher and more stable output SPL, given by the red line, compared the speaker in which the coil structure does not work, given by the black line. Reproduced with permission.[5] Copyright 2021, Elsevier B.V. d) SPL output of the piezoelectric speaker at different thickness of graphene component. GPC diaphragm with thicker graphene generates lower resonant frequency and higher SPL output. It is clear that performance of speakers with GPC diaphragms containing 60–120 nm thickness graphene components are all better than PEDOT:PSS-based commercial speaker. Reproduced with permission.[138] Copyright 2011, Royal Society of Chemistry.

the insulation layer beneath the diaphragm (**Figure 6**a). This new configuration allows the coil to generate a magnetic field within the plane of the conductive diaphragm. When the diaphragm is energized with alternating current, it experiences periodic electromagnetic forces. .[5,137] Given that it also possesses capacitor structure, this speaker's diaphragm also experiences electrostatic forces similar to those in an electrostatic speaker, so the vibration amplitude of diaphragm can be increased by this method. Guo et al. provided a detailed analysis and demonstration of this method (Figure 6a). Test results shows that the output SPL of this electrodynamic graphene speaker is almost doubled compared to the no-coil electrostatic speaker under the same conditions (shown in Figure 6c), within nearly the whole frequency range. However, it is noteworthy that the Joule heat loss from the conducting coil consumes a lot of energy, leading to much lower energy efficiency than electrostatic speakers. Overall, the development of this type of electrodynamic speakers is not yet fully mature, and its feasibility requires further verification and demonstration indeed.

*Piezoelectric Speakers*: Piezoelectric speakers operate mainly based on the inverse piezoelectric effect of their piezoelectric diaphragms, whose vibration is generated in pace with the AC voltage supplied[138] (as shown in Figure 6b). Denote the internal stress of the piezoelectric diaphragm as $\sigma$. $V_B$ is applied bias voltage on both sides of the piezoelectric film and $\bar{e}_{31}$ is the diaphragm's out-of-plane inverse piezoelectric coefficient (which


© 2023 Wiley-VCH GmbH

16163028, 0, Downloaded from https://onlinelibrary.wiley.com/doi/10.1002/adfm.202303519 by Peking University Health, Wiley Online Library on [07/10/2023]. See the Terms and Conditions (https://onlinelibrary.wiley.com/terms-and-conditions) on Wiley Online Library for rules of use; OA articles are governed by the applicable Creative Commons License

16163028, 0, Downloaded from https://onlinelibrary.wiley.com/doi/10.1002/adfm.202303519 by Peking University Health, Wiley Online Library on [07/10/2023]. See the Terms and Conditions (https://onlinelibrary.wiley.com/terms-and-conditions) on Wiley Online Library for rules of use; OA articles are governed by the applicable Creative Commons License

means the voltage on z-direction induces the deformation on x or y-direction). As it is defined,

$$\bar{e}_{31} = e_{31} - \left(\frac{c_{13}^E}{c_{33}^E}\right) e_{33} \tag{12}$$

where $e_{31}$ and $e_{33}$ are piezoelectric coefficient of bulk material, $c_{13}^E$ and $c_{33}^E$ are the bulk stiffness coefficient.[139] The diaphragm deforms $w$ under bias voltage $V_B$,

$$w = \frac{1}{2\sqrt{3}} \frac{\bar{e}_{31} V_B}{\sigma t \sqrt{\frac{\delta}{\gamma_o}}} \tag{13}$$

where $\sigma$ is the internal stress of diaphragm. For an isotropic elastic diaphragm, the edge tension $\gamma_0$, bending modulus $D$ and sheet stiffness $\delta$ are given by,

$$\gamma_0 = j_1 \frac{\sigma t}{a^2} \tag{14}$$

$$D = \frac{1}{12j} \frac{E}{1-\nu^2} \frac{t^3}{a^4} \tag{15}$$

$$\delta = j_2 \frac{E}{1-\nu^2} \frac{t}{a^4} \tag{16}$$

where $\nu$ is the Poisson's ratio and $j_1$, $j_2$, $j$ are parameters of the side dimensions aspect ratio. A larger deformation of diaphragm is needed for a larger SPL output, so the following steps can be consulted to improve the speaker's acoustic output: 1) decrease the bulk stiffness of diaphragm material to enlarge the bulk piezoelectric coefficient $\frac{\bar{e}_{31}}{e}$; 2) lower the diaphragm's thickness and enlarger its radius to make smaller $\delta$, so as to increase $w$; 3) reduce the internal stress $\sigma$ of the diaphragm, which has been illustrated in detail in Section 2. Thin-film piezoelectric material such as flexible Polyvinylidene fluoride (PVDF) membranes are promised to meet the above demands. In this scenario, applying an appropriate electric structure to PVDF films plays a crucial role in the performance of piezoelectric speakers. Graphene/PVDF composite (a type of GPC), which incorporates conductive graphene film structure, is one of the newly proposed methods for piezoelectric speakers. Due to the thinness of graphene electrodes, the nonlinear interaction between the diaphragm and the electrodes may not be very strong.[129] This potentially promotes better uniformity of the material and helps reduce acoustic harmonic distortion. In 2011, Shin et al. prepared a PVDF piezoelectric speaker based on a graphene transparent electrode (as in Figure 6b).[138] Its standard SPL test (shown in Figure 6d) illustrates that at higher frequencies, the output SPL is around 10 dB stronger than commercial microphones. Xiao et al. then prepared the reduced graphene oxide/PVDF (rGO/PVDF) sound generator and realized a synergy of thermal drive in pace with piezoelectric drive.[140] Other piezoelectric materials can also be combined with graphene to fabricate GPC speakers with improved performance. Kholkin et al. further spin-coated a graphene layer on piezoelectric $Si_3N_4$, inducing the inverse piezoelectric response of 14 nm $V^{-1}$, higher than that of graphene/PVDF structure.[141] The combination of the graphene electrode with materials such as lead zirconate titanate (PZT),[142] lithium niobate (LN),[143] barium titanate (BT),[144] $LiNbO_3$[145] and $BaTiO_3$[146] etc. is promised to inspire new applications in high-quality sensors.

The roles of 2D materials in piezoelectric speakers are not limited to being used merely as an electrode structure. Some non-centrosymmetric 2D crystals also exhibit piezoelectric effects on their own.[147] In 2002, Mele and Král predicted the possible piezoelectric effect in hexagonal boron nitride (h-BN) nanotubes.[148] In 2014, Wu et al. detected the piezoelectric polarization in 2D molybdenum disulfide ($MoS_2$) for the first time.[149] Relevant scholars carried out extensive exploration on other 2D materials with stable piezoelectric polarization, which can be generally divided into the following categories: III–V semiconductors (such as h-BN),[150] II–V semiconductors,[151] TMDs (such as $MoS_2$, $MoSe_2$, $WSe_2$, etc.) and transition metal dioxides ($MoO_2$, $WO_2$, etc.),[152] group IV metal monosulfide compounds (such as SnSe, SnS, GeSe, GeS, etc.),[153] MXene,[154] Janus TMDs (such as MoSSe, MoSTe),[155] etc. The work of these 2D films utilized alone as the diaphragm in piezoelectric speakers is relatively rare, thus this is an area worth further exploration in the future.

In summary, the working principle of a piezoelectric speaker relies on the vibration generated by the inverse piezoelectric effect. It does not require a DC bias or coils structure, resulting in a simpler vibrating system that can be fabricated into compact, arbitrarily shaped microdevices. Compared to other types of speakers, piezoelectric speakers have resonant peak at higher frequencies and exhibit significant good performance in the higher frequency range.[13,132] However, piezoelectric speakers have a narrow frequency response and poor low-frequency performance, making them unsuitable for reproducing a wide range of sounds.[156] Given that the low-frequency performance of piezoelectric speakers is primarily influenced by the thickness of the diaphragm given that its vibration mode and frequency are determined by its thickness.[157] Ultrathin 2D materials and their composites meet this requirement for tunable low thickness, which holds significant importance for achieving more tunability of piezoelectric speakers.

#### *3.1.3. Thermoacoustic Speakers Based on 2D Materials and Their Composites*

By subjecting the surrounding air to periodic joule heating, accomplished by applying AC voltage to heat the thermoacoustic speaker's heating film (as illustrated in **Figure 7**a), air molecules will undergo cyclical thermal convection and produce vibrations in the form of pressure waves. Thus it is able to generate sound wave without the need for a vibrating diaphragm structure. The thermal energy power generated by the thermoacoustic speaker is described by the following formula,[28,158]

$$\begin{aligned} \text{Power}\ (\tau) &= \frac{\left(V_{AC}\sin(\omega\tau)+V_B\right)^2}{R} \\ &= \frac{1}{R}\left(-\frac{{V_{AC}}^2}{2}\cos(2\omega\tau) + 2V_{AC}V_B\sin(\omega\tau) + \frac{{V_{AC}}^2}{2} + V_B^2\right) \end{aligned} \tag{17}$$

where $V_{AC}$ is the driving AC voltage amplitude and $\omega$ is the driving angular frequency, $V_B$ is the bias voltage and $R$ is the device resistance. A smaller device resistance contributes to a larger output acoustic power. The impact of heat loss in this structure

 © 2023 Wiley-VCH GmbH

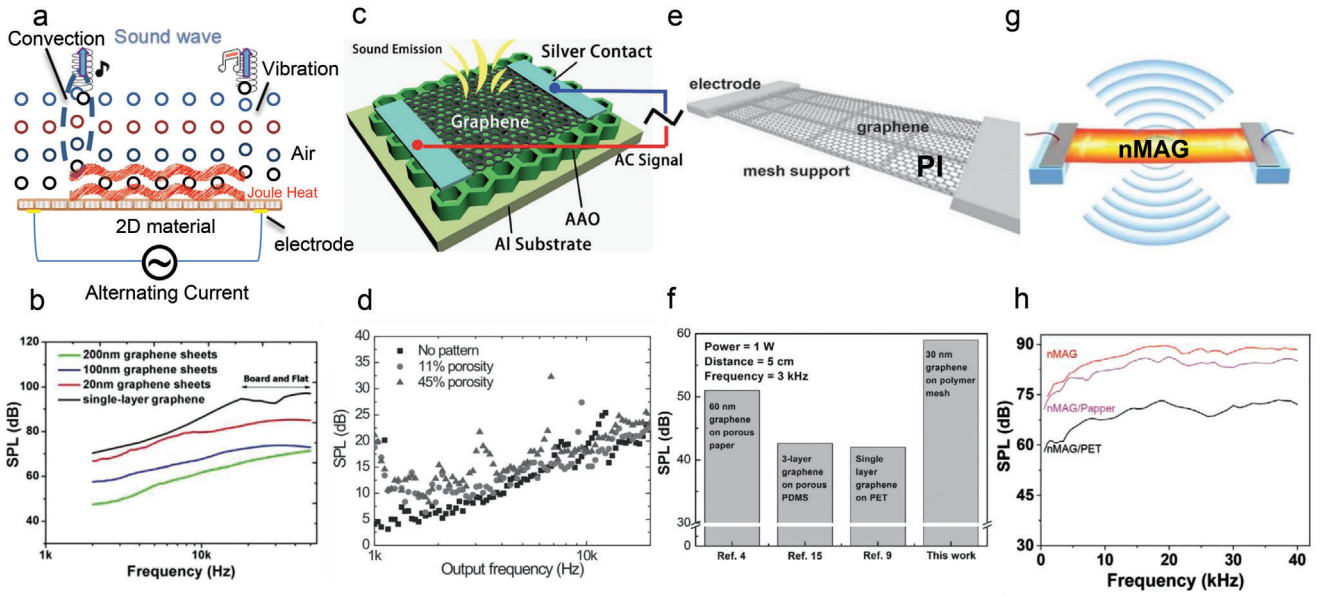


**Figure 7.** Structures and SPL output performance of thermoacoustic speakers. a) Schematic of general type thermoacoustic speaker. b) Output SPL of graphene sound-emitting devices with various graphene thickness and c) schematic of an AAO-based sound source device. Single layer graphene shows higher SPL and more flat bandwidth. Reproduced with permission.[162] Copyright 2012, Royal Society of Chemistry. d) Output SPL of graphene suspended on porous substrate. Increasing of porosity has positive effective on SPL output. Reproduced with permission.[160] Copyright 2012, Wiley-VCH. e) Schematic and f) output SPL of GPC diaphragms with different components among which graphene/polymer mesh GPC shows highest SPL output. Reproduced with permission.[163] Copyright 2015, Wiley- VCH. g) Schematic and h) output SPL of nMAG multifunctional diaphragm. Pure suspended nMAG diaphragm shows the larger SPL output than other GPC based on nGAG. Reproduced with permission.[57] Copyright 2021, Wiley-VCH .

cannot be eliminated, as indicated by the last two terms of Equation (17). Consequently, a significant amount of energy loss is inevitably generated, resulting in relatively low energy conversion efficiency for practical thermoacoustic speakers.

One of the factors that affects the performance of thermoacoustic speakers is the thermal diffusion length.[159] This is the distance that heat can travel in air medium during one cycle of the sound wave. If the thermal diffusion length is larger than the thickness of the speaker's heating film, then the heat will not be confined to the speaker surface and will dissipate into the surrounding fluid. This will reduce the efficiency and sound pressure level of the thermoacoustic speaker. So the thermal convection must be fast enough to suppress heat loss, which results in poor low-frequency performance of the thermoacoustic speaker. Another factor that influences the performance of thermoacoustic speakers is the heat capacity of the speaker material. The heat capacity determines how much heat is needed to change the temperature of the material. A low heat capacity means that a small amount of heat can cause a large temperature change, which is desirable for thermoacoustic speakers. Therefore, materials with smaller heat capacity per unit area (HCPUA) are strongly demanded here. 2D materials, such as graphene and MXene, possess much lower HCPUA than bulk materials, which is suitable for newly developed thermoacoustic heating structure. We will mainly discuss thermoacoustic speakers based on these 2D materials in the following text

*Graphene-Based Thermoacoustic Devices*: Reducing the heat loss of the substrate is significant for thermoacoustic devices.[160] Relevant research have suggested various types of suspension structure of heating film for reducing the contact ratio between substrate and heating film, so as to achieve louder thermoacoustic output. In 2011, Tian et al. reported the design of the graphene thermoacoustic speaker for the first time.[161] They utilized paper to suspend 20–100 nm multilayer graphene as GPC heating film. Standard SPL test at a distance of 5 cm presents a linear relationship between SPL and frequency between 3 kHz and 20 kHz. The device has shown an exciting flat and wide SPL output both in audio frequency and in low ultrasound frequency (shown in Figure 7b).

Subsequently, researchers discovered that by progressively reducing the thickness of the graphene membrane in thermoacoustic speakers, a significant increase in SPL output was observed. This increase can be attributed to the amplified HCPUA of the thinner graphene membrane, resulting in a relatively higher energy conversion efficiency compared to the thicker graphene membranes. In 2012, Tian et al. fabricated the first suspended thermoacoustic device (shown in Figure 7c) using monolayer graphene on porous anodic aluminum oxide (AAO) as GPC heating film.[162] This innovation resulted in a significant increase in the maximum output SPL compared to the previously prepared heating film with 20 nm multilayer graphene (Figure 7b), showing an enhanced SPL of 10 dB under the same conditions. This increase in SPL is precisely attributed to the reduction in thickness, which leads to a decrease in the heat capacity per unit area (HCPUA). Suk et al. almost simultaneously developed thermoacoustic devices with similar structures by combining SLG with polydimethylsiloxane (PDMS), PET, and other materials to form GPC heating films.[160] The prepared device has good transparency and flexibility. Furthermore, the impact of the suspension degree on the output performance of the


© 2023 Wiley-VCH GmbH

16163028, 0, Downloaded from https://onlinelibrary.wiley.com/doi/10.1002/adfm.202303519 by Peking University Health, Wiley Online Library on [07/10/2023]. See the Terms and Conditions (https://onlinelibrary.wiley.com/terms-and-conditions) on Wiley Online Library for rules of use; OA articles are governed by the applicable Creative Commons License

16163028, 0, Downloaded from https://onlinelibrary.wiley.com/doi/10.1002/adfm.202303519 by Peking University Health, Wiley Online Library on [07/10/2023]. See the Terms and Conditions (https://onlinelibrary.wiley.com/terms-and-conditions) on Wiley Online Library for rules of use; OA articles are governed by the applicable Creative Commons License

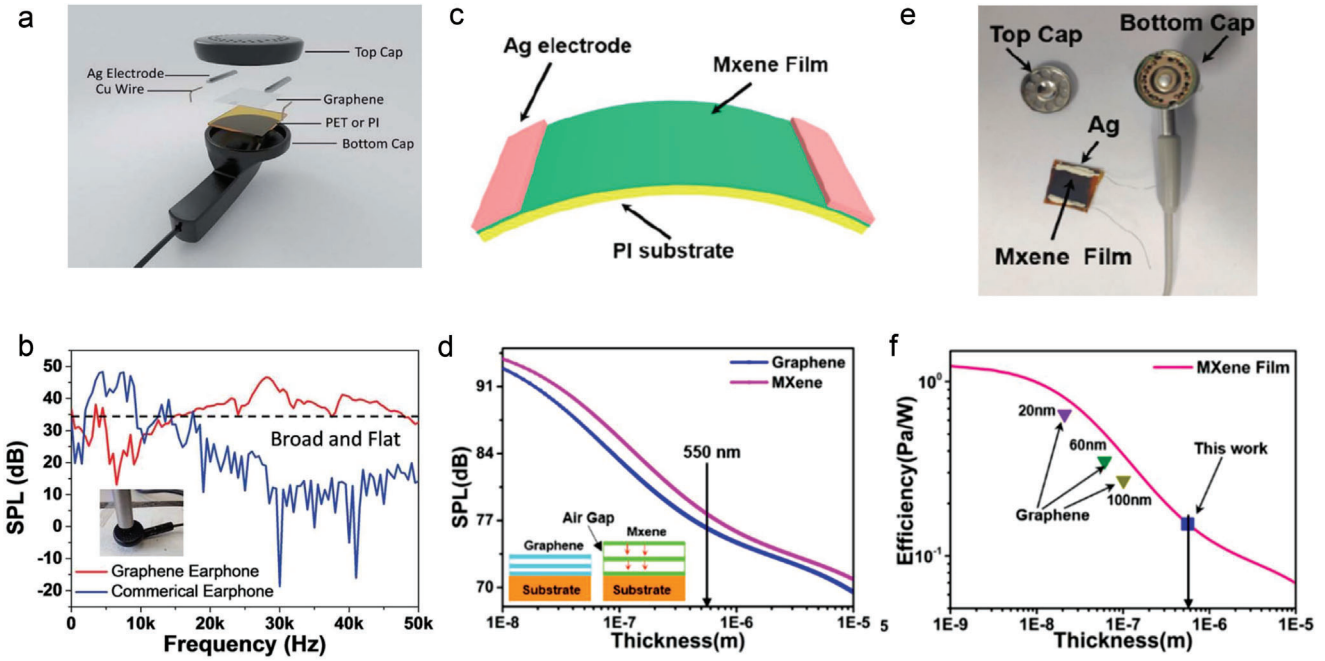


**Figure 8.** Typical structure and performance of 2D material earphones. a) Structure and b) SPL output of the earphones. GPC based earphone shows a higher SPL output and broader bandwidth in relatively high frequency compared with commercial earphones. Reproduced with permission.[166] Copyright 2015, Royal Society of Chemistry. c) Structure and d) SPL output of the MXene/PI composite speaker. With the same thickness, the diaphragms based on MXene shows a higher SPL output than the diaphragms based on graphene. Reproduced with permission.[167] Copyright 2019, American Chemical Society. e) Structure and f) energy efficiency of the MXene based earphone with different thickness. The energy efficiency of the MXene based earphones are slightly higher than the graphene based earphones with same diaphragm thickness, potentially due to its lower HCPUA. Reproduced with permission.[167] Copyright 2019, American Chemical Society.

thermoacoustic speaker is further investigated by modifying the porosity of the patterned $SiO_2$/Si substrate while keeping the graphene-based heating films intact. It is observed that as the porosity of the substrate gradually decreases, the thermal conductivity of the substrate also decreases. Simultaneously, the SPL output increases by 10 dB on the substrate with 45% porosity compared to the non-porous substrate. (shown in Figure 7d). Kim et al. combined 28 nm multilayer graphene on the PI mesh to form another GPC heating film (shown in Figure 7e).[163] The results of standard acoustic tests demonstrate the positive proportional relationship between the porosity of PI and the SPL output of the thermoacoustic speaker again, which is consistent with the results founded by Suk et al. The SPL output of the device is further improved by over 10 dB in low frequencies compared to speakers without a PI base (as depicted in Figure 7f), demonstrating an enhancement in the low-frequency performance of the speaker.

Increasing the diameter to thickness ratio of the heating film is expected to be another method for improving the acoustic performance of thermoacoustic speakers. Asaad et al. employed a graphene/PMMA GPC heating film with a diameter to thickness ratio of $10^5$ and, successfully improved the flatness of sound output at lower frequencies. Gao et al. proposed a "cooling-contraction" method for synthesizing macro-assembled graphene nanofilms (nMAG) and utilized them to create a heating film with a large lateral size of 4.2 cm and a thin thickness ranging from 16 to 48 nm.[57] The diameter to thickness ratio of these devices can exceed $10^6$, also the tensile strength of these films can reach 5.5 to 11.3 GPa with excellent conductivity between 1.8 and 2.1 MS $m^{-1}$ (depicted in Figure 7g). The fully suspended configuration among these films has shown the highest 89 dB SPL output (as shown in Figure 7h). Additionally, it boasts an ultrafast electric-thermal response rate of 30 µs.

Gate modulation of thermoacoustic materials is also a significant technique for enhancing thermoacoustic output. Zhang et al. developed a thermoacoustic transducer using CVD-grown woven graphene diaphragms. Through precise adjustment of the gate voltage, the SPL output of this transducer can be comparable to that with monolayer graphene heating film.[164] In a similar vein, Heath and Horsell fabricated a graphene field-effect transistor (FET) device and potentially demonstrated the feasibility of producing wearable earphones based this flexible graphene-based heating film.[165] In 2015, Tian et al. developed almost the first bendable 2D material thermoacoustic earphones combined graphene with PET and PI as the GPC heating film[166] (the earphone's structure is illustrated in **Figure 8**a). It is demonstrated that GPC with SLG component exhibits the smoother and louder SPL output of approximately 70 dB, showing higher quality than commercial earphones as well (Figure 8b). Further design of more efficient circuit tuning structures and the fabrication of heating film materials with lower HCPUA and higher diameter to thickness ratios will contribute to the practical production of high-performance advanced thermoacoustic earphones in the future research.

*MXene-Based Thermoacoustic Devices*: In addition to graphene, researchers have also explored thermoacoustic

 © 2023 Wiley-VCH GmbH

devices based on other 2D materials, such as MXene and its composite materials. In 2019, Gou et al. successfully fabricated the $Ti_3C_2$-MXene-based thermoacoustic speakers composited with anodized aluminum oxide (AAO) and flexible PI films (the speaker structure is depicted in Figure 8c).[167] MXene, unlike graphene, possesses terminal hydrophilic groups on its surface, which makes it easier for self-assembly into a diaphragm. Therefore, this MXene based composite film has the potential to achieve a larger diameter to thickness ratio. Also the average interlayer distance of MXene is approximately 1.31 nm, approximately three times of multilayered graphene, resulting in a lower HCPUA. These characteristics make MXene-based films an important material for thermoacoustic speaker heating films.

Tian et al. further fabricated thermoacoustic earphones based on this material (Figure 8e). Increasing the thickness of the MXene film similarly resulted in the decreasing of SPL output (as shown in Figure 8d). However, under the same conditions, the SPL output of MXene was clearly higher than that of graphene, potentially due to its lower HCPUA. The energy efficiency of MXene is also found to be higher than graphene (calculation results are displayed in Figure 8f). However, it should be noted that the energy efficiency of MXene-based films, like other thermoacoustic speakers films using 2D materials, typically ranges from $10^{-8}$ to $10^{-6}$. This presents a significant disadvantage compared to other types of speakers, especially electrostatic speakers that achieve energy conversion efficiencies close to 100%.[11]

In summary, thermoacoustic speakers offer several advantages compared to other types of speakers: 1) They do not rely on a vibrational diaphragm structure, making them more reliable and easier to fabricate in various sizes and shapes with lighter weight. 2) They have a relatively wide frequency range, allowing for versatile audio reproduction. 3) Unlike electrostatic speakers, thermoacoustic speakers do not require high voltage supply, making them safer for daily use. The thin thickness, low HCPUA, high conductivity, large diameter to thickness ratio, and good tunability of 2D materials are advantageous for fabricating thermoacoustic speakers with higher energy efficiency and improved acoustic performance. However, thermoacoustic speakers also have certain disadvantages, such as the relatively poor low-frequency performance and weak energy conversion efficiency. In the future, thermoacoustic structures can be further integrated with energy-related issues, such as waste heat recycling, playing more significant roles in specific heating configurations.

### 3.2. Microphone: Detection of Acoustic Wave

The devices used to receive acoustic waves and convert them into human recognizable signals are called microphone. Microphones can be classified into several types based on their sound detection principles: 1) dynamic and ribbon microphones[1] (also known as electrodynamic microphones, **Figure 9**a); 2) condenser microphones[3] (Figure 9b); 3) piezoelectric microphones[6] (Figure 9c); 4) piezoresistive microphones[2] (also known as contact microphones) (Figure 9d). The aforementioned four main types of microphones are all based on circuit design. Other newly developed types such as fiber-optic microphones (FOMs) [168] (Figure 9e) and acoustic laser vibrometers[169] (Figure 9f) possess no circuit structure, which are also able to detect acoustic wave with ultrahigh sensitivity.

The electrodynamic microphone, depicted in Figure 9a, is the most commonly used type of microphone. It consists of a diaphragm, a wire coil, and a magnet structure. The coil attached to the diaphragm moves along the magnet in response to external sound waves, inducing a corresponding electrical current. This structure is relatively simple in design (do not require a built-in preamplifier) with acceptable acoustic distortion and low production costs. However, electrodynamic microphones have some inherent drawbacks. Typically, this structure exhibits a low-frequency resonance peak around 2.5 kHz, which limits its response to higher frequencies. This resonant peak also may cause distortion and coloration of the sound.[170,171] The relatively heavy coil structure's inertia makes the microphone less responsive to subtle pressure variations, severely limiting its sensitivity. There have been some advancements in combining 2D material diaphragms, such as graphene,[5,137] with electrodynamic speakers, serving as updated versions of dynamic microphones. However, there is no clear evidence indicating that these developments significantly enhance the performance of the microphone. Consequently, electrodynamic microphones are not recommended for new generation high-quality sound receptors.

For evaluation of the other type potential high-performance microphones, three main parameters are typically considered: sensitivity, bandwidth (which is related to the quality factor), and dynamic range (DR) .[7,172] The mechanical sensitivity of the diaphragm material is defined as the normal deflection of the membrane caused by external pressure of one unit strength, which can be expressed as,[2,7]

$$S_{\mathrm{m}} = \frac{\Delta\omega}{\Delta P} = \frac{a^2}{8\sigma_0 t} \tag{18}$$

And the DR are defined as follows

$$\mathrm{DR} = \frac{P_{\max}}{P_{\mathrm{n}}} \tag{19}$$

where $P_{\max}$ is maximum non-distorted detected pressure and $P_{\mathrm{n}}$ is pressure noise caused by Brownian motion of air molecular as given below,[173]

$$P_{\mathrm{n}}^2 = \frac{4k_{\mathrm{B}}T\omega_0 m_{\mathrm{eff}}}{A^2 Q} \tag{20}$$

In this formula, $k_{\mathrm{B}}$ is Boltzmann constant, $A$ is the area of the diaphragm, $T$ is temperature, $Q$ is the quality factor, $\omega_0$ is the resonance angular frequency and $m_{\mathrm{eff}}$ is the effective mass. From Equation (20), we know the larger diameter to thickness ratio significantly enhances the mechanical sensitivity of the diaphragm, which is highly consistent with the characteristics of 2D materials. However, for electric microphones, the specific circuit structure also influences the electrical detection sensitivity,[29,174] so proper circuit design should be also detailly considered. We will first discuss the performance improvement of the circuit based advanced microphones through different 2D materials with their composites. After that we will discuss newly developed microphones that do not require circuit structures, such as FOMs and acoustic laser vibrometers.


© 2023 Wiley-VCH GmbH

16163028, 0, Downloaded from https://onlinelibrary.wiley.com/doi/10.1002/adfm.202303519 by Peking University Health, Wiley Online Library on [07/10/2023]. See the Terms and Conditions (https://onlinelibrary.wiley.com/terms-and-conditions) on Wiley Online Library for rules of use; OA articles are governed by the applicable Creative Commons License

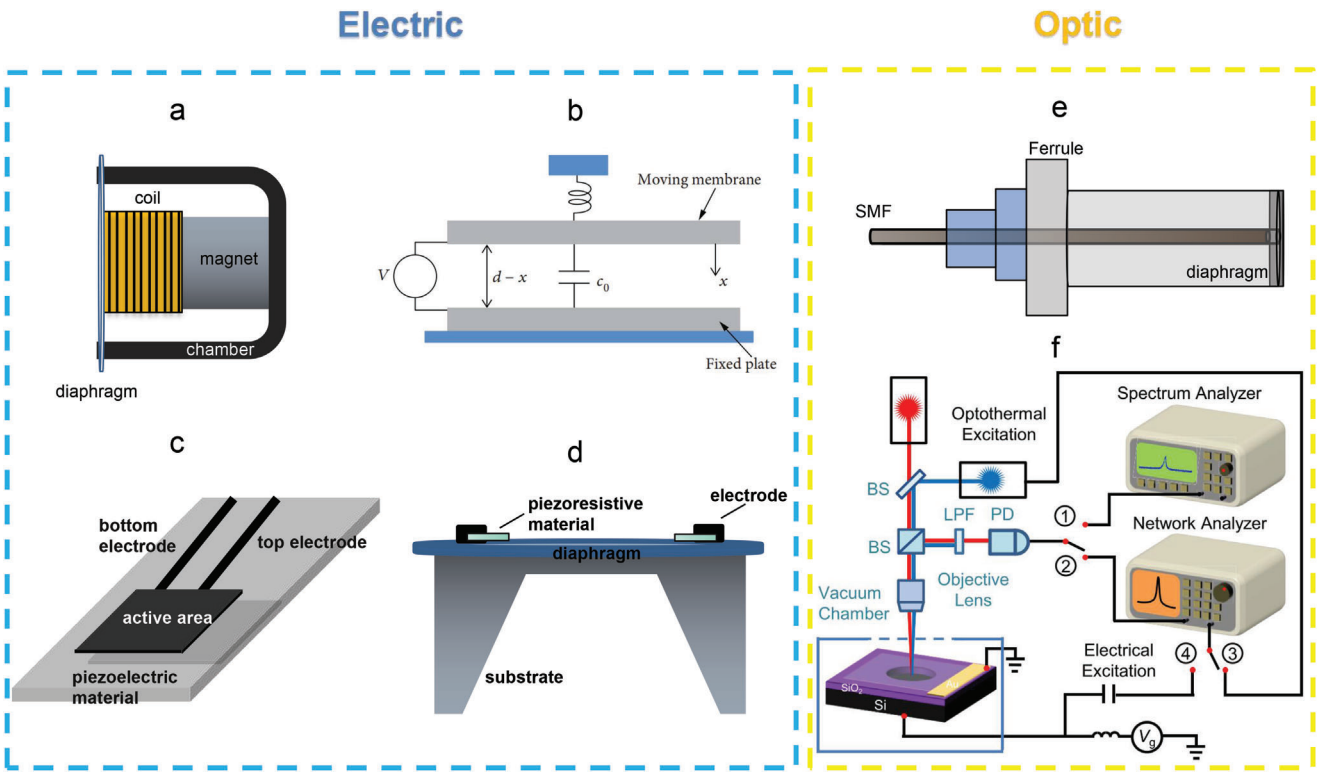


**Figure 9.** Various types of sound detection devices. a) Electrodynamic microphone (moving coil microphone) where vibrating diaphragm generates transient current (used for sound recording) through electromagnetic induction process. b) Condenser microphone, modeled as parallel plate capacitor. The transient current is generated by changing of capacitance. Reproduced under the terms of the CC-BY license.[7] Copyright 2019, Hindawi. c) Piezoelectric microphone, generating transient current through piezoelectric effect. d) Piezoresistive microphone, inducing changing resistivity through piezoresistive effect. These four types of microphones all based on electric readout principles. e) Fiber optic microphone (FOM). An Fabry-Pérot interferometer structure are integrated on the tip of optic fiber in order to detect the vibration of diaphragm sensitively by analyzing the interference of beams. f) Acoustic laser interferometer, which is able to detect the small displacement of diaphragm vibration up to femtometer magnitude, utilizing interference optical setups. Red laser with wavelength 633 nm serves as probe light and the purple laser with wavelength 405 nm is able to tune the vibration through photothermal effects. Method e) and f) are based on optical detection principles. Reproduced with permission.[212] Copyright 2022, American Chemical Society.

### *3.2.1. Condenser Microphones Based on 2D Materials and Their Composites*

Among the various types of electrical microphones, condenser microphones are known for their higher sensitivity and wider, flatter bandwidth response. Generally, the parallel plate capacitor model can accurately describe this type of microphone (as shown in Figure 9b). In this model, one end of the plate is connected to the diaphragm to form a capacitor.[7] To charge the capacitor, a constant voltage $V$ is applied. When the capacitor is disturbed by an external acoustic wave, its value changes due to small deviations in the plate spacing. This induces a transient current given by the equation,

$$I(\tau) = V\frac{\mathrm{d}}{\mathrm{d}\tau}C(\tau) \tag{21}$$

where $C(\tau)$ is the capacitance at time $\tau$. The acoustic signal input to the microphone can be encoded by this time-dependent current.

Electrical sensitivity is a measure of how much output voltage a microphone produces for a given SPL at a certain frequency. It is usually expressed in dBV/Pa or mV/Pa. Traditional condenser microphones have higher sensitivity than electrodynamics microphones because they use a preamplifier, which can increase the signal level. In addition, the use of high-performance diaphragm materials can greatly enhance the mechanical sensitivity of condenser microphones. The relative electrical sensitivity and absolute electrical sensitivity are determined by the following formulas,

$$S_{\mathrm{C}} = \frac{\partial}{\partial P}\left(\frac{\Delta C}{C_0}\right) = -\frac{\partial}{\partial P}\left(\frac{\Delta d}{d_0}\right) \tag{22}$$

$$S_{\mathrm{C}}^{\mathrm{A}} = \frac{\partial}{\partial P}\left(\frac{\Delta C}{A}\right) \tag{23}$$

where $P$ is sound pressure, $C_0$ is the original capacitance, $d_0$ is the equilibrium plate spacing, $\Delta C$ is the change of capacitance under sound wave, $\Delta d$ is the change of plate spacing, and $A$ is plate area. Higher device sensitivity can be achieved by adjusting the applied voltage $V_{\mathrm{B}}$, decreasing the spacing $d$, and enlarging the diaphragm area $A$. This can be easily achieved by 2D materials and their composites.


© 2023 Wiley-VCH GmbH

16163028, 0, Downloaded from https://onlinelibrary.wiley.com/doi/10.1002/adfm.202303519 by Peking University Health, Wiley Online Library on [07/10/2023]. See the Terms and Conditions (https://onlinelibrary.wiley.com/terms-and-conditions) on Wiley Online Library for rules of use; OA articles are governed by the applicable Creative Commons License

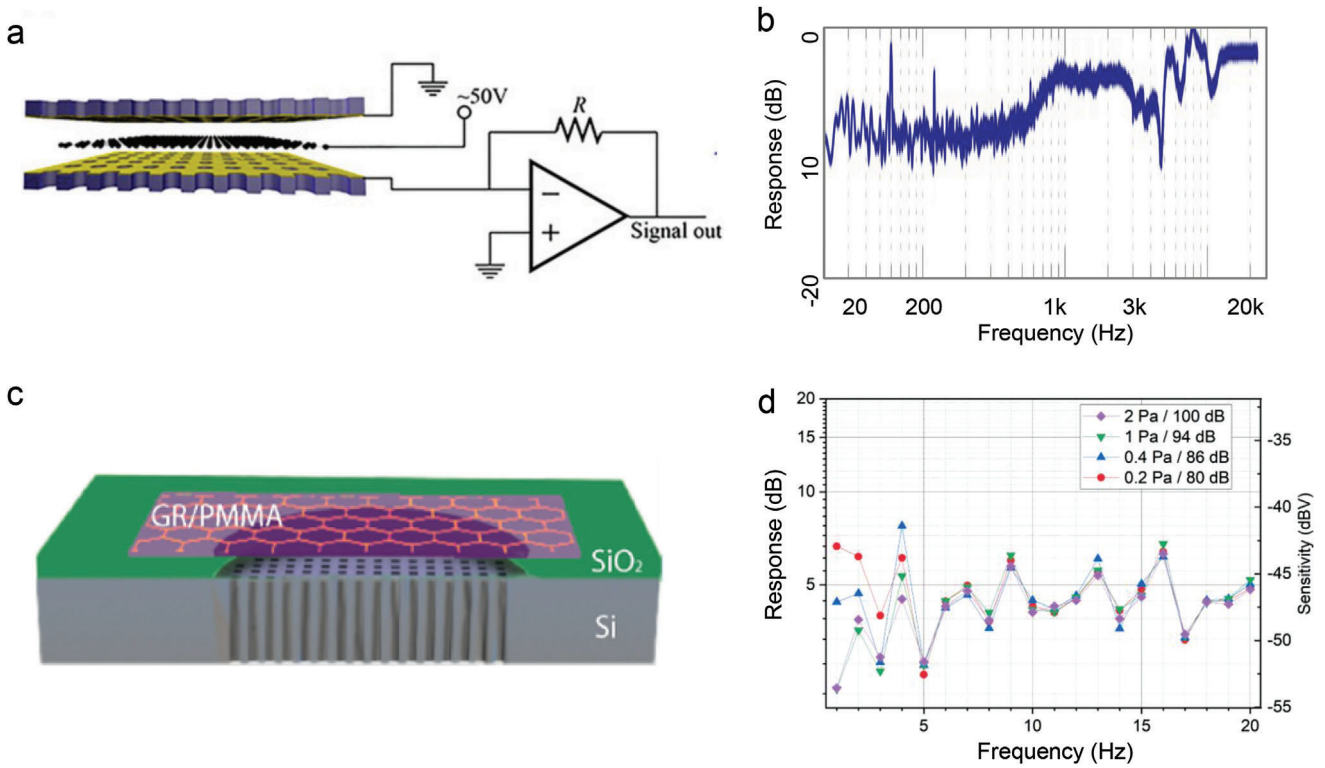


**Figure 10.** Graphene based condenser microphones. a) Schematic of the first condenser microphone, where graphene diaphragm is suspended on the support frame, with designing of the fast-photodiode detector-like circuit which enables consistent gain at higher frequency. Reproduced with permission.[26] Copyright 2015, National Academy of Sciences. b) Acoustic response of the first graphene condenser microphone, which shows broad bandwidth and flat frequency response. Reproduced with permission.[26] Copyright 2015, National Academy of Sciences. c) Schematic and d) acoustic response of graphene microphone with only 8 µm plate spacing. Under different external pressure this microphone shows broad and flat bandwidth response. Reproduced with permission.[183] Copyright 2021, American Chemical Society.

2D materials, such as graphene-based materials, typically offer good flexibility and can be prepared into large-area conductive diaphragms with ultrathin thickness. In recent times, there has been ongoing research to combine these materials with microphone diaphragms, aiming to create microphone structures with ultrahigh sensitivity. For example, Todorović et al. suggests a graphene based microphone in a similar structure as B&K Type 4134 earphones in 2015,[175] whose diaphragm is pure graphene film with a 5 mm diameter and a thickness of nearly 25 nm, showing obviously enhanced sensitivity compared with B&K Type 4134 earphones. Zhou et al. developed an optimized graphene condenser microphone (**Figure 10**a) using a graphene film approximately 60 layers with a diameter of 7 mm.[26] This graphene diaphragm possesses a much larger diameter to thickness ratio than Todorovic's microphone. To reduce the parasitic capacitance between the microphone and amplifier, they employed a cross-impedance amplification circuit and additionally, they installed a cavity on one side of the microphone electrode so as to enhance the low-frequency stability of their microphone (with frequency response shown in Figure 10b). Test results demonstrated a flat acoustic response with wiggles of less than 10 dB across the entire audio frequency range. Also this device had a bandwidth far exceeding that of other commercial microphones, typically having a 140 kHz bandwidth. The low spring constant and large diameter to thickness ratio of the graphene film are potential reasons for the ultrahigh sensitivity and wide bandwidth of this microphone. Chen et al. later built an acoustic sensor with suspended graphene diaphragm of 1.5 mm wide and 5 layers thick,[176] a larger diameter to thickness ratio compared to Zhou's microphone. The sensitivity of this device reached approximately 15.2 aF $Pa^{-1}$, nearly 50% higher than the general Si-based thin-film sensors. Mustapha et al. then conducted more targeted research specially on the diaphragm diameter and prepared monolayer graphene diaphragms with diameters ranging from 15 µm to 40 µm.[177] Test results showed that, with the same thickness, the device with the largest diameter exhibited the highest sensitivity (approximately 20 dB larger compared to the diaphragm with the smallest radius) and the most flat bandwidth response. In general these microphones based on 2D materials possess sensitivity comparable to or exceeding −42 dBV $Pa^{-1}$ at 1 kHz,[178] much higher than the commercial nickel-based microphone with a sensitivity of −52 dBV $Pa^{-1}$.[179] However, due to the ultrahigh sensitivity and excellent performance of these microphones, they can pick up more background noise than other types of microphones. Therefore, it is necessary to introduce appropriate noise reduction structures to further enhance sound quality.

Optimizing transfer methods and aiming to achieve lossless production of 2D material films are beneficial for realizing the fabrication of suspended diaphragms with larger diameter to thickness ratios and enhanced stability. Carvalho et al. developed


© 2023 Wiley-VCH GmbH

16163028, 0, Downloaded from https://onlinelibrary.wiley.com/doi/10.1002/adfm.202303519 by Peking University Health, Wiley Online Library on [07/10/2023]. See the Terms and Conditions (https://onlinelibrary.wiley.com/terms-and-conditions) on Wiley Online Library for rules of use; OA articles are governed by the applicable Creative Commons License

the sublimation-assisted transfer process and achieved the larger area suspension of graphene diaphragms.[180] The largest suspended diaphragm possessed a diameter of 4 mm with a thickness of only about 3.7 nm. They selected an 1 mm diameter diaphragm with thickness around 1 nm to build a condenser microphone. Acoustic test results showed that the sensitivity of the microphone increased by an average of 22 dB across the entire audio frequency range compared to the reference microphone. The larger diameter to thickness ratio with weaker internal stress is the reason for the higher sensitivity of this microphone, which highly demonstrates the suitability of 2D materials in enhancing microphone sensitivity. However, the transfer process discussed above may inevitably cause wrinkles and cracks, which can have a detrimental impact on the stability, lifespan, as well as the maximum achievable diameter to thickness ratio of the diaphragm. This is another aspect that can be further optimized in the transfer of 2D material films. Pezone et al. aimed at this and initially grew graphene films on silicon wafers and then built a cavity by etching silicon perforations on the backward substrate.[181] This allowed to directly suspend the graphene diaphragm on the opposite surface without the need for a transfer process. The suspended diaphragms possess diameters up to 155 μm with thickness of about only 7 nm, simultaneously have lower extent of wrinkles and defects. The fabrication yield of this method reached close to 100%, with the diaphragm's mechanical sensitivity achieving approximately 92 nm $Pa^{-1}$, much higher than most commercial microphone diaphragms (approximately 3 nm $Pa^{-1}$). This method is beneficial for avoiding large-scale wrinkles and cracks in suspended 2D diaphragms, and it facilitates the realization of prestress control of microphone diaphragms as described in Section 2.

Condenser microphones need a bias voltage because they work on the principle of capacitance. As mentioned above, the changes of capacitance can produce a small transient signal for recording. However, this AC signal is too weak to be used directly. It needs to be amplified by a preamplifier circuit inside the microphone. To power this circuit, a DC voltage is needed. This is called the bias voltage or phantom power. The bias voltage also serves another purpose: it polarizes the capacitor formed by the diaphragm and the backplate. This means that it creates an electric field between them so that it is able to tune the sensitivity and frequency response of the microphone. Relevant experiments are demonstrated by Mustapha et al.[177] When the bias voltage is increased until the diaphragm collapses and touch the back plate, defining the maximum applied voltage as the "pull-in" voltage, it can be expressed in the following formula,[7]

$$V_{\mathrm{PI}} = \sqrt{\frac{8kd^3}{27\epsilon A}} \tag{24}$$

where $\epsilon$ is permittivity in cavity. From this formula we can see the "pull-in" voltage of a microphone depends on several factors, such as the size, shape, material, the distance and configuration of the electrodes, the air gap between the diaphragm and the back plate. Also the internal stress of the diaphragm affects the deflection of the diaphragm, so it impacts the "pull-in" voltage. The "pull-in" voltage of the condenser microphone is a critical parameter because it determines the upper limit of the bias voltage that can be used to power the microphone and tune its sensitivity and frequency response.

Typically the bias voltage is limited under 60% of the "pull-in" voltage to avoid instability and nonlinear effects. Therefore, how to avoid diaphragm "pull-in" while ensuring high stability and sensitivity of the microphone with the smallest possible plate spacing is a major challenge in recent research on microphones based on 2D materials and their composites such as graphene and GPC. It has been reported that by utilizing graphene/PMMA GPC diaphragm, the condenser microphone can achieve an equilibrium plate spacing of only 10 μm.[182] Test results demonstrate that the microphone's detection sensitivity has reached approximately -20 dB, surpassing almost all traditional electret condenser microphones (ECM) by more than 9 dB, with the dynamic range of about 90 dB. Xu et al. reported the development of an alternative approach for fabricating a suspended graphene/PMMA condenser microphone, employing an improved preparation method that eliminates the need for transfer. This was achieved by selectively etching the $SiO_2$ sacrificial layer beneath the film, as illustrated in Figure 10c.[183] This method enabled the microphone's plate spacing to reach 2 μm, nearly the minimum plate spacing for graphene-based condenser microphones, with the diameter to thickness ratio of the diaphragm reaching up to 7800. The estimated average sensitivity for this device was valued at 4.22 ± 10% mV $Pa^{-1}$ (around −47.5 dB V) (Figure 10d). These results offer promising advancements for miniaturized acoustic devices used on chips. However, studies in this area are still limited, and the consideration of synergistic conditions related to plate spacing decreasing is not yet sufficient. Therefore, further research on plate spacing necessitates more comprehensive discussions and investigations.

Another crucial aspect of condenser microphone research is the type of bias voltage. The effects of DC bias voltage and AC bias voltage on the performance of capacitive microphones have been explored in the early researches.[184] As previously discussed, DC bias voltage can be modulated to achieve a high signal-to-noise ratio and wide frequency response. However, it can also lead to issues such as DC drift and offset, which can impact the accuracy and stability of the microphone signal. To mitigate this effects of DC bias voltage, researchers have utilized oscillating circuits within the microphone or preamplifier to generate AC bias voltage, which has shown effectiveness. Nevertheless, the introduction of AC voltage may introduce inevitable harmonic distortion and noise into the microphone output signal, potentially reducing sensitivity and dynamic range. Given the recent researches, the incorporation of 2D material diaphragms is able to optimize performance of capacitive microphones to a mechanistic level, so by employing appropriate control variable methods, it will play as a solid platform for further investigation about the impact of AC bias on microphone performance.

In summary, condenser microphones based on 2D materials and their composites offer the main advantages of ultrahigh sensitivity and large bandwidth compared with other types of microphones as well as condenser microphones with diaphragms made of traditional bulk materials. Optimizing the bias voltage tuning of capacitive microphones, investigating the comprehensive impact of plate spacing, and designing more reasonable noise reduction circuit structures will be crucial for


© 2023 Wiley-VCH GmbH

16163028, 0, Downloaded from https://onlinelibrary.wiley.com/doi/10.1002/adfm.202303519 by Peking University Health, Wiley Online Library on [07/10/2023]. See the Terms and Conditions (https://onlinelibrary.wiley.com/terms-and-conditions) on Wiley Online Library for rules of use; OA articles are governed by the applicable Creative Commons License

the development of the next generation of microphones. It is essential to comprehensively consider factors such as sound quality, bandwidth, dynamic range, and sensitivity in order to achieve significant advancements in condenser microphone technology.

### 3.2.2. Other Types of Electric Microphones Based on 2D Materials and Their Composites

*Piezoresistive Microphones*: The piezoresistive effect was firstly discovered by Lord Kelvin in around 1856.[185] However, the significant large piezoresistive effect in silicon and germanium that could be used in piezoresistive microphones was first discovered by Smith et al. in 1954.[7,186] A piezoresistive microphone is designed with a diaphragm incorporating two pairs of piezoresistors arranged in a Wheatstone bridge configuration (as shown in Figure 9d). When exposed to mechanical stress or strain induced by sound waves, the piezoresistive diaphragm undergoes a corresponding change in resistance, synchronizing with the vibrations. This alteration in resistance leads to changes in output current signals, enabling the microphone to capture and record acoustic signals. Similar to the discussion on transient current in condenser microphones, the output current change in piezoresistive type microphones is also very small.[187] So it typically requires the preamplifier to provide the necessary gain and enable impedance matching for the output signal. Also the bias voltage is needed as a constant current excitation to the piezoresistive element.[188] Parameters related to the properties of piezoresistive microphones are described in Section 4.1.

2D materials and their composites, such as GPC, are projected to be fabricated into piezoresistive microphones given that some 2D materials and their composites exhibit high gauge factors (which measure the extent of resistance change with strain and generally, materials with higher gauge factors possess stronger piezoresistive characteristics) .[6,29,189–201] However, currently, there is limited literature on 2D material-based piezoresistive microphones. One possible reason for this scarcity of research may be due to the inherent drawbacks of piezoresistive microphones, including a limited dynamic range and poor sensitivity.[187] Therefore, further research is needed to explore this field. Piezoresistive microphones are mainly modified into MEMS devices and primarily employed in the field of static pressure sensing, working as piezoresistive pressure sensors. These sensors address the limitations of traditional piezoelectric and capacitive sensors. Combined with 2D material based diaphragms, they are able to possess ultrahigh sensitivity and tunable bandwidth.[28,202] In Section 4.1, we will delve into a detailed discussion of those high performance piezoresistive pressure sensors based on 2D materials and compare them with the traditional acoustic sensors.

*Piezoelectric Microphones*: Piezoelectric microphones are devices that use the piezoelectric effect to convert sound vibrations into electrical signals. Piezoelectric microphones are typically composed of a thin piezoelectric material sandwiched between two electrodes, such as a traditional quartz, ceramic, or polymer film (as shown in Figure 9c). Recently, 2D material based piezoelectric thin films are developed as a new generation of piezoelectric material. When sound waves hit the piezoelectric material, it deforms and generates a potential difference between the electrodes as the output signal, without the need of an externally applied polarizing voltage. However it requires a preamplifier to amplify the output voltage of the piezoelectric microphone to the level that can be processed by the subsequent circuitry. Therefore, developing a well-designed and sophisticated circuit for the piezoelectric microphone, which facilitates easy miniaturization and integration, holds significant research importance.

Piezoelectric microphones, in general, offer advantages such as high sensitivity, a wide frequency range, and low noise compared to other types of microphones. The output energy and size of piezoelectric microphones can be optimized based on the input pressure, bandwidth, and different piezoelectric materials. Thinner piezoelectric films generally exhibit better transient response, while a larger area results in a greater effect of sound waves on the diaphragm, leading to the generation of more output charge and increased sensitivity. From this, it can be observed that 2D materials with ultralarge area and atomic thinness are highly beneficial for enhancing microphone sensitivity.[6,203,204] Additionally, atomic thin films of 2D materials are so flexible that they can rapidly respond to sound waves of different frequencies, resulting in a broader resonance bandwidth.

However, it is important to note that these microphones also have drawbacks, including high impedance, temperature dependence, and aging effects. Considering that the output signal current is very small, it results in a high output impedance. High impedance means that the piezoelectric microphone requires an amplifier with a high input impedance to amplify the signal; otherwise, signal loss and related errors may occur. The sensitivity and frequency response of the piezoelectric microphone also vary with temperature, as temperature affects the polarization, elasticity, and thermal expansion properties of the piezoelectric material. Temperature dependence implies that the piezoelectric microphone needs a compensation circuit to correct the signal in case of the distortion and drift. Furthermore, the performance of the piezoelectric microphone deteriorates over time. The polarization properties of the piezoelectric material gradually degrade over periods, leading to a decrease in sensitivity and stability. This means that the piezoelectric microphone requires an aging testing and calibration process to ensure its accuracy and consistency of the signal. In summary it is necessary to control the experimental conditions and implement appropriate compensation strategies to optimize test accuracy considering the limitations of the piezoelectric microphone.

It is worth noting that, up to this point, only a limited number of composite materials comprising 2D materials and piezoelectric polymers have been successfully used in the fabrication of piezoelectric microphones. Wang et al. utilized a PVDF-fluoridetrifluoroethylene (TrFE)/MXene material to construct a pressure sensor where MXene enhances the piezoelectric polarization of PVDF,[205] showing improved sensitivity compared with pure PVDF piezoelectric film. Graphene is also utilized as conducting electrode component in GPC combined with piezoelectric materials such as PVDF, PZT, and other piezoelectric materials.[206,207] In these structure, the graphene electrode is lightweight and thin, which promotes the device transparency.

However, it should be noticed that pure MXene films and other 2D materials have hardly been experimentally fabricated into


© 2023 Wiley-VCH GmbH

16163028, 0, Downloaded from https://onlinelibrary.wiley.com/doi/10.1002/adfm.202303519 by Peking University Health, Wiley Online Library on [07/10/2023]. See the Terms and Conditions (https://onlinelibrary.wiley.com/terms-and-conditions) on Wiley Online Library for rules of use; OA articles are governed by the applicable Creative Commons License

16163028, 0, Downloaded from https://onlinelibrary.wiley.com/doi/10.1002/adfm.202303519 by Peking University Health, Wiley Online Library on [07/10/2023]. See the Terms and Conditions (https://onlinelibrary.wiley.com/terms-and-conditions) on Wiley Online Library for rules of use; OA articles are governed by the applicable Creative Commons License

piezoelectric microphones, though various types of 2D materials, such as BN, TMDs (such as $MoS_2$, $WS_2$) has shown out-of-plane ferroelectric effect.[208,209] This could be attributed to the insufficient piezoelectric coefficient of these pure 2D materials and the challenging of transfer processes, which makes it difficult to be directly fabricated into piezoelectric thin films with reliable acoustic performance. With recent advancements in newly developed materials such as Janus TMDs with out of plane symmetry broken, it as a promising new 2D material for producing high-performance piezoelectric speakers. In the future, significant breakthroughs are anticipated to be made for those concept-based piezoelectric speakers such as single atomic layer piezoelectric speakers etc., as the further development of transfer and preparation processes.

#### 3.2.3. Optical Sound Detectors

Optical sound detection methods directly capture the mechanical vibrations of the diaphragm using interference, reflection, and other techniques. These methods offer higher sensitivity and greater convenience compared to electric detection methods. FOMs and laser vibrometers are typical examples of optical acoustic detection devices, which will be discussed in the following sections

*Fiber Optic Microphones (FOMs)*: Conventionally, FOMs are fabricated in the following steps: Firstly, researchers insert an optical fiber into the outer ferrule and precisely control the small distance between the end of the optical fiber and the ferrule port. Then, they integrate a 2D material diaphragm (such as graphene) onto the ferrule port, forming a Fabry-Perot interferometer (FPI) structure with the end of the optical fiber. By using a photodetector (PD) or other equipment to detect interference fringes or reflection spectra, the vibration amplitude and frequency of the graphene diaphragm can be deduced through spectrum analysis (the general structure of a FOM is shown in Figure 9e).

The detection intensity $I_{out}$ is the sum of reflections from the optical fiber end and the membrane, given by the following equation with reflectivity denoted by $R_1$ and $R_2$,[210]

$$I_{out} = \left(R_2 + \xi R_1 - 2\sqrt{\xi R_1 R_2}\cos\theta\right) I_i \tag{25}$$

where $\theta$ is phase difference between two reflected beam, generally the value is $\theta = 4\pi L/\lambda$. $I_i$ is the intense of input light while $\xi$ is coupling constant given by,

$$\xi = \frac{4\left[1 + \left(\frac{2\lambda L}{\pi N_0 a_0^2}\right)^2\right]}{\left[2 + \left(\frac{2\lambda L}{\pi N_0 a_0^2}\right)^2\right]^2} \tag{26}$$

where $\lambda$ is guiding wavelength in length $L$ cavity, $N_0$ is refractive index (approximately 1 for air medium) and $a_0$ is the radius of mode field (typically 4.9 μm for SMF-28 single-mode fiber). The change of cavity length caused by vibration is the deflection of diaphragm $w$, then the absolutely contrast of reflected light is given by,

$$\Delta I = \frac{8\pi}{\lambda} I_i \sin\frac{4\pi L}{\lambda}\sqrt{\xi R_1 R_2} w \tag{27}$$

The photodetector responses to the detected light intensity with output voltage $V_{out} = RI_{out}$, so the deformation $w$ of diaphragm can be inferred from intensity variation with the formula given as,

$$w = \frac{\lambda\left(R_2 + \xi R_1\right)\left(V_{out} - V_0\right)}{8\pi V_0\sqrt{\xi R_1 R_2}} \tag{28}$$

where $V_0$ is equilibrium output voltage of PD at no sound. From this, we can express the total external sound pressure $P$ of as,

$$P = \frac{B_1\sigma_0 t w}{a^2} + \frac{B_2 E t w^3}{(1-\nu)a^4} \tag{29}$$

where $B_1$, $B_2$ are dimensionless indices. Equations (27) to (29) indicate that the deformation of FOM diaphragm and vibrations of external acoustic pressure can be directly analyzed from the output optical signals of the FOM. Remind that the mechanical sensitivity of the FOM is determined by Equation (18),

$$S_m = \frac{\Delta\omega}{\Delta P} = \frac{a^2}{8\sigma_0 t} \tag{30}$$

Due to the controllable internal stress and high diameter to thickness ratio of suspended 2D materials and their composite diaphragms, their mechanical sensitivity can be significantly adjusted. With the capability to directly capture the vibration signal of the diaphragm, the FOMs based on 2D materials and their composites can exhibit a notable measurement sensitivity to sound pressure fluctuations, given that the measurement equipment is well optimized. As a result, these materials hold promising prospects for next-generation high-performance microphones. Similar principles can also be applied to pressure sensing. Further details regarding these FOMs and pressure sensors with similar structures will be discussed in Section 4.2.1.

In summary, the magnitude of deformation $w$ affects the cavity length of the FP cavity, which in turn affects the intensity of the interfering light. Therefore, by directly measuring the intensity of the interfering light, we can accurately determine the deformation of the diaphragm thus achieving precise measurement accuracy.

The reflectivity of the 2D material based diaphragms also has an impact on experimental measurements. From Equation (27), it can be observed that the change in light intensity is directly proportional to the square root of $(R_1 R_2)$, the multiplication of the material reflectivity of 2D material and optical fiber base. Hence, using 2D material based diaphragms with higher reflectivity is advantageous for enhancing the intensity of the effective interference signal, thereby improving the resolution of thin film deformation. Furthermore, it can be deduced that adjusting the appropriate cavity length, employing suitable wavelengths, and selecting 2D materials with higher reflectivity all contribute to improving the precision of optical vibration measurements.

*Laser Vibrometers for Sound Detection*: The vibration of the diaphragm can be directly detected by laser vibrometers. Various types of laser vibrometers are shown in **Figure 11**. Davidovikj et al. employ a He–Ne laser to create a laser vibrometer, in which the laser is directed onto the underlying 2D material. The incident light undergoes multiple reflections at each


© 2023 Wiley-VCH GmbH

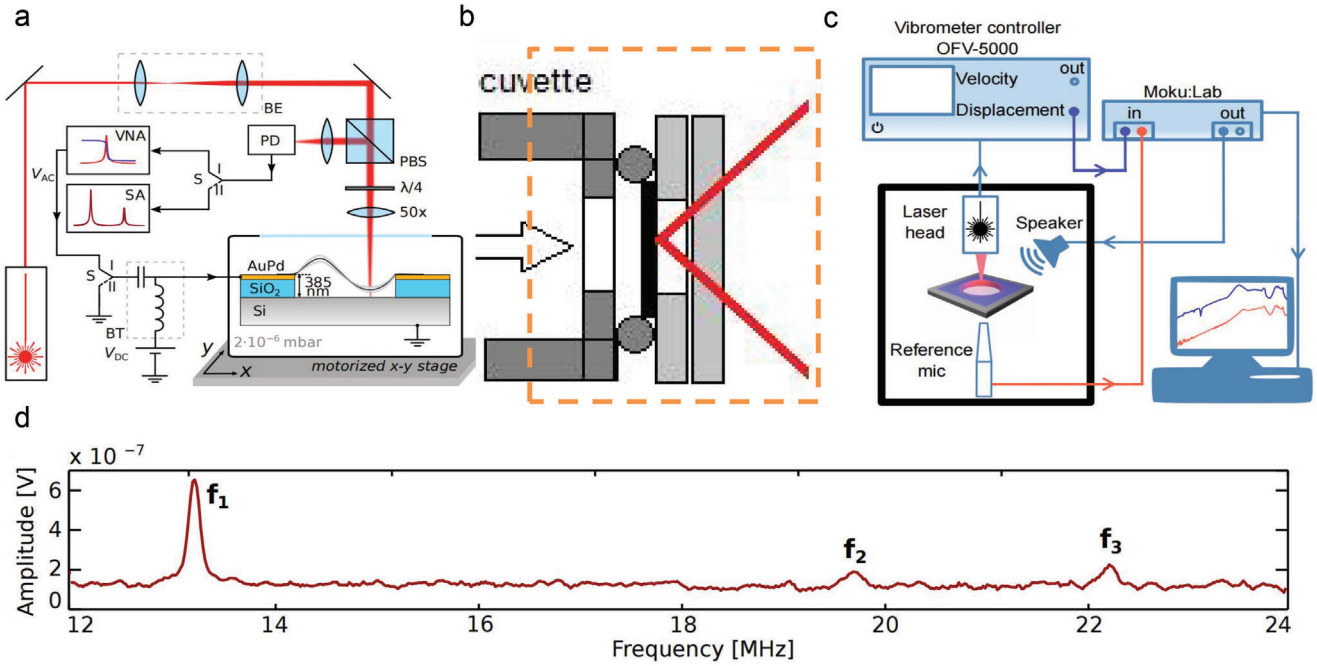


**Figure 11.** Laser vibrometers for high quality sound detection. a) Interference interferometer which detects the vibration form the interference of beams after penetrating the vibrating films. Large resolving power and broad bandwidth covering several Megahertz can be detected by this method. Reproduced with permission.[211] Copyright 2016, American Chemical Society. b) Laser vibrometer based on reflection method, with similar principle as atomic force microscope tips, where the vibration of film is magnified by light reflection. Reproduced under the terms of the CC-BY license.[213] Copyright 2015, Crown. c) Laser Doppler Vibrometer, which can directly readout the vibration frequency and amplitude with relatively lower frequency and larger displacement. The resolution of this method is able to reach several femtometers. Reproduced with permission.[214] Copyright 2023, Royal Society of Chemistry. d) High-sensitive broadband spectrum measured by laser interferometers, possessing broadened response and high sensitivity in ultrasonic frequency range which will be discussed in the following sections. Reproduced with permission.[211] Copyright 2016, American Chemical Society.

interface, resulting in periodic vibrations that cause alterations in the spectrum of interference intensity.[211] This enables the measurement of vibration amplitude and frequency with high sensitivity (Figure 11a). This method can detect the vibration mode of graphene film under high-frequency drive and measure the thermal fluctuations of suspended 2D material without external drive (Figure 11d). The displacement resolution of this interferometer reaches an ultrahigh value of 11 fm $Hz^{-1/2}$. Similar methods have also been developed by Wang et al.[169,212] which accurately detect the ultrasonic resonant behavior of 2D material-based mechanical resonators. However, it is important to note that this method is more suitable for acoustic measurement at high frequencies with smaller vibration amplitudes that are less than one wavelength of the probe light in order to generate effective interference.

Other methods have been developed to accurately detect acoustic vibrations at lower frequencies. Zelinger et al. developed a method (Figure 11b) that utilizes a silicon cantilever coupled with a multilayer graphene film, employing similar principles as the atomic force microscopy (AFM) tip.[213] This method allows direct analysis of vibrations from beam reflection signals. However, the sensitivity and signal-to-noise ratio (SNR) of this method have not been proven to be more precise than acoustic detection using high-quality microphones. Another commonly used method, as described by Baglioni et al., is to employ a laser Doppler vibrometer (LDV), such as the OFV-5000 vibrometer controller, to accurately measure the mechanical and vibration properties of microphones diaphragms (as shown in Figure 11c).[214] The instantaneous velocity of the film vibration can be accurately determined by measuring the Doppler frequency shift of small regions where incident light interferes with reflected beams of known wavelengths. By counting the light and dark stripes of the interference spectrum on the LDV, the amplitude of the film vibration can be resolved down to the femtometer level.[215,216]

The utilization of laser vibrometers to characterize the acoustic vibration of diaphragms offers a simple and fast way to achieve highly accurate detection. However, their application is limited due to the expensive equipment involved, making them unsuitable for large-scale industrial usage. Optical sound detection methods, in general, provide ultrahigh sensitivity and SNR due to their direct interaction with diaphragm vibrations, similar to how our eyes perceive moving objects, without the need for cumbersome circuit analysis as in electric detection methods (where accuracy mainly depends on circuit impedance characteristics). Nonetheless, the method described above still has certain limitations, including high costs, limited applicability for large-scale industrialization, and poor environmental stability. There is potential for further research and development in optical detection technology, such as the area of array sensing technology. This approach involves integrating FOM arrays with varying geometric parameters. By analyzing and interpreting the combined detection results, it is anticipated that a broader frequency bandwidth and greater sensitivity for acoustic vibration sensing can


© 2023 Wiley-VCH GmbH

16163028, 0, Downloaded from https://onlinelibrary.wiley.com/doi/10.1002/adfm.202303519 by Peking University Health, Wiley Online Library on [07/10/2023]. See the Terms and Conditions (https://onlinelibrary.wiley.com/terms-and-conditions) on Wiley Online Library for rules of use; OA articles are governed by the applicable Creative Commons License

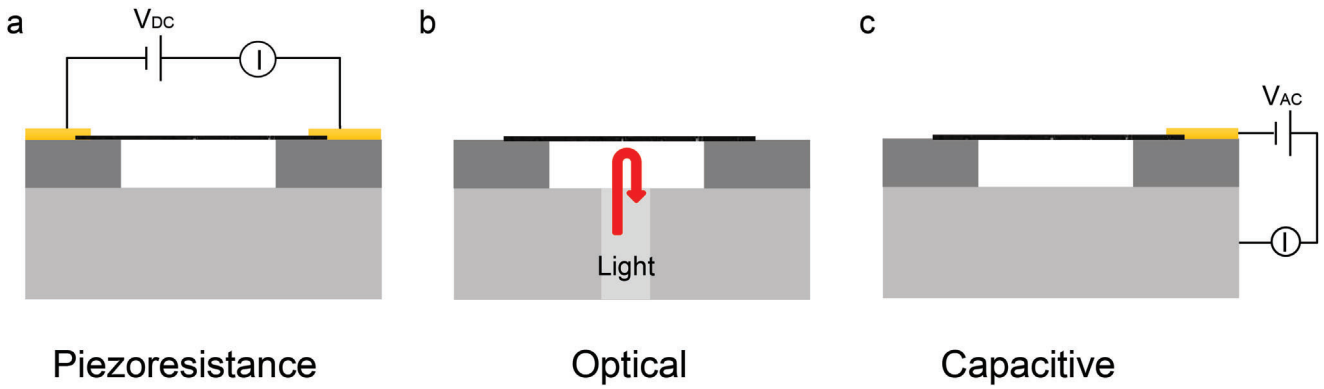


**Figure 12.** Pressure detection methods. a) Piezoresistive: the resistance of the membrane depends on the strain of the membrane. b) Optical: the reflected light signal depends on the displacement of the center point of the membrane. c) Capacitive: the capacitance between the membrane and the electrode depends on the average displacement of the whole membrane.

be achieved. In conclusion, the optical sound detection technology is expected to find increased development and utilization in the future, particularly in the field of ultrahigh accuracy acoustic detection.

## 4. Static Pressure Sensors

Pressure sensors are widely used in both industrial monitoring and everyday life. They are commonly manufactured as MEMS devices that convert external pressure into electrical or optical signals. However, the increasing demand for high-performance pressure sensors brought about by the Internet of Things has placed greater emphasis on the sensitivity and size of these devices.[28]

To meet these requirements, 2D materials have garnered attention due to their high surface area, making them an attractive option for developing highly sensitive pressure sensors with small dimensions. This section will focus on pressure sensors for static pressure, while resonant pressure sensors for high-frequency sensor devices will be discussed in the section 5.

There are several methods available for measuring the deformation of suspended films, with two main types being strain-based and displacement-based pressure sensors. Strain-based pressure sensors detect changes in the resistance of the film under strain to measure pressure (**Figure 12**a), resulting in a linear response and a clear output signal. Displacement-based pressure sensors typically measure changes in displacement using optical (Figure 12b) or capacitive (Figure 12c) means and are less susceptible to environmental factors such as gas and humidity.

### 4.1. Strain-Based Pressure Sensors

Piezoresistive pressure sensors are a widely used pressure sensors, due to the fact that the resistance can be detected simply by a change in voltage or current in the circuit (Figure 12a). Piezoresistive pressure sensors function based on the principle of the piezoresistive effect.[28] The sensing element of the device, typically a suspended thin film, undergoes deformation under the influence of a pressure differential $\Delta P$, resulting in the introduction of a corresponding strain within the film. This strain causes a measurable change in the electrical resistance of the sensor, which can be accurately detected and quantified as a measure of the applied pressure. The extent of this effect is determined by the gauge factor (GF) of the material, which is the ratio of the relative change in resistance to the applied strain[217]

$$\mathrm{GF} = \frac{\mathrm{d}\varphi}{\varphi_0}\frac{1}{\mathrm{d}s} + (1+2\nu) \tag{31}$$

where $\varphi$ is the resistivity, $\varphi_0$ is the material's zero-strain resistivity, $s$ is the applied strain in the material, and $\nu$ is the Poisson ratio. Commercially available piezoresistive sensors predominantly utilize metal foils. However, due to the absence of a band gap in metals, their resistivity exhibits only marginal changes upon strain application, resulting in lower GF within the range of 1–5. In contrast, semiconductor materials possess a non-zero band gap and their intrinsic carrier density is dependent on the band gap. Strain application alters the energy band structure, thereby modulating the carrier density and yielding higher GF values.[218] The GF of $MoS_2$ are −148, −224, and −40 for monolayer, bilayer and trilayer, respectively.[219,220] Theoretical GF predictions for monolayer $WSe_2$ are about 3000.[221] The high piezoresistive coefficients make it possible to fabricate smaller and more sensitive pressure sensors from 2D materials.

In most cases, strain-based pressure sensors employ suspended films that are characterized by square geometries, as such configurations enable the attainment of elevated strain gradients. Relationship between center deflection and pressure difference of a square suspension membrane is described as[222]

$$P = \frac{C_1 t\sigma_0}{\left(\frac{l}{2}\right)^2}w + \frac{C_2 f(\nu)\, tE}{\left(\frac{l}{2}\right)^4(1-\nu)}w^3 \tag{32}$$

where $C_1$, $C_2$ are dimensionless constants, $\sigma_0$ is the prestress in the film, $l$ is the edge length of the film, $\nu$ is the Poisson's ratio, $f(\nu)$ is a geometric function, $t$ is the film thickness, $E$ is the Young's modulus and $w$ is the displacement at the centre of the film.


© 2023 Wiley-VCH GmbH

16163028, 0, Downloaded from https://onlinelibrary.wiley.com/doi/10.1002/adfm.202303519 by Peking University Health, Wiley Online Library on [07/10/2023]. See the Terms and Conditions (https://onlinelibrary.wiley.com/terms-and-conditions) on Wiley Online Library for rules of use; OA articles are governed by the applicable Creative Commons License

**Table 1.** Sensitivity comparison of different piezoresistive pressure sensors (N/A: specific parameter that is not provided by the authors).

| Author | Year | Material | Suspended area[a] [μm$^2$] | Test range [kPa] | Sensitivity [kPa$^{-1}$] | Sensitivity per unit area[b] [kPa$^{-1}$μm$^{-2}$] |
|---|---|---|---|---|---|---|
| Zhu et al.[226] | 2013 | Graphene/$SiN_x$ | 78400 | 0–70 | $6.67 \times 10^{-5}$ [c] | $8.50 \times 10^{-10}$ [c] |
| Smith et al.[195] | 2013 | Graphene | 384 | 40–100 | $2.96 \times 10^{-5}$ [d] | $7.71 \times 10^{-8}$ [d] |
| Wang et al.[227] | 2016 | Graphene/$SiN_x$ | 240100 | 0–40 | $2.8 \times 10^{-4}$ | $1.17 \times 10^{-9}$ [c] |
| Wagner et al.[230] | 2018 | $PtSe_2$/PMMA | 157 | N/A | $1.39 \times 10^{-3}$ [c] | $8.85 \times 10^{-6}$ [c] |
| Lin et al.[228] | 2019 | Graphene/PMMA | 1570 | 0–80 | $2.87 \times 10^{-5}$ | $1.83 \times 10^{-8}$ |
| Liu et al.[229] | 2020 | Graphene/PMMA | 602 | 0–70 | $7.42 \times 10^{-5}$ [d] | $1.23 \times 10^{-7}$ [d] |
| Gonzalez et al.[223] | 2012 | Silicon germanium | 62500 | 0–60 | $2.5 \times 10^{-5}$ | $4 \times 10^{-10}$ |
| Godovitsyn et al.[224] | 2013 | Silicon | 4000000[d] | 0–100[d] | $2.37 \times 10^{-4}$ [d] | $5.92 \times 10^{-11}$ [d] |

[a] the area of the suspended membrane; [b] Sensitivity per unit area = Sensitivity/suspended area; [c] From Ref. of Wagner et al;[230] [d] From Ref. of Liu et al;[229]

In the linear region characterized by small displacements, the displacement of the suspended film can be primarily attributed to the first term on the right-hand side of Equation (32). The thickness of the piezoresistive material is a critical parameter that significantly impacts the performance of the piezoresistive pressure sensors. Nevertheless, traditional piezoresistive materials encounter significant challenges in achieving very thin thicknesses, which can limit their performance in applications requiring high sensitivity. Suspended 2D materials with atomic-thin layer thickness offer a promising avenue for addressing the challenges associated with achieving ultrathin piezoresistive materials (**Table 1**) .[223,224] The mechanical sensitivity at the center of the film increases with the square of $(a/2)^2/t$, where $a$ is the length of the square membrane and $t$ is its thickness. Thus, a higher value of diameter to thickness ratio corresponds to a greater strain change inside the film for the same differential pressure, which in turn increases the sensitivity of the resistive device. In 2013, Smith et al. successfully fabricated suspended CVD monolayer graphene films on 6 × 64 μm$^2$ square cavities (**Figure 13**a).[195] The team demonstrated the piezoresistive effect of graphene in nanoelectromechanical thin film configuration, revealing an average GF of 2.9 and a sensitivity per unit

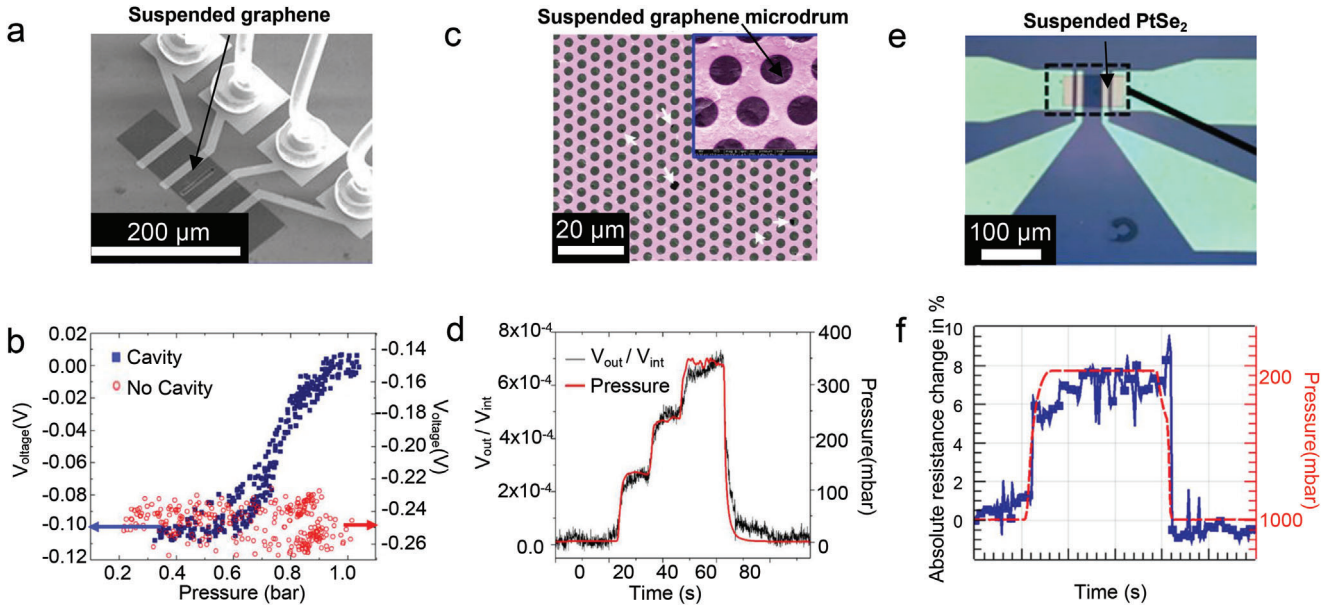


**Figure 13.** Strain-based pressure sensor. a) CVD monolayer graphene suspended on a 6 × 64 μm$^2$ rectangular cavity. Reproduced with permission.[195] Copyright 2013, American Chemical Society. b) The device in a) demonstrates the piezoresistive effect of graphene in a nanoelectromechanical film with a sensitivity per unit area of up to $7.71 \times 10^{-8}$ kPa$^{-1}$μm$^{-2}$. Reproduced with permission.[195] Copyright 2013, American Chemical Society. c) SEM image of ≈2 nm thick CVD graphene transferred on a suspended 490 × 490 μm$^2$ $SiN_x$ film with the through-hole arrays. Reproduced with permission.[227] Copyright 2016, Royal Society of Chemistry. d) The device in c) maintains a high sensitivity of $2.8 \times 10^{-6}$ kPa$^{-1}$ over a wide pressure range. Reproduced with permission.[227] Copyright 2016, Royal Society of Chemistry. e) Optical image of $PtSe_2$ on a 157 μm$^2$ cavity through PMMA-assisted suspension. Reproduced with permission.[230] Copyright 2018, American Chemical Society. f) Absolute resistance (left y-axis) and pressure (right y-axis) change for one pressure cycle (1000 mbar, pumped down to 200 mbar, 1000 mbar) of the device. Reproduced with permission.[230] Copyright 2018, American Chemical Society.


© 2023 Wiley-VCH GmbH

16163028, 0, Downloaded from https://onlinelibrary.wiley.com/doi/10.1002/adfm.202303519 by Peking University Health, Wiley Online Library on [07/10/2023]. See the Terms and Conditions (https://onlinelibrary.wiley.com/terms-and-conditions) on Wiley Online Library for rules of use; OA articles are governed by the applicable Creative Commons License

area of 7.71 × $10^{-8}$ $kPa^{-1}$ $\mu m^{-2}$ (Figure 13b). In 2014, they experimentally determined that biaxially strained CVD monolayers of graphene exhibited a higher average GF of 6.1.[225] Aside from pure 2D materials, it is also possible to produce suspended films by combining 2D materials with silicon-based materials. This approach can facilitate the transfer of suspended 2D materials and enhance their strain. A piezoresistive pressure sensor was proposed by Zhu and co-workers in 2013.[226] The sensor was created by transferring a CVD multilayer polycrystalline graphene film onto a suspended square silicon nitride ($SiN_x$) membrane that was suspended and had a side length of 280 μm and a thickness of 100 nm. The graphene was then selectively patterned in the area with the highest strain. Wang et al. have reported a method for enhancing the strain sensitivity of graphene-based pressure sensors.[227] They first created a 490 × 490 $\mu m^2$ $SiN_x$ membrane with an array of micropores and then transferred a large graphene film onto it (Figure 13c). The method resulted in a significant increase in strain on the graphene, thereby achieving a sensitivity of 2.8 × $10^{-4}$ $kPa^{-1}$ (Figure 13d).

In recent years, there have been significant progress on the development of larger-sized suspended films using polymer-assisted graphene. This approach has enabled the creation of films with increased dimensions, which has potential applications in various fields, including pressure sensing. Lin et al. combined PMMA with graphene to achieve a sensitivity of 2.87 × $10^{-5}$ $kPa^{-1}$ sensitivity.[228] Liu et al. prepared a pressure sensor with sensitivity of approximately 7.42 × $10^{-5}$ $kPa^{-1}$ .[229] The sensitivity of this device on the unit area is approximately the same order compared with suspended monolayer graphene. Due to the high specific surface area of 2D materials, the resistance of 2D materials is very sensitive to air and humidity. The polymer not only acts as a support for the film, but also isolates the 2D material from the external environment so as to improve the stability of the device.

In addition to mechanical sensitivity, the sensitivity of a device is directly related to the gauge factor of the material. As we mentioned earlier, 2D materials possess a tunable band gap, allowing piezoresistive coefficients to reach exceptionally high levels.[220,221] Wagner et al. (Figure 13e) verified that platinum diselenide ($PtSe_2$) has a GF of −85 ,[230] using 157 $\mu m^2$ suspended membrane with a sensitivity of up to 1.39 × $10^{-3}$ $kPa^{-1}$ (Figure 13f).

### 4.2. Displacement-Based Pressure Sensors

Displacement-based pressure sensors exhibit high environmental robustness and have a wide range of potential applications, including but not limited to automotive, aerospace, and blood pressure monitoring. Displacement-based pressure sensors can be broadly categorized into two primary categories based on their sensing mechanisms: optical fiber pressure sensors and capacitive pressure sensors. Optical fiber pressure sensors measure the displacement at the center point of the diaphragm (Figure 12b), while capacitive pressure sensors detect the deflection of the entire diaphragm caused by the applied pressure (Figure 12c).

#### 4.2.1. Optical Fiber Pressure Sensor

Typically, in order to obtain a larger displacement at the center point of the film, fiber optic pressure sensors usually employ a suspension membrane characterized by a circular geometry. The relationship between the center deflection of a circular suspension membrane and the pressure difference has already been described by Equation (29). In the linear range, dominated by the first term on the right side of equation, the mechanical sensitivity of the fiber optic pressure sensor is proportional to the diameter to thickness ratio and inversely proportional to the prestress in the film. In order to obtain higher sensitivity in fiber optic sensors, many studies have prepared suspension films with larger diameter to thickness ratio using 2D materials (**Table 2**).[231]

2D materials exhibit superior mechanical and atomic-thin layer thickness properties, particularly the ability to fabricate devices with high diameter to thickness ratios, which is challenging in traditional bulk materials. This makes them ideal candidates for use in optical fiber pressure sensors and FOM diaphragms. In 2012, Ma et al. constructed a pressure sensor using a few-layer graphene diaphragm with a width of 25 μm (**Figure 14**a).[232] The diaphragm proved to be effective in accurately detecting fluctuations in air pressure, exhibiting a high sensitivity of over 39.4 nm $kPa^{-1}$ (Figure 14b). Then in 2013, they built one of the earliest FOM utilizing around 100 nm thick multilayer graphene film with 125 μm diameter,[233] indicating a high sensitivity of 1100 nm $kPa^{-1}$, with an equivalent noise background of only 60 $\mu Pa\ Hz^{-1/2}$. This was an exciting value compared with other types of microphones at that time. In 2015, Li et al. conducted a study wherein they modified the length of the FP cavity to 98 μm and fabricated a suspended graphene film with a thickness of 4.36 nm and a diameter of 125 μm.[234] The device achieved an impressive sensitivity of 2.38 nm $Pa^{-1}$ and demonstrated a flat response within the whole audio frequency. Optimization of devices' structures is also a good way for performance improvement. Liao et al. fabricated graphene film with enhanced sensitivity based on the principles of differential Bragg reflector/distributed feedback Bragg (DBR/DFB) fiber laser.[235] Li et al. used the elastic theory of vibrating film to simulate how various mechanical parameters influence the diaphragm's response. They predicted that the higher reflectivity, lower thickness, smaller Young's modulus and larger diaphragm diameter are conducive to higher detection sensitivity and better signal-to-noise ratio of devices.[236] In 2017, Yu et al. developed a fiber optic pressure sensor utilizing a suspended $MoS_2$ diaphragm with a thickness of 8 nm on a 125 μm diameter cavity (Figure 14c).[237] The sensor exhibited a remarkable sensitivity of 89.3 nm $Pa^{-1}$ in the 0–100 Pa range (Figure 14d).

However, the reflectivity of graphene is too low, resulting in a low signal-to-noise ratio of the FP cavity. Wu et al. utilized GO and prepared an 100 nm thick suspended diaphragm with a 1.8 mm diameter to form an FP cavity.[54] Experiments show that GO film has a flatter acoustic response compared with graphene, with the detection signal-to-noise ratio enhanced to 62.2 dB. Dong et al. further explore the role of the diaphragm's reflectivity.[238] They synthesized a 4-layer graphene film composited with 5 nm silver film, enhancing the maximum reflectivity of the diaphragm for more than 5 dB, the result shows the sensitivity of FOM increased by 3 times compared with the film's original electric sensitivity. Better results can be achieved by modulating the air gaps


© 2023 Wiley-VCH GmbH

16163028, 0, Downloaded from https://onlinelibrary.wiley.com/doi/10.1002/adfm.202303519 by Peking University Health, Wiley Online Library on [07/10/2023]. See the Terms and Conditions (https://onlinelibrary.wiley.com/terms-and-conditions) on Wiley Online Library for rules of use; OA articles are governed by the applicable Creative Commons License

**Table 2.** Sensitivity comparison of different optical fiber pressure sensors.

| Author | Year | Material | Suspended area[a] [μm$^2$] | Test range [Pa] | Sensitivity [nm Pa$^{-1}$] | Sensitivity per unit area[b] [nm Pa$^{-1}$μm$^{-2}$] |
|---|---|---|---|---|---|---|
| Ma et al.[232] | 2012 | Graphene | 490 | 0–2 × 10$^4$ | 0.0394 | 8.03 × 10$^{-5}$ |
| Ma et al.[233] | 2013 | Graphene | 11265 | 0–0.4 | 1.1 | 8.97 × 10$^{-5}$ |
| Li et al.[234] | 2015 | Graphene | 12265 | 0–9 | 2.38 | 1.94 × 10$^{-4}$ |
| Yu et al.[237] | 2017 | $MoS_2$ | 12265 | 0–100 | 89.3 | 7.28 × 10$^{-3}$ |
| Xu et al.[231] | 2014 | Silver | 4521600 | 0–7 × 10$^{-3}$ | 160 | 3.54 × 10$^{-5}$ |

[a] the area of the suspended membrane. [b] Sensitivity per unit area = sensitivity/suspended area.

within FP cavity as well. Monteiro et al. utilized a method of solution self-assembly method to fabricate GO films on optic fiber tips.[239] In a 4 mg mL$^{-1}$ GO aqueous dispersion, a diaphragm with a thickness of about 40 nm and radius of about 75 μm was directly deposited on the optical fiber section through vdW interaction (Figure 14e), without the usage of the hazard chemical transfer process. The experiment shows a flat frequency response with a maximum signal to noise ratio of 32.7 dB (Figure 14f). Large stability and sensitivity are remained by FOM of up to 90 degrees Celsius. In the future, further improving the mechanical properties of diaphragm materials and analyzing their performance in extreme environments deserves more efforts to explore.

#### 4.2.2. Capacitive Pressure Sensors

An alternative technique for determining the displacement of membranes is to measure capacitance, which has low energy consumption and high pressure sensitivity. The basic operating principle of a capacitive pressure sensor is illustrated in Figure 12c. The capacitance of the sensor can be determined by the equation:

$$C = \frac{\epsilon A}{d} \tag{33}$$

where $\epsilon$ denotes the absolute dielectric constant of the medium, $A$ represents the area of the pole plates, and $d$ is the distance between the plates. When the pressure differential causes the

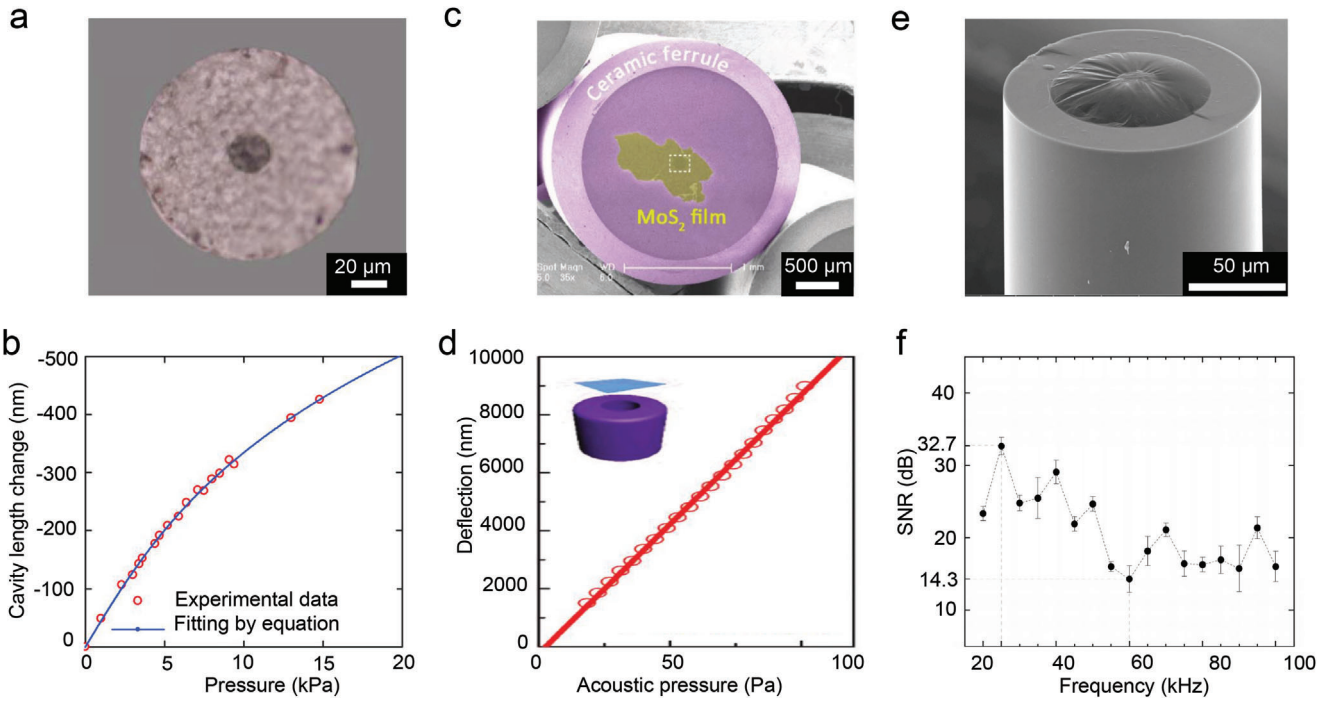


**Figure 14.** Optical fiber pressure sensor. a) Optical images of CVD graphene suspended on a pure silica capillary with an inner diameter of 25 μm. Reproduced with permission.[232] Copyright 2012, Optical Society of America. b) The sensitivity of the suspended graphene bilayers in a) reaches 36 nm kPa$^{-1}$. Reproduced with permission.[232] Copyright 2012, Optical Society of America. c) Low-magnification SEM image of a ceramic ferrule with a diameter of 125 μm covered with a $MoS_2$ film of approximately 8 nm thickness. Reproduced with permission.[237] Copyright 2017, Wiley-VCH. d) Pressure sensors with sensitivity up to 89.3 nm Pa$^{-1}$ prepared from approximately 8 nm thick self-supported $MoS_2$ films in c). Reproduced with permission.[237] Copyright 2017, Wiley-VCH. e) SEM image of the suspended GO film with a thickness about 40 nm. Reproduced with permission.[239] Copyright 2021, MDPI. f) Signal-to-noise ratio of the suspended 40 nm thick GO film at different input acoustic frequencies, with a maximum of 32.7 dB when the frequency is 25 kHz. Reproduced with permission.[239] Copyright 2021, MDPI.


© 2023 Wiley-VCH GmbH

16163028, 0, Downloaded from https://onlinelibrary.wiley.com/doi/10.1002/adfm.202303519 by Peking University Health, Wiley Online Library on [07/10/2023]. See the Terms and Conditions (https://onlinelibrary.wiley.com/terms-and-conditions) on Wiley Online Library for rules of use; OA articles are governed by the applicable Creative Commons License

**Table 3.** Sensitivity comparison of different capacitive pressure sensors (N/A: specific parameter that is not provided by the authors).

| Author | Year | Material | Suspended area[a)] [μm$^2$] | Test range [kPa] | Sensitivity [aF Pa$^{-1}$] | Sensitivity per unit area[b)] [aF Pa$^{-1}$μm$^{-2}$] |
|---|---|---|---|---|---|---|
| Berger et al.[244] | 2017 | PMMA/graphene | N/A | 0–100 | 4.2 | $1.23 \times 10^{-4}$ |
| Berger et al.[245] | 2018 | Polymer/graphene | 196 000 000 | 0.5–8.5 | 27100 | $1.38 \times 10^{-4}$ |
| Šiškins et al.[243] | 2020 | Graphene | 196 250 | 80–120 | N/A | $4.78 \times 10^{-5}$ |
| Tran et al.[242] | 2017 | Graphene | 502 400 | $1–5 \times 10^{-3}$ | 410 000 | $8.16 \times 10^{-1}$ |
| Han et al.[240] | 2009 | Polyamide /metal | 288 000 000 | 0–35 | 30 000 | $1.04 \times 10^{-4}$ |

[a)] The area of the suspended membrane; [b)] Sensitivity per unit area = sensitivity/suspended area.

suspended membrane to deform, altering the distance $d$ between the pole plates, the change in ambient pressure ($\Delta P$) can be detected by measuring the shift in capacitance between the suspended material and the fixed electrode.

The high sensitivity of capacitive pressure sensors requires a larger average displacement ($\bar{w}$) across the film. The average displacement of the entire suspended membrane can be approximated as follows

$$\bar{w} = \frac{w}{2} \tag{34}$$

where $w$ is the displacement of the center point of the film. To obtain higher sensitivity, capacitive pressure sensors are also usually employ a suspension membrane characterized by a circular geometry.

Throughout deformation, the relative area ($A$) of the electrodes remains constant, and as a result, the equation for the change in value of capacitance versus deflection can be simplified to

$$\Delta C = \frac{\varepsilon A}{d_0} - \frac{\varepsilon A}{d_0 - \frac{w}{2}} = \frac{-w\varepsilon A}{d_0(2d_0 - w)} \tag{35}$$

where $d_0$ denotes the initial distance between the film and the electrode. Increasing the diameter to thickness ratio of the suspended membrane, or decreasing the initial spacing between the pole plates can significantly enhance the capacitive sensitivity of the device. The use of suspended 2D materials confers unique advantages in fabricating capacitive pressure sensors with heightened sensitivity (**Table 3**).[240]

The sensitivity of capacitive pressure sensors is closely related to the area of the suspended membrane. To enlarge this area, Chen et al. employed a combination of a gradual solvent replacing technique and a hydrogen bubbling transfer approach with thermal annealing to manufacture a suspended graphene (five layers) pressure sensor with a diameter of 1.5 mm (**Figure 15**a).[176] The device achieved a capacitive sensitivity of up to 15.15 aF Pa$^{-1}$ (Figure 15b). In 2017, Davidovikj et al. fabricated a patterned bottom electrode on an insulating substrate to optimize the contribution of the suspended graphene film to the overall device capacitance,[241] enabling capacitance readout for a single layer suspended graphene film with a diameter of 5 μm. Using an array of suspended graphene films with a diameter of 8 μm and a thickness of 2 nm, Tran et al. achieved a capacitive sensitivity of 164 aF Pa$^{-1}$ over a low-pressure range of 1–5 Pa.[242] In 2020, Šiškins et al. developed pressure sensors using an array of nearly 10000 bilayer graphene membranes,[243] each having a diameter of 5 μm (Figure 15c), achieving a capacitive sensitivity per unit area of up to 47.8 aF Pa$^{-1}$ mm$^{-2}$ (Figure 15d).

Reducing the distance between the polar plates is another effective method of improving capacitance sensitivity, as demonstrated by Equation (35). Berger et al. achieved a suspended film on a 50 nm air medium by combining a single layer of graphene with a 140 nm polymer[244] (Figure 15e) and the device shown was able to achieve a sensitivity of 123 aF Pa$^{-1}$ mm$^{-2}$ from 0 to 100 kPa (Figure 15f). To further enhance sensitivity, the researchers incorporated a 12.5 μm polymer in combination with graphene,[245] resulting in a pressure sensor capable of detecting sensitivity of up to 27.1 fF Pa$^{-1}$ within the 0.5 to 8.5 kPa range.

The ultrathin nature of 2D materials offers unique advantages in the development of highly sensitive pressure sensors. Compared to traditional materials, 2D material pressure sensors exhibit higher sensitivity per unit area in piezoresistive, capacitive, and optical fiber pressure sensors, making them particularly appealing for producing small-sized pressure sensors with higher sensitivity (Tables 1–3).

However, the current transfer process for producing suspended 2D materials and their composites on closed cavities remains to be improved, and achieving thin-thickness films with large suspended areas remains challenging. The conflicting relationship between high sensitivity and wide linear measurement range of pressure sensors is also an unsolved challenge, and modulating the prestress of suspended membrane is a feasible solution. The current piezoresistive pressure sensors prepared from suspended 2D materials and their composites are much more sensitive per unit area than conventional materials, but the overall sensitivity is not as good as conventional piezoresistive materials with large dimensions, and the development of materials with higher GF is expected to solve this shortcoming. In addition, the high specific surface area of 2D materials in piezoresistive pressure sensors makes them more vulnerable to temperature, humidity, gases, etc. Reducing the environmental impact on piezoresistive materials by compounding other materials to isolate them is an effective means of broadening the operating range of piezoresistive pressure sensors. The capacitive pressure sensors also presents a challenging problem primarily due to the high parasitic capacitance. While increasing the suspended area of the thin film and reducing the electrode spacing can enhance capacitance sensitivity, it increases the parasitic capacitance of the device at the same time. Patterning the electrodes to match the suspended membrane or increasing the ratio of the suspended


© 2023 Wiley-VCH GmbH

16163028, 0, Downloaded from https://onlinelibrary.wiley.com/doi/10.1002/adfm.202303519 by Peking University Health, Wiley Online Library on [07/10/2023]. See the Terms and Conditions (https://onlinelibrary.wiley.com/terms-and-conditions) on Wiley Online Library for rules of use; OA articles are governed by the applicable Creative Commons License

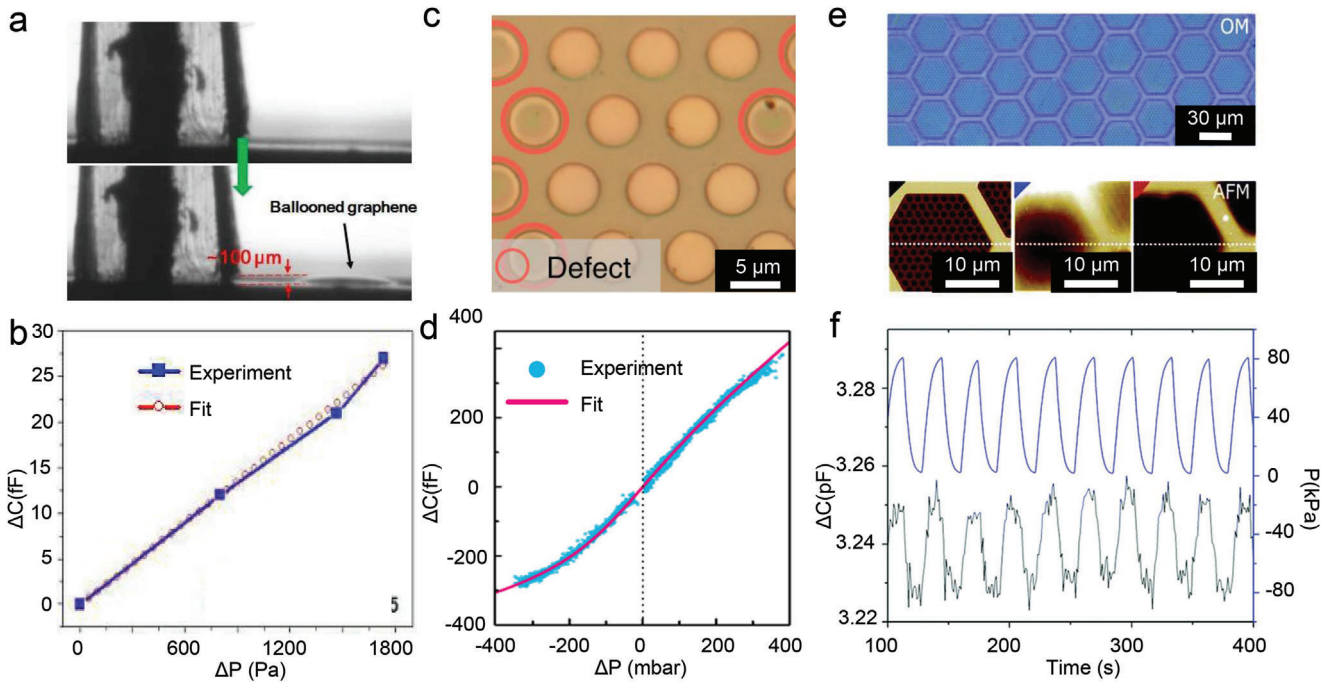


**Figure 15.** Capacitive pressure sensor. a) Optical image shows a CVD graphene film with a diameter of 1.5 mm in suspension, deformed by air pressure by approximately 100 μm. Reproduced with permission.[176] Copyright 2016, Royal Society of Chemistry. b) Capacitive response to air pressure corresponding to the device in Figure a), with a sensitivity of up to 15.15 aF $Pa^{-1}$. Reproduced with permission.[176] Copyright 2016, Royal Society of Chemistry. c) Optical image of CVD bilayer graphene suspended on an array of circular holes with a diameter of 5 μm. Reproduced with permission.[243] Copyright 2020, Springer Nature. d) Barometric capacitance response corresponding to the device in c) with a sensitivity per unit area of up to 47.8 aF $Pa^{-1}$ $mm^{-2}$. Reproduced with permission.[243] Copyright 2020, Springer Nature. e) Optical image and AFM height image of PMMA-assisted graphene suspended on a 30 μm diameter hexagonal array. Reproduced with permission.[244] Copyright 2017, Royal Society of Chemistry. f) The sensitivity per unit area of the device in e) up to 123 aF $Pa^{-1}$ $mm^{-2}$ over a pressure range of 0 to 100 kPa. Reproduced with permission.[244] Copyright 2017, Royal Society of Chemistry.

area of the film to the whole membrane provide good ideas for solutions. As for optical fiber pressure sensors, drawbacks including low signal-to-noise ratio and narrow measurement range, must also be taken into account. The former can be improved by using a higher reflectivity suspended membrane, and the latter is also expected to be solved by suspending a larger size, reducing the thickness of the membrane, and regulating the prestress of the membrane. All of these undoubtedly require advanced material preparation and transfer method as technical support.

## 5. Ultrasonic Frequency Acoustic Devices

As discussed in Section 3 of this review, it is possible to tune the resonant frequency of acoustic diaphragms to the ultrasonic frequency range by adjusting the internal stress and the diameter to thickness ratio of 2D materials. Acoustic diaphragms working in the ultrasonic frequency range not only could be used for ultrasonic imaging or echolocation, but become ideal candidates for sensing.[169,246] Due to the characteristics of low mass, high sensitivity and large frequency tuning range, 2D material resonators can be used in the fields of micro-mass sensing,[247,248] micro-force sensing,[249,250] temperature sensing,[251–254] radiation sensing[255,256] and so on. Utilizing these resonant properties of membranes, specific applications such as light mass and ambient temperature detection can be specially developed with dramatically increased sensitivities, which we will discuss about in more detail.

### 5.1. Mass and Pressure Sensors Based on Suspended 2D Materials Resonators

Suspended diaphragms fabricated from 2D materials have the advantages of ultralight weight which should be highlighted in ultrasensitive micro mass sensing. The mass of gas atoms attached to the membrane can be calculated by monitoring the variance of resonant frequency, which is typically within the ultrasonic frequency range. A study of graphene mass sensor via molecular dynamics simulation (the schematic of this device is shown in **Figure 16**a) found that the resonance frequency of membrane changes from 1.1665 THz to 0.8510 THz with 20 Xe atoms attached on the center (Figure 16b),[248] which could be utilized to realize mass sensing of more than $10^{-6}$ femtograms. This mass sensor can be further utilized for specific recognition of gas molecules. Dolleman et al. analyzed the impurity concentration on the surface of graphene by monitoring the variation of the resonance frequency of graphene diaphragm with respect to oxygen plasma cleaning time,[257] achieving highly sensitive impurity detection. Other calculation results indicate that the mass sensing sensitivity of graphene can be achieved as high as $10^{-27}$ g $Hz^{-1}$,[258] which is able to resolute the


© 2023 Wiley-VCH GmbH

16163028, 0, Downloaded from https://onlinelibrary.wiley.com/doi/10.1002/adfm.202303519 by Peking University Health, Wiley Online Library on [07/10/2023]. See the Terms and Conditions (https://onlinelibrary.wiley.com/terms-and-conditions) on Wiley Online Library for rules of use; OA articles are governed by the applicable Creative Commons License

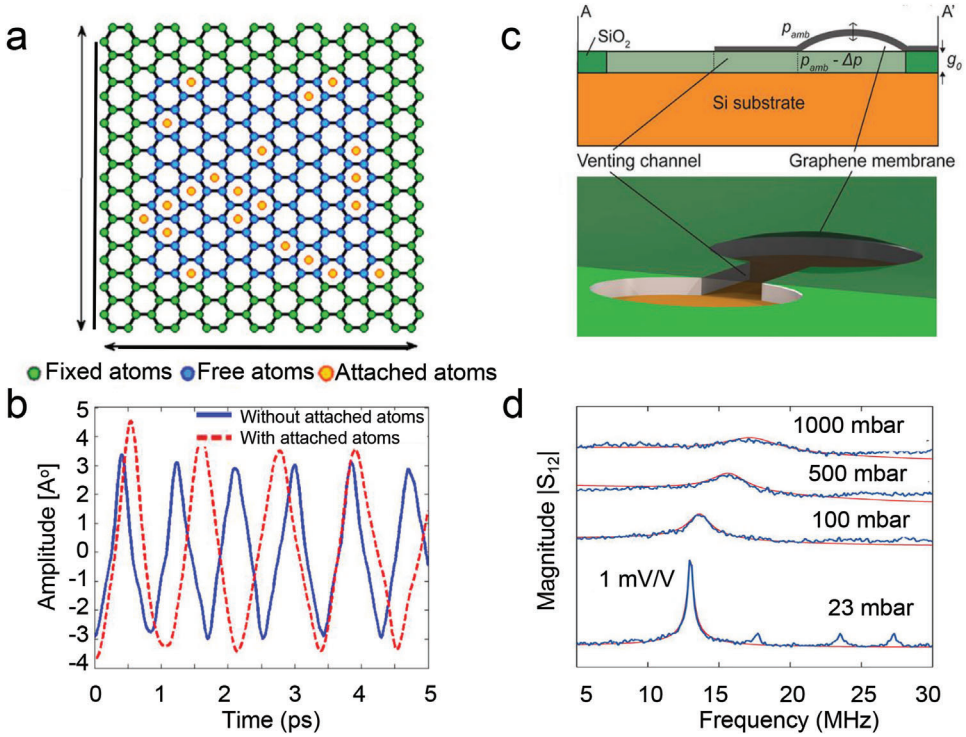


**Figure 16.** Pressure/mass sensors based on 2D material ultrasonic resonator. a) Illustration of different settings of the atoms in the simulation. A model of a fully clamped square graphene resonator of 100 $nm^2$ is built with the honeycomb structure representing the graphene. The green atoms were fixed and the blue atoms are free to vibrate vertically carrying target Xe atom. Reproduced with permission.[248] Copyright 2011, Elsevier B.V. b) Period change when mass varies. Reproduced with permission.[248] Copyright 2011, Elsevier B.V. c) Structure of the pressure sensor based on unsealed resonator. Reproduced with permission.[267] Copyright 2016, American Chemical Society. d) Frequency shift of the unsealed pressure sensor at different atmospheric pressure. Reproduced with permission.[267] Copyright 2016, American Chemical Society.

attachment of only one hydrogen atom with $10^{-4}$ relative shift of resonant peak.[29] Compared to other traditional materials based mass sensors, graphene mass sensor has obvious advantages.[259] These measurements of resonant frequency due to attached light mass can be combined with the optical and electrical measurement methods demonstrated in Section 3 so as to further enhance the measuring efficiency. Other theoretical calculations of 2D material based mass sensors have studied the influence of temperature,[260] in-plane magnetic field,[261] layer numbers,[262] internal stress,[263] diameter to thickness ratio[264] and higher order nonlinear vibration modes.[265] The results of these theoretical calculations provide feasible suggestions for future experiments with enhanced sensitivity and reliability of mass sensors.

As for pressure sensors working in the ultrasonic frequency range, unlike the static pressure sensors discussed in Section 4, the film is squeezed and the stress changes because of the air pressure difference between two sides, which directly causes the shift of resonant frequency. Lee and Feng used bilayer and trilayer $MoS_2$ on high-frequency circular drumhead resonator and found that the resonator exhibited ultrasmall footprints, minimal air damping and high pressure responsivity, revealing the great potential for pressure sensing in a wide pressure range.[266] In 2015, Dolleman et al. transferred the few-layer graphene on a dumbbell shaped hole, forming an unconventional pressure sensor with venting channel (Figure 16c).[267] The unsealed structure maintains the average pressure inside and outside the resonator. When operating at a high frequency, the gas inside is trapped in its effective position because of the viscous force, and the resonance frequency shift obviously when the pressure varies from 23 mbar to 1000 mbar (Figure 16d).

### 5.2. Thermal Sensors Based on Suspended 2D Materials

As temperature raises, the resonant frequency also changes due to the variation of Young's modulus, internal stress, volume and many other factors. The correspondence between resonant frequency and temperature is potential to be utilized as thermal sensors. Yang et al. successfully made a thermal sensor based on $MoS_2$ mechanical resonator (as shown in **Figure 17**a).[268] By changing the temperature with small steps and monitoring the resonant frequency variations, they calibrated the temperature coefficient of frequency (TCF, defined as the ratio of frequency change to resonant frequency, with value $\frac{|f_0-f_0'|}{f_0}$ or $\frac{\Delta f}{f_0}$) and thermal expansion coefficient of this $MoS_2$ mechanical resonator. It shows a negative TCF with an estimated value of −0.396% $K^{-1}$ from 293 to 315.5 K (Figure 17b). The quality factor also decreases with temperature (determined by power of laser). Similar work is conducted in graphene based mechanical resonators by Ye et al.[254] It is shown that graphene diaphragm possesses an extraordinary negative thermal expansion coefficient. As the temperature goes up, the diaphragm will shrink, which is


© 2023 Wiley-VCH GmbH

16163028, 0, Downloaded from https://onlinelibrary.wiley.com/doi/10.1002/adfm.202303519 by Peking University Health, Wiley Online Library on [07/10/2023]. See the Terms and Conditions (https://onlinelibrary.wiley.com/terms-and-conditions) on Wiley Online Library for rules of use; OA articles are governed by the applicable Creative Commons License

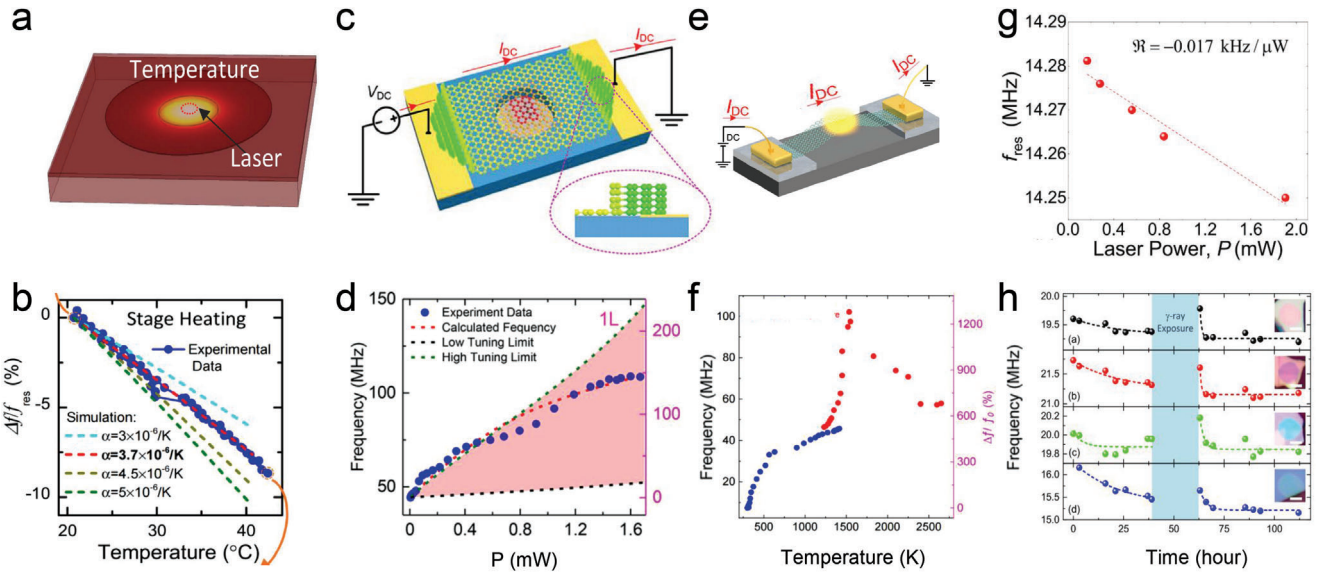


**Figure 17.** Thermal/radiation sensors based on 2D material ultrasonic resonator. a) Schematic about suspended $MoS_2$ thermal sensor with laser heating to determine the device temperature. Reproduced with permission.[268] Copyright 2015, IEEE. b) Temperature-frequency curve in experiment and simulations, as shown in the figure they show good correspondence. Reproduced with permission.[268] Copyright 2015, IEEE. c) Illustration of the working principle of the fully clamped graphene resonator. Reproduced with permission.[254] Copyright 2018, American Chemical Society. d) Experimental data and calculated resonance frequency with different temperatures indicated by different laser power. Reproduced with permission.[254] Copyright 2018, American Chemical Society. e) Illustration of the working principle of the double clamped graphene resonator at high temperature. Reproduced with permission.[269] Copyright 2018, IEEE. f) Anomalous temperature-frequency correspondence of graphene resonator at high temperature. Thermal sensor has a limited operating range given that thermal expansion coefficients beyond a certain temperature becomes positive, which causes the resonant frequency to reduce. Reproduced with permission.[269] Copyright 2018, IEEE. g) Resonance frequency shift caused by absorption of infrared light of different power. Reproduced with permission.[255] Copyright 2020, IEEE. h) Detection of the $\gamma$-ray at low dose. Reproduced with permission.[270] Copyright 2016, AIP Publishing.

necessary for keeping its resonant peak on stage (no resonant peak exists if the diaphragm enlargers and gets relaxed), making it more stable to realize temperature modulation of the resonant peak., Next, they studied the graphene resonator tuned by periodic Joule heating (shown in Figure 17c, the color of the atoms indicates the temperature gradient with the green and red atoms representing low temperature and high temperature respectively). The test result shows broad band modulation ranges with TCF≈310% at temperature up to 1200 K (Figure 17d). Further upgrading the temperature to 2650K (the highest operating temperature for electromechanical resonators known to date, as shown in Figure 17e), the operation range of frequency modulation indicated by TCF reaches approximately 1300%, as is the widest frequency tuning range up to that time.[269] These works definitely illustrate the strengths of suspended 2D materials to be utilized into thermal sensors. However, this type of thermal sensor has a limited operating range given that thermal expansion coefficients beyond a certain temperature becomes positive which causes the resonant frequency to reduce (as is shown in Figure 17f).

Furthermore, specific temperature sensing within different optical wavelength ranges can be achieved due to the different absorption characteristics of 2D materials. For instance, multilayer black phosphorus has a direct bandgap of 0.3 eV and thus absorbs infrared light up to 4 μm. When exposed to a 785 nm infrared light, the resonant frequency decreases as laser power (indicating temperature) goes up (Figure 17g) with the responsivity about −0.31 kHz $\mu W^{-1}$.[255] Such selective light absorption properties can be highly utilized in infrared ranged thermal sensing. Some other works also illustrate the phonon absorption of the $MoS_2$ which makes it respond to the absorption of $\gamma$-ray with the sensitivity of 30–82 Hz per phonon,[270] comparable with the dosage at the very beginning of the nuclear leakage (Figure 17h).

### 5.3. Other Types of Ultrasonic Transducers Based on Suspended 2D Materials

In addition to static pressure sensors, some pressure sensors operating in the ultrasonic frequency range with unclosed structures are able to achieve wider range and higher sensitivity pressure responses as well as miniaturized sizes.[267,271–273] For example, the micro-machined ultrasonic transducer (MUT) classified as piezoelectric micromachined ultrasonic transducer (PMUT) and capacitive micro-machined ultrasonic transducer (CMUT) have been widely utilized in medical imaging and ultrasound localization.[274,275] PMUT is a sensing array composed of piezoelectric film such as PZT and polymer support layers, which realizes the conversion between mechanical energy and induced charges during deformation.[274,276] The CMUT reads the deformation through the capacitance change between the suspended film and the bottom electrode to obtain acoustic information. Some CMUT diaphragms are also composed of 2D materials and polymers.[244] Due to the ultralight weight and high mechanical strength of 2D material graphene, it can also be composed of


© 2023 Wiley-VCH GmbH

16163028, 0, Downloaded from https://onlinelibrary.wiley.com/doi/10.1002/adfm.202303519 by Peking University Health, Wiley Online Library on [07/10/2023]. See the Terms and Conditions (https://onlinelibrary.wiley.com/terms-and-conditions) on Wiley Online Library for rules of use; OA articles are governed by the applicable Creative Commons License

16163028, 0, Downloaded from https://onlinelibrary.wiley.com/doi/10.1002/adfm.202303519 by Peking University Health, Wiley Online Library on [07/10/2023]. See the Terms and Conditions (https://onlinelibrary.wiley.com/terms-and-conditions) on Wiley Online Library for rules of use; OA articles are governed by the applicable Creative Commons License

CMUT without the polymer support layer.[176,277] The resolution of these detectors would be greatly improved by arraying acoustic devices with micron-scale sizes. Combined with ultrathin 2D materials, the arrayed MEMS-based CMUT shows its potential to be further miniaturized with higher performance, which it is still in the early stage of research.

On the other hand, as for the ultrasonic resonator and sensing application, there is less work using 2D composite materials. It seems that most ultrasonic resonators are micro-sized or nano-sized devices so that the 2D materials are easier to be transferred and suspended compared with large-area suspending materials, thus the polymer support layer is unnecessary. Besides, higher weight of the diaphragm will reduce the sensitivity under some scenarios. Taking mass sensor as an example, according to the working principle, the sensitivity is reflected by the shift of the resonance frequency point, which is determined by the relative change of the mass. Heavier weight will inevitably lead to a substantial reduction in sensitivity.

In summary, ultrasonic frequency acoustic sensors based on suspended 2D materials typically respond to physical quantities such as mass, pressure, and temperature through changes in resonant frequency. These resonators have the ability to detect mass as small as a single hydrogen atom, making them promising for applications such as highly sensitive gas sensing and indoor air pressure navigation. Additionally, the sensitivity of the resonator to temperature has potential applications in monitoring industrial production and processes related to high-precision thermal treatments. By combining the advantages of 2D materials and micromachining technology, further development of highly-integrated ultrasonic transducer arrays made of 2D materials would result in even higher precision and sensitivity for ultrasound detection.

## 6. Conclusion

In this review, we briefly summarize the recent progress of acoustic devices based on suspended 2D materials and their composites, especially applications in the audio frequency, static pressure, and ultrasonic frequency range, comprehensively discussing their preparation methods, working principles and performance optimization methods. 2D materials and their composites have aroused more and more attention, due to their intrinsic outstanding properties including atomic layer thickness, large diameter to thickness ratio, high mechanical strength, extensive surface area, and remarkable layer-stacking tunability, which are conducive to promoting the development of high-performance acoustic devices with controlled size (either large or small), low power consumption, and multifunctional capabilities.

On the one hand, with the development of the wafer-scale 2D materials synthesis methods, as well as the controllable membrane transfer techniques, high quality large area vibrating diaphragm with diameter to thickness ratio exceeding $10^6$ can be achieved, which is almost impossible in traditional bulk materials. Remarkably, through suspension of 2D material membranes, the mechanical and thermal disruption from substrate can be further eliminated. The larger diameter to thickness ratio of suspended 2D material-based diaphragms leads to greatly optimized performance for speakers/microphones and sensors. On the other hand, integrated with the mature MEMS/NEMS techniques, acoustic devices based on 2D materials and their composites have also shown their great potential in future state-of-the-art transducers and sensors, such as highly arrayed nanoscale 2D acoustic sensors with significantly increased bandwidth and sensitivity. All these advancements will definitely pave the way for the high-performance next-generation acoustic devices in the near future.

## Acknowledgements

Z.W., H.L., Y.Z., and Y.M.. contributed equally to this work. This work was supported by Guangdong Major Project of Basic and Applied Basic Research (2021B0301030002), the National Natural Science Foundation of China (12104018, 52025023, 51991342, 52021006, 92163206, 11888101 and T2188101), China Postdoctoral Science Foundation (2022M710232), and the New Cornerstone Science Foundation through the XPLORER PRIZE.

## Conflict of Interest

The authors declare no conflict of interest.

## Keywords

acoustic devices, audio frequency, static pressure, suspended 2D materials, ultrasonic frequency

Received: March 29, 2023
Revised: August 15, 2023
Published online:

[1] F. Brandt, *Semin. Hear.* **1989**, *10*, 31.
[2] P. R. Scheeper, A. G. H. Van Der Donk, W. Olthuis, P. Bergveld, *Sens. Actuators, A* **1994**, *44*, 1.
[3] N. J. C. A. Fletcher, *Can. Acoust.* **2003**, *31*, 35.
[4] X. Fan, J. Chen, J. Yang, P. Bai, Z. Li, Z. L. Wang, *ACS Nano* **2015**, *9*, 4236.
[5] X. H. Guo, J. B. An, H. C. Wu, Z. H. Cai, P. Wang, *Ultrasonics* **2021**, *114*, 106420.
[6] A. Kumar, A. Varghese, A. Sharma, M. Prasad, V. Janyani, R. P. Yadav, K. Elgaid, *Sens. Actuators, A* **2022**, *347*, 113887.
[7] M. A. Shah, I. A. Shah, D.-G. Lee, S. Hur, *J. Sen.* **2019**, *2019*, 9294528.
[8] H. F. Olson, J. Preston, E. G. May, *J Audio Eng. Soc.* **1954**, *2*, 219.
[9] F. Giorgianni, C. Vicario, M. Shalaby, L. D. Tenuzzo, A. Marcelli, T. Zhang, K. Zhao, Y. Chen, C. Hauri, S. Lupi, *Adv. Funct. Mater.* **2018**, *28*, 1702652.
[10] H. Ding, X. Shu, Y. Jin, T. Fan, H. Zhang, *Nanoscale* **2019**, *11*, 5839.
[11] Q. Zhou, A. Zettl, *Appl. Phys. Lett.* **2013**, *102*, 223109.
[12] A. Dehe, G. Ruhl (Infineon Technologies AG), US9516428B2, **2016**.
[13] H. R. Wang, Y. F. Ma, Q. C. Zheng, K. Cao, Y. Lu, H. Xie, *Micromachines* **2021**, *12*, 1257.
[14] I. Shahosseini, E. Lefeuvre, E. Martincic, M. Woytasik, J. Moulin, S. Megherbi, R. Ravaud, G. Lemarquand, *Microsyst. Technol.* **2012**, *18*, 1791.
[15] H. S. Lee, J. Chung, G.-T. Hwang, C. K. Jeong, Y. Jung, J.-H. Kwak, H. Kang, M. Byun, W. D. Kim, S. Hur, S-Ha Oh, K. J. Lee, *Adv. Funct. Mater.* **2014**, *24*, 6914.
[16] P. Cawley, *Struct. Health Monit.* **2018**, *17*, 1225.

 © 2023 Wiley-VCH GmbH

[17] K. G. Foote, in *Oceans-IEEE*, IEEEE, Piscaataway, NJ **2008**, p. 1327, https://doi.org/10.1109/OCEANS.2008.5289427.
[18] H. J. Hu, H. Huang, M. H. Li, X. X. Gao, L. Yin, Q. Ruixiang, R. S. Wu, X. Chen, Y. Ma, K. Shi, C. Li, T. M. Maus, B. Huang, C. Lu, M. Lin, S. Zhou, Z. Lou, Y. Gu, Y. Chen, Y. Lei, X. Wang, R. Wang, W. Yue, X. Yang, Y. Bian, J. Mu, G. Park, S. Xiang, S. Cai, P. W. Corey, et al., *Nature* **2023**, *613*, 667.
[19] Y. Q. Fu, J. K. Luo, N. T. Nguyen, A. J. Walton, A. J. Flewitt, X.-T. Zu, Y. Li, G. McHale, A. Matthews, E. Iborra, H. Du, W. I. Milne, *Prog. Mater. Sci.* **2017**, *89*, 31.
[20] T. Xu, W. Gao, Li-P Xu, X. Zhang, S. Wang, *Adv. Mater.* **2017**, *29*, 1603250.
[21] S. Zhang, F. Li, X. Jiang, J. Kim, J. Luo, X. Geng, *Prog. Mater. Sci.* **2015**, *68*, 1.
[22] J. X. Zhu, X. M. Liu, Q. F. Shi, T. Y. Y. He, Z. D. Sun, X. G. Guo, W. X. Liu, S. O. Bin, B. W. Dong, C. Lee, *Micromachines* **2020**, *11*, 7.
[23] L. Zigoneanu, B.-I. Popa, S. A. Cummer, *Nat. Mater.* **2014**, *13*, 352.
[24] C. Wang, X. Chen, L. Wang, M. Makihata, H.-C. Liu, T. Zhou, X. Zhao, *Science* **2022**, *377*, 517.
[25] B. Tiller, A. Reid, B. Zhu, J. Guerreiro, R. Domingo-Roca, J. Curt Jackson, J. F. C. Windmill, *Mater. Des.* **2019**, *165*, 107593.
[26] Q. Zhou, J. Zheng, S. Onishi, M. F. Crommie, A. K. Zettl, *Proc. Natl. Acad. Sci. USA* **2015**, *112*, 8942.
[27] M. L. Kuntzman, J. L. LoPresti, Y. Du, W. F. Conklin, V. Naderyan, S. B. Lee, D. Schafer, M. Pedersen, P. V. Loeppert, *J. Acoust. Soc. Am.* **2019**, *145*, 327.
[28] A. F. Carvalho, B. Kulyk, A. J. S. Fernandes, E. Fortunato, F. M. Costa, *Adv. Mater.* **2022**, *34*, 2101326.
[29] M. C. Lemme, S. Wagner, K. H. Lee, X. G. Fan, G. J. Verbiest, S. Wittmann, S. Lukas, R. J. Dolleman, F. Niklaus, H. S. J. van der Zant, G. S. Duesberg, P. G. Steeneken, *Research* **2020**, *2020*, 8748602.
[30] J. Wan, S. D. Lacey, J. Dai, W. Bao, M. S. Fuhrer, L. Hu, *Chem. Soc. Rev.* **2016**, *45*, 6742.
[31] H. Zhang, *ACS Nano* **2015**, *9*, 9451.
[32] K.-H. Lee, S. Chakram, S. E. Kim, F. Mujid, A. Ray, H. Gao, C. Park, Yu Zhong, D. A. Muller, D. I. Schuster, J. Park, *Nano Lett.* **2019**, *19*, 8287.
[33] J.-Y. Kim, X. Ju, K.-W. Ang, D. Chi, *ACS Nano* **2023**, *17*, 1831.
[34] J. Zhang, Li Lin, K. Jia, L. Sun, H. Peng, Z. Liu, *Adv. Mater.* **2020**, *32*, 1903266.
[35] T. Y. Liu, C. Liu, K. H. Liu, *Acta Phys. Sin.* **2022**, *71*, 108103.
[36] H-U. Kim, H. Seok, W. S. Kang, T. Kim, *Nanoscale Adv* **2022**, *4*, 2962.
[37] S. Alam, M. A. Chowdhury, A. Shahid, R. Alam, A. Rahim, *FlatChem* **2021**, *30*, 100305.
[38] V. L. Nguyen, B. G. Shin, D. L. Duong, S. T. Kim, D. Perello, Y. J. Lim, Q. H. Yuan, F. Ding, H. Y. Jeong, H. S. Shin, S. M. Lee, S. H. Chae, Q. A. Vu, S. H. Lee, Y. H. Lee, *Adv. Mater.* **2015**, *27*, 1376.
[39] X. Li, C. W. Magnuson, A. Venugopal, R. M. Tromp, J. B. Hannon, E. M. Vogel, L. Colombo, R. S. Ruoff, *J. Am. Chem. Soc.* **2011**, *133*, 2816.
[40] I. V. Vlassiouk, Y. Stehle, P. R. Pudasaini, R. R. Unocic, P. D. Rack, A. P. Baddorf, I. N. Ivanov, N. V. Lavrik, F. List, N. Gupta, K. V. Bets, B. I. Yakobson, S. N. Smirnov, *Nat. Mater.* **2018**, *17*, 318.
[41] X. Z. Xu, Z. H. Zhang, J. C. Dong, D. Yi, J. J. Niu, M. Wu, L. Lin, R. Yin, M. Li, J. Zhou, S. Wang, J. Sun, X. Duan, P. Gao, Y. Jiang, X. Wu, H. Peng, R. S. Ruoff, Z. Liu, D. Yu, E. Wang, F. Ding, K. Liu, *Sci. Bull.* **2017**, *62*, 1074.
[42] T. Iwasaki, H. J. Park, M. Konuma, D. S. Lee, J. H. Smet, U. Starke, *Nano Lett.* **2011**, *11*, 79.
[43] P. W. Sutter, J. I. Flege, E. A. Sutter, *Nat Mater* **2008**, *7*, 406.
[44] A. T. N'Diaye, R. van Gastel, A. J. Martinez-Galera, J. Coraux, H. Hattab, D. Wall, F. J. M. zu Heringdorf, M. Horn-von Hoegen, J. M. Gomez-Rodriguez, B. Poelsema, C. Busse, T. Michely, *New J. Phys.* **2009**, *11*, 113056.
[45] Y. Wu, G. Yu, H. Wang, B. Wang, Z. Chen, Y. Zhang, B. Wang, X. Shi, X. Xie, Z. Jin, X. Liu, *Carbon* **2012**, *50*, 5226.
[46] H. Wang, G. Yu, *Adv. Mater.* **2016**, *28*, 4956.
[47] H., J. Chen, H. Ma, X. Sun, X. Jiang, K. Liu, J. Shan, X. Lian, B. Jiang, R. Liu, B. Liu, G. Yang, W. Yin, W. Zhao, L. Huang, T. Gao, J. Sun, Z. Liu, *Adv. Mater.* **2022**, *34*, 2206389.
[48] Z. L. Chen, Y. Qi, X. D. Chen, Y. F. Zhang, Z. F. Liu, *Adv. Mater.* **2019**, *31*, 1803639.
[49] J.-H. Lee, E. K. Lee, W.-J. Joo, Y. Jang, B.-S. Kim, J. Y. Lim, S.-H. Choi, S. J. Ahn, J. R. Ahn, M-Ho Park, C.-W. Yang, B. L. Choi, S.-W. Hwang, D. Whang, *Science* **2014**, *344*, 286.
[50] H. Yu, M. Liao, W. Zhao, G. Liu, X. J. Zhou, Z. Wei, X. Xu, K. Liu, Z. Hu, Ke Deng, S. Zhou, J-An Shi, L. Gu, C. Shen, T. Zhang, L. Du, Li Xie, J. Zhu, W. Chen, R. Yang, D. Shi, G. Zhang, *ACS Nano* **2017**, *11*, 12001.
[51] T. Li, W. Guo, L. Ma, W. Li, Z. Yu, Z. Han, Si Gao, L. Liu, D. Fan, Z. Wang, Y. Yang, W. Lin, Z. Luo, X. Chen, N. Dai, X. Tu, D. Pan, Y. Yao, P. Wang, Y. Nie, J. Wang, Yi Shi, X. Wang, *Nat. Nanotechnol.* **2021**, *16*, 1201.
[52] J. Wang, X. Xu, T. Cheng, L. Gu, R. Qiao, Z. Liang, D. Ding, H. Hong, P. Zheng, Z. Zhang, Z. Zhang, S. Zhang, G. Cui, C. Chang, C. Huang, J. Qi, J. Liang, C. Liu, Y. Zuo, G. Xue, X. Fang, J. Tian, M. Wu, Yi Guo, Z. Yao, Q. Jiao, L. Liu, P. Gao, Q. Li, R. Yang, *Nat. Nanotechnol.* **2022**, *17*, 33.
[53] M. A. Alibakhshi, X. Kang, D. Clymer, Z. Zhang, A. Vargas, V. Meunier, M. Wanunu, *Adv. Mater.* **2023**, 2207089.
[54] Yu Wu, C. Yu, F. Wu, C. Li, J. Zhou, Y. Gong, Y. Rao, Y. Chen, *J. Lightwave Technol.* **2017**, *35*, 4344.
[55] W. S. Hummers, R. E. Offeman, *J. Am. Chem. Soc.* **1958**, *80*, 1339.
[56] R. Cruz-Silva, M. Endo, M. Terrones, *Nanotechnol. Rev.* **2016**, *5*, 377.
[57] P. Li, Y. Han, M. H. Wang, X. X. Cao, J. F. Gao, Y. Liu, X. Chen, B. Wang, B. Wang, C. Zhu, X. Wang, K. Cao, M. Huang, B. V. Cunning, J. Pang, W. Xu, Y. Ying, Z. Xu, W. Fang, Y. Lu, R. S. Ruoff, C. Gao, *Adv. Mater.* **2021**, *33*, 2104195.
[58] R. K. Singh, R. Kumar, D. P. Singh, *RSC Adv.* **2016**, *6*, 64993.
[59] M. S. Stark, K. L. Kuntz, S. J. Martens, S. C. Warren, *Adv. Mater.* **2019**, *31*, 1808213.
[60] A. M. Abdelkader, A. J. Cooper, R. A. W. Dryfe, I. A. Kinloch, *Nanoscale* **2015**, *7*, 6944.
[61] Z. Y. Lin, Y. Liu, U. Halim, M. N. Ding, Y. Y. Liu, Y. Wang, C. Jia, P. Chen, X. Duan, C. Wang, F. Song, M. Li, C. Wan, Y. Huang, X. Duan, *Nature* **2018**, *562*, 254.
[62] J. D. Caldwell, T. J. Anderson, J. C. Culbertson, G. G. Jernigan, K. D. Hobart, F. J. Kub, M. J. Tadjer, J. L. Tedesco, J. K. Hite, M. A. Mastro, R. L. Myers-Ward, C. R. Eddy, P. M. Campbell, D. K Gaskill, *ACS Nano* **2010**, *4*, 1108.
[63] S. Ullah, X. Q. Yang, H. Q. Ta, M. Hasan, A. Bachmatiuk, K. Tokarska, B. Trzebicka, L. Fu, M. H. Rummeli, *Nano Res.* **2021**, *14*, 3756.
[64] A. Castellanos-Gomez, M. Buscema, R. Molenaar, V. Singh, L. Janssen, H. S. J. van der Zant, G. A. Steele, *2D Mater.* **2014**, *1*, 011002.
[65] J. H. Kim, T.-J. Ko, E. Okogbue, S. S. Han, M. S. Shawkat, M. G. Kaium, K. H. Oh, H.-S. Chung, Y. Jung, *Stem Cells Int.* **2019**, *9*, 1641.
[66] A. J. Watson, W. B. Lu, M. H. D. Guimaraes, M. Stohr, *2D Mater.* **2021**, *8*, 032001.
[67] J. Cai, H. Chen, Y. Ke, S. Deng, *ACS Nano* **2022**, *16*, 15016.
[68] T. Hallam, C. F. Moldovan, K. Gajewski, A. M. Ionescu, G. S. Duesberg, *Phys. Status Solidi B* **2015**, *252*, 2429.
[69] W. Regan, N. Alem, B. Alemán, B. Geng, Ç. Girit, L. Maserati, F. Wang, M. Crommie, A. Zettl, *Appl. Phys. Lett.* **2010**, *96*, 113102.
[70] A. M. V. D Zande, R. A. Barton, J. S. Alden, C. S. Ruiz-Vargas, W. S. Whitney, P. H. Q. Pham, J. Park, J. M. Parpia, H. G. Craighead, P. L. Mceuen, *Nano Lett.* **2010**, *10*, 4869.

 © 2023 Wiley-VCH GmbH

16163028, 0, Downloaded from https://onlinelibrary.wiley.com/doi/10.1002/adfm.202303519 by Peking University Health, Wiley Online Library on [07/10/2023]. See the Terms and Conditions (https://onlinelibrary.wiley.com/terms-and-conditions) on Wiley Online Library for rules of use; OA articles are governed by the applicable Creative Commons License

[71] R. Frisenda, E. Navarro-Moratalla, P. Gant, D. Pérez De Lara, P. Jarillo-Herrero, R. V. Gorbachev, A. Castellanos-Gomez, *Chem. Soc. Rev.* **2018**, *47*, 53.
[72] Q. Wang, Y. Liu, F. S. Xu, X. D. Zheng, G. S. Wang, Y. Zhang, J. Qiu, G. J. Liu, *Micromachines* **2021**, *12*, 525.
[73] S. A. Akbari, V. Ghafarinia, T. Larsen, M. M. Parmar, L. G. Villanueva, *Stem Cells Int.* **2020**, *10*, 6426.
[74] A. F. Carvalho, A. J. S. Fernandes, M. Ben Hassine, P. Ferreira, E. Fortunato, F. M. Costa, *Appl. Mater. Today* **2020**, *21*, 100879.
[75] Ki-B Nam, Q. Hu, J-Ho Yeo, M. J. Kim, Ji-B Yoo, *Nanoscale Adv* **2022**, *4*, 3824.
[76] J. Zhu, X. Liu, Q. Shi, T. He, Z. Sun, X. Guo, W. Liu, O. Bin Sulaiman, B. Dong, C. Lee, *Micromachines* **2019**, *11*, 7.
[77] M. AbdelGhany, F. Mahvash, M. Mukhopadhyay, A. Favron, R. Martel, M. Siaj, T. Szkopek, *2D Mater.* **2016**, *3*, 041005.
[78] B. Alemán, W. Regan, S. Aloni, V. Altoe, N. Alem, C. Girit, B. Geng, L. Maserati, M. Crommie, F. Wang, A. Zettl, *ACS Nano* **2010**, *4*, 4762.
[79] Y. Song, W. Zou, Qi Lu, Li Lin, Z. Liu, *Small* **2021**, *17*, 2007600.
[80] L. Zheng, Y. Chen, N. Li, J. Zhang, N. Liu, J. Liu, W. Dang, B. Deng, Y. Li, X. Gao, C. Tan, Zi Yang, S. Xu, M. Wang, H. Yang, L. Sun, Yi Cui, X. Wei, P. Gao, H.-W. Wang, H. Peng, *Nat. Commun.* **2020**, *11*, 541.
[81] S. S. Verbridge, D. F. Shapiro, H. G. Craighead, J. M. Parpia, *Nano Lett.* **2007**, *7*, 1728.
[82] W.-M. Zhang, K.-M. Hu, Z-Ke Peng, G. Meng, *Sensors* **2015**, *15*, 26478.
[83] L. Yang, Y. Huang, K. Liu, Z. Wu, Q. Zhou, *J. Phys. Chem. C* **2022**, *126*, 10449.
[84] C. Galiotis, O. Frank, E. N. Koukaras, D. Sfyris, *Annu. Rev. Chem. Biomol. Eng.* **2015**, *6*, 121.
[85] C. Lee, X. Wei, J. W. Kysar, J. Hone, *Science* **2008**, *321*, 385.
[86] I. R. Storch, R. De Alba, V. P. Adiga, T. S. Abhilash, R. A. Barton, H. G. Craighead, J. M. Parpia, P. L. McEuen, *Phys. Rev. B* **2018**, *98*, 085408.
[87] B. Chitara, A. Ya'akobovitz, *Nanoscale* **2018**, *10*, 13022.
[88] A. K. Al-Mashaal, G. S. Wood, A. Torin, E. Mastropaolo, M. J. Newton, R. Cheung, *Appl. Phys. Lett.* **2017**, *111*, 243503.
[89] H. Hartmann, J.-N. Beyer, J. Hansen, S. C. Bittinger, M. Yesilmen, H. Schlicke, T. Vossmeyer, *ACS Appl. Mater. Interfaces* **2021**, *13*, 40932.
[90] R. De Alba, T. S. Abhilash, A. Hui, I. R. Storch, H. G. Craighead, J. M. Parpia, *J. Appl. Phys.* **2018**, *123*, 095109.
[91] L. Zheng, N. Liu, X. Gao, W. Zhu, K. Liu, C. Wu, R. Yan, J. Zhang, X. Gao, Y. Yao, B. Deng, J. Xu, Ye Lu, Z. Liu, M. Li, X. Wei, H.-W. Wang, H. Peng, *Nat. Methods* **2023**, *20*, 123.
[92] J. Zabel, R. R. Nair, A. Ott, T. Georgiou, A. K. Geim, K. S. Novoselov, C. Casiraghi, *Nano Lett.* **2012**, *12*, 617.
[93] B. Karki, B. Freelon, M. Rajapakse, R. Musa, S. M. S. Riyadh, B. Morris, U. Abu, M. Yu, G. Sumanasekera, J. B. Jasinski, *Nanotechnology* **2020**, *31*, 425707.
[94] E. Del Corro, M. Taravillo, V. G. Baonza, *Phys. Rev. B* **2012**, *85*, 033407.
[95] J. C. McDonald, G. M. Whitesides, *Acc. Chem. Res.* **2002**, *35*, 491.
[96] H. H. Kim, S. K. Lee, S. G. Lee, E. Lee, K. Cho, *Adv. Funct. Mater.* **2016**, *26*, 2070.
[97] C. Y. Chen, S. Lee, V. V. Deshpande, G. H. Lee, M. Lekas, K. Shepard, J. Hone, *Nat. Nanotechnol.* **2013**, *8*, 923.
[98] N. Morell, A. Reserbat-Plantey, I. Tsioutsios, K. G. Schädler, F. Dubin, F. H. L. Koppens, A. Bachtold, *Nano Lett.* **2016**, *16*, 5102.
[99] D. Davidovikj, M. Poot, S. J. Cartamil-Bueno, H. S. J. Van Der Zant, P. G. Steeneken, *Nano Lett.* **2018**, *18*, 2852.
[100] B. L. Turner, S. Senevirathne, K. Kilgour, D. Mcart, M. Biggs, S. Menegatti, M. A. Daniele, *Adv. Healthcare Mater.* **2021**, *10*, 2100986.
[101] L. Wang, X. M. Fu, J. Q. He, X. Shi, T. Q. Chen, P. Chen, B. Wang, H. Peng, *Adv. Mater.* **2020**, *32*, 1901971.
[102] Li Gao, *Small* **2017**, *13*, 1603994.
[103] J. H. Kim, J. H. Jeong, N. Kim, R. Joshi, G.-H. Lee, *J. Phys. D: Appl. Phys.* **2019**, *52*, 083001.
[104] R. Lerch, M. Kaltenbacher, M. Meiler, *J. Acoust. Soc. Am.* **2008**, *123*, 3643.
[105] T. Dumon, O. Zennaro, J.-M. Aran, J.-P. Bebear, *Otolaryngol. Clin. North Am.* **1995**, *28*, 173.
[106] H.-Y. Chiang, Yu-H Huang, *J. Acoust. Soc. Am.* **2015**, *137*, 1714.
[107] J. G. Švec, S. Granqvist, *J. Speech Hear. Res.* **2018**, *61*, 441.
[108] S. E. Tranter, D. A. Reynolds, *IEEE Trans. Audio Speech Lang. Process* **2006**, *14*, 1557.
[109] B. U. Seeber, S. Kerber, E. R. Hafter, *Hear. Res.* **2010**, *260*, 1.
[110] Y. H. Jung, S. K. Hong, H. S. Wang, J. H. Han, T. X. Pham, H. Park, J. Kim, S. Kang, C. D. Yoo, K. J. Lee, *Adv. Mater.* **2020**, *32*, 1904020.
[111] J. Eargle, *Loudspeaker Handbook*, Springer Science & Business Media, Berlin **2003**.
[112] K. Hu, W. Cardenas, Yi-C Huang, H. Wei, R.-E. Gaskell, E. Martel, M. Cerruti, T. Szkopek, *Adv. Funct. Mater.* **2022**, *32*, 2107167.
[113] A. Dehe, G. Ruhl (Infineon Technologies AG), US9516428B2, **2016**.
[114] Q. Zhou, A. K. Zettl ( The Regents of the University of California (Oakland, CA)), US10582305, **2020**.
[115] G. Eda, M. Chhowalla, *Adv. Mater.* **2010**, *22*, 2392.
[116] A. Chavez-Valdez, M. S. P. Shaffer, A. R. Boccaccini, *J. Phys. Chem. B* **2013**, *117*, 1502.
[117] D. W. Lee, T.-K. Hong, D. Kang, J. Lee, M. Heo, J. Y. Kim, B-Su Kim, H. S. Shin, *J. Mater. Chem.* **2011**, *21*, 3438.
[118] H. Li, S. Pang, Si Wu, X. Feng, K. Müllen, C. Bubeck, *J. Am. Chem. Soc.* **2011**, *133*, 9423.
[119] T. Szkopek, K. Hu, W. Cardenas, Y.-C. Huang, H. Wei, R.-E. Gaskell, E. Martel, M. Cerruti, presented at the Electrochemical Society Meeting Abstracts 241, 2022, https://doi.org/10.1149/MA2022-0112850mtgabs.
[120] P. Gaskell, R.-E. Gaskell, T. Szkopek, J. W. Hong, WO2016054723A1, **2016**.
[121] A. Kausar, I. Rafique, B. Muhammad, *Polym.-Plast. Technol. Eng.* **2017**, *56*, 1438.
[122] X. Sun, H. Sun, H. Li, H. Peng, *Adv. Mater.* **2013**, *25*, 5153.
[123] H. Wang, Z. Zhao, P. Liu, X. Guo, *Biosensors* **2022**, *12*, 55.
[124] Wu Lei, W. Si, Y. Xu, Z. Gu, Q. Hao, *Microchim. Acta* **2014**, *181*, 707.
[125] M. Ilami, H. Bagheri, R. Ahmed, E. O. Skowronek, H. Marvi, *Adv. Mater.* **2021**, *33*, 2003139.
[126] R. J. Young, I. A. Kinloch, L. Gong, K. S. Novoselov, *Compos. Sci. Technol.* **2012**, *72*, 1459.
[127] P. Y. Huang, C. S. Ruiz-Vargas, A. M. Van Der Zande, W. S. Whitney, M. P. Levendorf, J. W. Kevek, S. Garg, J. S. Alden, C. J. Hustedt, Ye Zhu, J. Park, P. L. Mceuen, D. A. Muller, *Nature* **2011**, *469*, 389.
[128] B. M. Yoo, H. J. Shin, H. W. Yoon, H. B. Park, *J. Appl. Polym. Sci.* **2014**, *131*, n/a.
[129] K. R. Lee, S. H. Jang, I. Jung, *Nanotechnology* **2018**, *28*, 325502.
[130] A. U. Khan, G. Zeltzer, G. Speyer, Z. L. Croft, Y. Guo, Y. Nagar, V. Artel, A. Levi, C. Stern, D. Naveh, G. Liu, *Adv. Mater.* **2021**, *33*, 2004053.
[131] K. R. Lee, J. Seo, S. S. Kwon, N. Kim, Y. J. Lee, J. G. Son, S. H. Lee, *ACS Appl. Mater. Interfaces* **2023**, *15*, 7319.
[132] H. R. Wang, Z. F. Chen, H. K. A. H.-S. P. M. L. S. B. T. C. P. Xie, *Sens. Actuators, A* **2020**, *309*, 112018.
[133] P. R. Andersen, V. Cutanda Henríquez, N. Aage, J. Kook, *Struct. Multidiscip. Optim.* **2022**, *65*, 343.
[134] M. R. Bai, Ching Yu Liu, Rong Liang Chen, *IEEE Trans. Magn.* **2008**, *44*, 2049.
[135] R. E. I. Schropp, M. Smits, H. Meiling, W. G. J. H. M. Van Sark, M. M. Boone, J. Bezemer, W. F. Van Der Weg, *MRS Online Proc. Libr.* **1991**, *219*, 519.
[136] L. L. Beranek, *J. Acoust. Soc. Am.* **1954**, *26*, 618.

 © 2023 Wiley-VCH GmbH

16163028, 0, Downloaded from https://onlinelibrary.wiley.com/doi/10.1002/adfm.202303519 by Peking University Health, Wiley Online Library on [07/10/2023]. See the Terms and Conditions (https://onlinelibrary.wiley.com/terms-and-conditions) on Wiley Online Library for rules of use; OA articles are governed by the applicable Creative Commons License

[137] X. Guo, Y. Zhang, J. An, Q. Zhang, R. Wang, X. Yu, *Ultrasonics* **2023**, *127*, 106857.
[138] K.-Y. Shin, J.-Y. Hong, J. Jang, *Chem. Commun.* **2011**, *47*, 8527.
[139] A. S. Wixom, M. J. Anderson, D. F. Bahr, D. J. Morris, *Sens. Actuators, A* **2012**, *179*, 204.
[140] Y. K. Xiao, W. F. Ji, K. S. Chang, K. T. Hsu, J. M. Yeh, W.-R. Liu, *RSC Adv.* **2017**, *7*, 33829.
[141] A. L. Kholkin, A. D. Ushakov, M. A. Chuvakova, M. S. Kosobokov, A. R. Akhmatkhanov, A. V. Turutin, M. V. Chichkov, I. I. Kravchenko, Y. Kopelevich, V. Y. Shur, *IEEE Trans. Sonics Ultrason.* **2020**, *67*, 2142.
[142] W. Lee, O. Kahya, C. T. Toh, B. Özyilmaz, J.-H. Ahn, *Nanotechnology* **2013**, *24*, 475202.
[143] Z. Chang, W. Jin, K. S. Chiang, *Opt. Lett.* **2018**, *43*, 1718.
[144] B. Luo, X. Wang, E. Tian, H. Gong, Q. Zhao, Z. Shen, Y. Xu, X. Xiao, L. Li, *ACS Appl. Mater. Interfaces* **2016**, *8*, 3340.
[145] Y. J. Guo, J. Zhang, C. Zhao, P. A. Hu, X. T. Zu, Y. Q. Fu, *Optik* **2014**, *125*, 5800.
[146] M. Lee, J. R. Renshof, K. J. Van Zeggeren, M. J. A. Houmes, E. Lesne, M. Šiškins, T. C. Van Thiel, R. H. Guis, M. R. Van Blankenstein, G. J. Verbiest, A. D. Caviglia, H. S. J. Van Der Zant, P. G. Steeneken, *Adv. Mater.* **2022**, *34*, 2204630.
[147] C. J. Cui, F. Xue, W. J. Hu, L. J Li, *npj 2D Mater. Appl.* **2018**, *2*, 1.
[148] E. J. Mele, P. Král, *Phys. Rev. Lett.* **2002**, *88*, 056803.
[149] W. Wu, L. Wang, Y. Li, F. Zhang, L. Lin, S. Niu, D. Chenet, X. Zhang, Y. Hao, T. F. Heinz, J. Hone, Z. L. Wang, *Nature* **2014**, *514*, 470.
[150] L. J. Sun, X. M. Chen, *Proc. SPIE* **2011**, *8202*, 169.
[151] F. Xue, J. Zhang, W. Hu, W.-T. Hsu, A. Han, S.-F. Leung, J.-K. Huang, Yi Wan, S. Liu, J. Zhang, Jr-H He, W.-H. Chang, Z. L. Wang, X. Zhang, L.-J. Li, *ACS Nano* **2018**, *12*, 4976.
[152] Y. Zhang, W. J. Jie, P. Chen, W. W. Liu, J. H. Hao, *Adv. Mater.* **2018**, *30*, 1707007.
[153] H. Khan, N. Mahmood, A. Zavabeti, A. Elbourne, Md. A Rahman, B. Y. Zhang, V. Krishnamurthi, P. Atkin, M. B. Ghasemian, J. Yang, G. Zheng, A. R. Ravindran, S. Walia, L. Wang, S. P. Russo, T. Daeneke, Y. Li, K. Kalantar-Zadeh, *Nat. Commun.* **2020**, *11*, 3449.
[154] D. C. Tan, C. M. Jiang, N. Sun, J. J. Huang, Z. Zhang, Q, Zhang, B. Jingyuan, S. Bi, Q. Guo, J. Song, *Nano Energy* **2021**, *90*, 106528.
[155] L. Dong, J. Lou, V. B. Shenoy, *ACS Nano* **2017**, *11*, 8242.
[156] V. Hegde, C. David, E. S. Jesseca, S. Nadgouda, S. M. Vrinda, in *Proc. of Int. Conf. on Communication, Circuits, and Systems*, Springer, Berlin **2021**, pp. 215–224, https://doi.org/10.1007/978-981-33-4866-0_27.
[157] H. J. Kim, W. S. Yang, K. No, *IEEE Trans. Sonics Ultrason.* **2012**, *59*, 2027.
[158] Y. Qiao, G. Gou, F. Wu, J. Jian, X. Li, T. Hirtz, Y. Zhao, Y. Zhi, F. Wang, He Tian, Yi Yang, T.-L. Ren, *ACS Nano* **2020**, *14*, 3779.
[159] P. Kumar, R. Sriramdas, A. E. Aliev, J. B. Blottman, N. K. Mayo, R. H. Baughman, S. Priya, *J. Sound Vib.* **2021**, *498*, 115940.
[160] J. W. Suk, K. Kirk, Y. Hao, N. A. Hall, R. S. Ruoff, *Adv. Mater.* **2012**, *24*, 6342.
[161] He Tian, T.-L. Ren, D. Xie, Yu-F Wang, C.-J. Zhou, T.-T. Feng, Di Fu, Yi Yang, P.-G. Peng, Li-G Wang, Li-T Liu, *ACS Nano* **2011**, *5*, 4878.
[162] He Tian, D. Xie, Yi Yang, T.-L. Ren, Yu-F Wang, C.-J. Zhou, P.-G. Peng, Li-G Wang, Li-T Liu, *Nanoscale* **2012**, *4*, 2272.
[163] C. S. Kim, S. K. Hong, J.-M. Lee, D.-S. Kang, B. J. Cho, J.-W. Choi, *Small* **2016**, *12*, 185.
[164] Z. Zhang, He Tian, P. Lv, Yi Yang, Q. Yang, S. Yang, G. Wang, T. Ren, *Appl. Phys. Lett.* **2017**, *110*, 093110.
[165] M. S. Heath, D. W. Horsell, *Stem Cells Int.* **2017**, *7*, https://doi.org/10.1038/s41598-017-01467-z.
[166] He Tian, Yi Yang, C. Li, W.-T. Mi, M. A. Mohammad, T.-L. Ren, *RSC Adv.* **2015**, *5*, 17366.
[167] G.-Y. Gou, M. L. Jin, B.-J. Lee, He Tian, F. Wu, Yu-T Li, Z-Yi Ju, J.-M. Jian, X.-S. Geng, J. Ren, Y. Wei, G-Ya Jiang, Y. Qiao, X. Li, S. J. Kim, M. Gao, H.-T. Jung, C. W. Ahn, Yi Yang, T.-L. Ren, *ACS Nano* **2019**, *13*, 12613.
[168] J. Bush, F. P. McNair, F. J. F. O. DeMetz, L. S. XII, *Proc. SPIE* **1994**, *2292*, 83.
[169] B. Xu, P. C. Zhang, J. K. Zhu, Z. H. Liu, A. Eichler, X.-Q, Zheng, J. Lee, A. Dash, S. More, S. Wu, Y. Wang, H. Jia, A. Naik, A. Bachtold, R. Yang, P. X.-L. Feng, Z. Wang, *ACS Nano* **2022**, *16*, 15545.
[170] S. C. Thompson, J. L. Lopresti, E. M. Ring, H. G. Nepomuceno, J. J. Beard, W. J. Ballad, E. V. Carlson, *J. Acoust. Soc. Am.* **2002**, *111*, 861.
[171] T. Fritsch, D. Beer, J. Küller, G. Fischer, A. Zhykhar, M. Fiedler, in *Microactuators, Microsensors and Micromechanisms*, Springer, Berlin **2021**, pp. 125–136, https://doi.org/10.1007/978-3-030-61652-6_11.
[172] L. D. Fielder, *J. Audio Eng. Soc.* **1995**, *43*, 322.
[173] T. B. Gabrielson, *IEEE Trans. Electron Devices* **1993**, *40*, 903.
[174] H. Li, H. Deng, G. Zheng, M. Shan, Z. Zhong, B. Liu, *Appl. Sci.*. **2019**, *9*, 2241.
[175] D. Todorović, A. Matković, M. Milićević, D. Jovanović, R. Gajić, I. Salom, M. Spasenović, *2D Mater.* **2015**, *2*, 045013.
[176] Yu-M Chen, S.-M. He, C.-H. Huang, C.-C. Huang, W.-P. Shih, C.-L. Chu, J. Kong, Ju Li, C.-Y. Su, *Nanoscale* **2016**, *8*, 3555.
[177] H. M. Mustapha, M. F. M. R. Wee, A. R. M. Zain, M. A. Mohamed, *Sains Malays.* **2019**, *48*, 1201.
[178] G. S. Wood, A. Torin, A. K. Al-Mashaal, L. S. Smith, E. Mastropaolo, M. J. Newton, R. Cheung, A. K. Al-mashaal, L. S. Smith, E. Mastropaolo, *IEEE Sens. J.* **2019**, *19*, 7234.
[179] R. Z. A. HMa, M. A. M. Alia, M. S. Rusdia, *Sci. Eng.* **2016**, *3*, 187.
[180] A. F. Carvalho, A. J. S. Fernandes, M. Ben Hassine, P. Ferreira, E. Fortunato, F. M. Costa, *Appl. Mater.* **2020**, *21*, 100879.
[181] R. Pezone, G. Baglioni, P. M. Sarro, P. G. Steeneken, S. Vollebregt, *ACS Appl. Mater. Interfaces* **2022**, *14*, 21705.
[182] S. Woo, J.-H. Han, J. H. Lee, S. Cho, Ki-W Seong, M. Choi, J-Ho Cho, *ACS Appl Mater Interfaces* **2017**, *9*, 1237.
[183] J. Xu, G. S. Wood, E. Mastropaolo, M. J. Newton, R. Cheung, *ACS Appl. Mater. Interfaces* **2021**, *13*, 38792.
[184] H. Mahdavi, F. Sohbatzadeh, *Philos. Mag.* **2019**, *13*, 165.
[185] J. Erhart, *Phys. Educ.* **2013**, *48*, 438.
[186] A. A. Barlian, W.-T. Park, J. R. Mallon, A. J. Rastegar, B. L. Pruitt, *Proc. IEEE* **2009**, *97*, 513.
[187] S. A. Zawawi, A. A. Hamzah, B. Y. Majlis, *Micromachines* **2020**, *11*, 484.
[188] R. Dieme, G. Bosman, T. Nishida, M. Sheplak, *J. Acoust. Soc. Am.* **2006**, *119*, 2710.
[189] R. Li, Q. Zhang, E. Zhao, J. Li, Q. Gu, P. Gao, *J. Mater. Chem. C* **2019**, *7*, 13032.
[190] B. Wang, B. K. Lee, M. J. Kwak, D. W. G./P. N. S. S. Lee, *Rev. Sci. Instrum.* **2013**, *84*, 105005.
[191] T. Nguyen, T. Dinh, A. R. Md Foisal, H.-P. Phan, T.-K. Nguyen, N.-T. Nguyen, D. V. Dao, *Nat. Commun.* **2019**, *10*, 4139.
[192] E. Caffrey, J. R. Garcia, D. O'suilleabhain, C. Gabbett, T. Carey, J. N. Coleman, *ACS Appl. Mater. Interfaces* **2022**, *14*, 7141.
[193] Q. Zheng, J.-H. Lee, Xi Shen, X. Chen, J.-K. Kim, *Mater. Today* **2020**, *36*, 158.
[194] E. Ricohermoso, F. Rosenburg, F. Klug, N. Nicoloso, H. F. Schlaak, R. Riedel, E. Ionescu, *Open Ceram.* **2021**, *5*, 100057.
[195] A. D. Smith, F. Niklaus, A. Paussa, S. Vaziri, A. C. Fischer, M. Sterner, F. Forsberg, A. Delin, D. Esseni, P. Palestri, M. Ostling, M. C. Lemme, *Nano Lett.* **2013**, *13*, 3237.
[196] M. Huang, T. A. Pascal, H. Kim, W. A. Goddard, J. R. Greer, *Nano Lett.* **2011**, *11*, 1241.
[197] Yi Wang, R. Yang, Z. Shi, L. Zhang, D. Shi, E. Wang, G. Zhang, *ACS Nano* **2011**, *5*, 3645.


© 2023 Wiley-VCH GmbH

16163028, 0, Downloaded from https://onlinelibrary.wiley.com/doi/10.1002/adfm.202303519 by Peking University Health, Wiley Online Library on [07/10/2023]. See the Terms and Conditions (https://onlinelibrary.wiley.com/terms-and-conditions) on Wiley Online Library for rules of use; OA articles are governed by the applicable Creative Commons License

[198] R. Frisenda, M. Drüppel, R. Schmidt, S. Michaelis De Vasconcellos, D. Perez De Lara, R. Bratschitsch, M. Rohlfing, A. Castellanos-Gomez, *npj 2D Mater. Appl.* **2017**, *1*, 10.
[199] H. Liu, Q. M. Li, S. D. Zhang, R. Yin, X. H. Liu, Y. He, K. Dai, C. Shan, J. Guo, C. Liu, C. Shen, X. Wang, N. Wang, Z. Wang, R. Wei, Z. Guo, *J. Mater. Chem. C* **2018**, *6*, 12121.
[200] P. Zhang, R. Jia, Ke Tao, S. Jiang, X. Dai, H. Sun, Z. Jin, Z. Ji, X. Liu, C. Zhao, H. Liu, Y. Zhao, L. Tang, *Sol. Energy Mater. Sol. Cells* **2019**, *200*, 109983.
[201] W. Dong, W. Li, Z. Tao, K. Wang, *Constr. Build. Mater.* **2019**, *203*, 146.
[202] Yi Yang, Y. Wei, Z. Guo, W. Hou, Y. Liu, He Tian, T.-L. Ren, *Small Methods* **2022**, *6*, 2200671.
[203] J. Han, M. Saravanapavanantham, M. R. Chua, J. H. Lang, V. Bulović, *Microsyst. Nanoeng.* **2022**, *8*, 55.
[204] S. C. Ko, Y. C. Kim, S. S. Lee, S. H. Choi, S. R. Kim, *Sens. Actuators, A* **2003**, *103*, 130.
[205] S. Wang, He-Q Shao, Y. Liu, C.-Y. Tang, X. Zhao, K. Ke, R.-Y. Bao, M-Bo Yang, W. Yang, *Compos. Sci. Technol.* **2021**, *202*, 108600.
[206] J. Kwon, W. Seung, B. K. Sharma, S.-W. Kim, J.-H. Ahn, *Environ. Sci.* **2012**, *5*, 8970.
[207] J. S. Lee, K.-Y. Shin, O. J. Cheong, J. H. Kim, J. Jang, *Stem Cells Int.* **2015**, *5*, 7887.
[208] X. R. Wang, K. Yasuda, Y. Zhang, S. Liu, K. Watanabe, T. Taniguchi, J. Hone, L, Fu, P. Jarillo-Herrero, *Nat. Nanotechnol.* **2022**, *17*, 367.
[209] K. Yasuda, X. R. Wang, K. Watanabe, T. Taniguchi, P. Jarillo-Herrero, *Science* **2021**, *372*, 1458.
[210] C. Li, X. Gao, T. Guo, J. Xiao, S. Fan, W. Jin, *Meas. Sci. Technol.* **2015**, *26*, 085101.
[211] D. Davidovikj, J. J. Slim, S. J. Cartamil-Bueno, H. S. J. Van Der Zant, P. G. Steeneken, W. J. Venstra, *Nano Lett.* **2016**, *16*, 2768.
[212] J. Zhu, Bo Xu, F. Xiao, Y. Liang, C. Jiao, J. Li, Q. Deng, S. Wu, T. Wen, S. Pei, J. Xia, Z. Wang, *Nano Lett.* **2022**, *22*, 5107.
[213] Z. Zelinger, P. Janda, J. Suchánek, M. Dostál, P. Kubát, V. Nevrlý, P. Bitala, S. Civiš, *J. Sens. Sens. Syst.* **2015**, *4*, 103.
[214] G. Baglioni, R. Pezone, S. Vollebregt, K. Cvetanović Zobenica, M. Spasenović, D. Todorović, H. Liu, G. J. Verbiest, H. S. J. Van Der Zant, P. G. Steeneken, *Nanoscale* **2023**, *15*, 6343.
[215] Y. Zhang, Ph. D. Thesis, Brunel University London **2018**.
[216] M. Johansmann, G. Siegmund, M. Pineda, in *Proc. IDEMA*, **2005**, pp. 1–12.
[217] F. S. Irani, A. H. Shafaghi, M. C. Tasdelen, T. Delipinar, C. E. Kaya, G. G. Yapici, M. K. Yapici, *Micromachines* **2022**, *13*, 119.
[218] W. J. Yan, H. R. Fuh, Y. H. Lv, K. Q. Chen, T. Y. Tsai, Y.-R. Wu, T.-H. Shieh, K.-M. Hung, J. Li, D. Zhang, C. Ó. Coileáin, S. K. Arora, Z. Wang, Z. Jiang, C.-R. Chang, H.-C. Wu, *Nat. Commun.* **2021**, *12*, 2018.
[219] S. Manzeli, A. Allain, A. Ghadimi, A. Kis, *Nano Lett.* **2015**, *15*, 5330.
[220] A. Tarasov, M. Y. Tsai, H. Taghinejad, P. M. Campbell, A. Adibi, E. M. Vogel, *2015 73rd Annual Device Research Conf. (DRC)*, IEEE, Piscataway, NJ **2015**, pp. 159–160, https://doi.org/10.1109/DRC.2015.7175604.
[221] M. Hosseini, M. Elahi, M. Pourfath, D. Esseni, *Appl. Phys. Lett.* **2015**, *107*, 253503.
[222] D. Maier-Schneider, J. Maibach, E. Obermeier, *J. Microelectromech. Syst.* **1995**, *4*, 238.
[223] P. Gonzalez, M. Rakowski, D. San Segundo, S. Severi, K. De Meyer, A. Witvrouw, *IEEE Electron Device Lett.* **2012**, *33*, 1204.
[224] I. V. Godovitsyn, V. V. Amelichev, V. V. Pankov, *Sens. Actuators, A* **2013**, *201*, 274.
[225] A. D. Smith, F. Niklaus, S. Vaziri, A. C. Fischer, M. Sterner, A. Witvrouw, *2014 IEEE 27th Int. Conf. on Micro Electro Mechanical Systems (MEMS)*, IEEE, Piscataway, NJ **2014**, p. 1055, https://doi.org/10.1109/MEMSYS.2014.6765826.
[226] S-En Zhu, M. Krishna Ghatkesar, C. Zhang, G. C. A. M. Janssen, *Appl. Phys. Lett.* **2013**, *102*, 161904.
[227] Q. Wang, W. Hong, L. Dong, *Nanoscale* **2016**, *8*, 7663.
[228] X. Lin, Y. Liu, Y. Zhang, P. Yang, X. Cheng, J. Qiu, G. Liu, *Nano* **2019**, *14*, 1950130.
[229] Y. Liu, Y. Zhang, X. Lin, K. H. Lv, P. Yang, J. Qiu, G. Liu, *Micromachines* **2020**, *11*, 786.
[230] S. Wagner, C. Yim, N. Mcevoy, S. Kataria, V. Yokaribas, A. Kuc, S. Pindl, C.-P. Fritzen, T. Heine, G. S. Duesberg, M. C. Lemme, *Nano Lett.* **2018**, *18*, 3738.
[231] F. Xu, J. Shi, K. Gong, H. Li, R. Hui, B. Yu, *Opt. Lett.* **2014**, *39*, 2838.
[232] J. Ma, W. Jin, H. L. Ho, J. Y. Dai, *Opt. Lett.* **2012**, *37*, 2493.
[233] J. Ma, H. Xuan, H. L. Ho, W. Jin, Y. Yang, S. Fan, *IEEE Photonics Technol. Lett.* **2013**, *25*, 932.
[234] C. Li, Q. W. Liu, T. T. Guo, J. Xiao, S. C. Fan, J. Wei, in *IEEE Sensor*, IEEE, Piscataway, NJ **2015**, p. 567, https://doi.org/10.1109/ICSENS.2015.7370318.
[235] S. L. Liao, T. Wong, Z. Wang, R. Wang, E. Clutter, H. T. Chien, *2018 IEEE Research and Applications of Photonics in Defense Conf. (Rapid)*, IEEE, Piscataway, NJ **2018**, p. 197, https://doi.org/10.1109/RAPID.2018.8508963.
[236] C. Li, J. Xiao, T. T. Guo, S. C. Fan, W. Jin, *Mater. Res. Innovations* **2015**, *19*, 17.
[237] F. Yu, Q. Liu, X. Gan, M. Hu, T. Zhang, C. Li, F. Kang, M. Terrones, R. Lv, *Adv. Mater.* **2017**, *29*, 1603266.
[238] Q. Dong, H. Bae, Z. Zhang, Y. Chen, Z. Wen, D. A. Olson, M. Yu, H. Liu, *J. Vib. Acoust.* **2019**, *141*, 041003.
[239] C. S. Monteiro, M. Raposo, P. A. Ribeiro, S. O. Silva, O. Frazão, *Sensors* **2021**, *21*, 2336.
[240] J. Han, M. A. Shannon, *IEEE Sens. J.* **2009**, *9*, 199.
[241] D. Davidovikj, P. H. Scheepers, H. S. J. Van Der Zant, P. G. Steeneken, *ACS Appl. Mater. Interfaces* **2017**, *9*, 43205.
[242] Q. C. Tran, C. C. Gao, Y. L. Hao, in *Int. Conf. Nano Micro*, **2017**, p. 526, https://doi.org/10.1109/NEMS.2017.8017077.
[243] M. Šiškins, M. Lee, D. Wehenkel, R. Van Rijn, T. W. De Jong, J. R. Renshof, B. C. Hopman, W. S. J. M. Peters, D. Davidovikj, H. S. J. Van Der Zant, P. G. Steeneken, *Microsyst. Nanoeng.* **2020**, *6*, 102.
[244] C. Berger, R. Phillips, A. Centeno, A. Zurutuza, A. Vijayaraghavan, *Nanoscale* **2017**, *9*, 17439.
[245] C. Berger, R. Phillips, I. Pasternak, J. Sobieski, W. Strupinski, A. Vijayaraghavan, *2D Mater.* **2018**, *5*, 015025.
[246] S. Ban, X. Nie, Z. Lei, J. Yi, A. Vinu, Y. Bao, Y. Liu, *Mater. Res. Lett.* **2023**, *11*, 21.
[247] C. Chen, S. Rosenblatt, K. I. Bolotin, W. Kalb, P. Kim, I. Kymissis, H. L. Stormer, T. F. Heinz, J. Hone, *Nat. Nanotechnol.* **2009**, *4*, 861.
[248] B. Arash, Q. Wang, W. H. Duan, *Phys. Lett. A* **2011**, *375*, 2411.
[249] P. Weber, J. Güttinger, A. Noury, J. Vergara-Cruz, A. Bachtold, *Nat. Commun.* **2016**, *7*, 12496.
[250] J. S Bunch, A. M. Van Der Zande, S. S. Verbridge, I. W. Frank, D. M. Tanenbaum, J. M. Parpia, H. G. Craighead, P. L. Mceuen, *Science* **2007**, *315*, 490.
[251] Xu-Q Zheng, J. Lee, P. X.-L. Feng, *Microsyst. Nanoeng.* **2017**, *3*, 17038.
[252] R. Yang, Z. H. Wang, P. X. L. Feng, in *Joint Conf. of the IEEE Int. Frequency Control Symp. & the European Frequency and Time Forum (Fcs)*, IEEE, Piscataway, NJ **2015**, pp. 198–201, https://doi.org/10.1109/FCS.2015.7138822.
[253] F. Ye, J. Lee, P. X. L. Feng, paper presented at the 2018 IEEE Int. Electron Devices Meeting (IEDM), December **2018**, https://doi.org/10.1109/IEDM.2018.8614604.
[254] F. Ye, J. Lee, P. X.-L. Feng, *Nano Lett.* **2018**, *18*, 1678.
[255] A. Islam, J. Lee, P. X. L. Feng, in *Proc IEEE Micro Electro*, IEEE, Piscataway, NJ **2020**, p. 826, https://doi.org/10.1109/MEMS46641.2020.9056366.

 © 2023 Wiley-VCH GmbH

16163028, 0, Downloaded from https://onlinelibrary.wiley.com/doi/10.1002/adfm.202303519 by Peking University Health, Wiley Online Library on [07/10/2023]. See the Terms and Conditions (https://onlinelibrary.wiley.com/terms-and-conditions) on Wiley Online Library for rules of use; OA articles are governed by the applicable Creative Commons License

[256] J. Lee, M. J. Krupcale, P. X.-L. Feng, *Appl. Phys. Lett.* **2016**, *108*, 023106.
[257] R. J. Dolleman, M. Hsu, S. Vollebregt, J. E. Sader, H. S. J. Van Der Zant, P. G. Steeneken, M. K. Ghatkesar, *Appl. Phys. Lett.* **2019**, *115*, 053102.
[258] H.-L. Lee, Yu-C Yang, W.-J. Chang, *Jpn. J. Appl. Phys.* **2013**, *52*, 025101.
[259] I. B. Baek, S. Byun, B. K. Lee, J. H. Ryu, Y. Kim, Y. S. Yoon, W. I. Jang, S. Lee, H. Y. Yu, *Stem Cells Int.* **2017**, *7*, 46660.
[260] S. A Fazelzadeh, E. Ghavanloo, *Acta Mech. Sin.* **2014**, *30*, 84.
[261] D. Karličić, P. Kozić, S. Adhikari, M. Cajić, T. Murmu, M. Lazarević, *Int. J. Mech. Sci.* **2015**, *96–97*, 132.
[262] T. Natsuki, J.-X. Shi, Q.-Q. Ni, *J. Appl. Phys.* **2013**, *114*, 094307.
[263] M. D. Dai, C.-W. Kim, K. Eom, *Nanoscale Res. Lett.* **2012**, *7*, 499.
[264] X. Xiao, S. C. Fan, C. Li, *Micromachines* **2021**, *12*, 189.
[265] Xiao, Fan, Li, Xing,, *Sensors* **2019**, *19*, 3027.
[266] J. Lee, P. X. L. Feng, in *Proc. IEEE Int. Frequency Control Symp.*, IEEE, Piscatawaway, NJ, **2014**, p. 276, https://doi.org/10.1109/FCS.2014.6859918.
[267] R. J. Dolleman, D. Davidovikj, S. J. Cartamil-Bueno, H. S. J. Van Der Zant, P. G. Steeneken, *Nano Lett.* **2016**, *16*, 568.
[268] R. Yang, Z. Wang, P. X.-L. Feng, in *Joint Conf. of the IEEE Int. Frequency Control Symp. & the European Frequency and Time Forum*, IEEE, Piscataway, NJ **2015**, pp. 198–201, https://doi.org/10.1109/FCS.2015.7138822.
[269] F. Ye, J. Lee, P. X.-L. Feng, in *2018 IEEE Int. Electron Devices Meeting (IEDM)*, IEEE, Piscataway, NJ **2018**, pp. 4.4.1–4.4.4, https://doi.org/10.1109/IEDM.2018.8614604.
[270] J. Lee, M. J. Krupcale, P. X.-L. J. A. P. L. Feng, *Appl. Phys. Lett.* **2016**, *108*, 023106.
[271] H. Lei, Y. Chen, Z. Gao, Z. Wen, X. Sun, *J. Mater. Chem. A* **2021**, *9*, 20100.
[272] M. Sang, J. Shin, K. Kim, Ki Yu, *Nanomaterials* **2019**, *9*, 374.
[273] Y. Xiao, F. Luo, Y. C. Zhang, F. Hu, M. J. Zhu, S. Q. Qin, *Micromachines* **2022**, *13*, 215.
[274] Y. Qiu, J. Gigliotti, M. Wallace, F. Griggio, C. Demore, S. Cochran, S. Trolier-Mckinstry, S. Qin, *Sensors* **2015**, *15*, 8020.
[275] H. Nazemi, J. A. Balasingam, S. Swaminathan, K. Ambrose, M. U. Nathani, T. Ahmadi, Y. B. Lopez, A. Emadi, *Sensors* **2020**, *20*, 2010.
[276] D. E. Dausch, K. H. Gilchrist, J. B. Carlson, S. D. Hall, J. B. Castellucci, O. T. Von Ramm, *IEEE Trans. Sonics Ultrason.* **2014**, *61*, 1754.
[277] Po-F Chong, X. Shi, C.-H. Cheng, *Micro Nano Lett.* **2014**, *9*, 884.

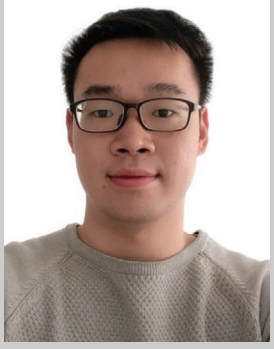

**Zhaoyi Wan** is currently pursuing his Doctoral degree at the International Centre for Quantum Materials, Peking University, China. He received his Bachelor's degree from Northwestern Polytechnical University, China in 2021. His research interests lie in spectral physics and nonlinear optics of 2D materials as well as their acoustic devices.

**Huazhan Liu** received his B.S. degree from Nanjing University in 2022. Now he is a Ph.D candidate under the supervision of Prof. Kaihui Liu in School of Physics, Peking University Beijing, China. His research interests mainly focus on the optical properties of low-dimensional materials and their applications in acoustic devices.


© 2023 Wiley-VCH GmbH

16163028, 0, Downloaded from https://onlinelibrary.wiley.com/doi/10.1002/adfm.202303519 by Peking University Health, Wiley Online Library on [07/10/2023]. See the Terms and Conditions (https://onlinelibrary.wiley.com/terms-and-conditions) on Wiley Online Library for rules of use; OA articles are governed by the applicable Creative Commons License

**Yuebin Zheng** is currently a joint postdoctoral fellow at Institute of Physics, Chinese Academy of Sciences and Songshan Lake Materials Laboratory. He obtained his Ph.D. degree from Dalian University of Technology in 2021. His main research interests are graphene and other 2D materials-based technologies aims at developing next-generation acoustic sensors. He also has got a vast background in acoustic-based Structural Health Monitoring.

**Yuhua Ma** received his B.S. degree from Hunan Normal University in 2017, and is currently engaged in master's level research at South China Normal University. His main research interests include 2D materials physics and device physics.

**Xu Zhou** is currently an associate professor at the School of Physics, South China Normal University, China. He received his B.S. degree from Northwestern Polytechnical University in 2014 and his Ph.D. degree from Peking University in 2018, followed by his postdoctoral research in Peking University until 2020. His research interests mainly focus on the physics and device physics of 2D materials.

**Chang Liu** is currently a postdoctoral research fellow in the International Center for Quantum Materials, School of Physics, Peking University, China. He received his B.S. degree from Xi'an Jiaotong University in 2016 and his Ph.D. degree from Peking University in 2021. His research interests mainly focus on the spectral physics and nonlinear optics of 2D materials and their acoustic devices.



© 2023 Wiley-VCH GmbH

16163028, 0, Downloaded from https://onlinelibrary.wiley.com/doi/10.1002/adfm.202303519 by Peking University Health, Wiley Online Library on [07/10/2023]. See the Terms and Conditions (https://onlinelibrary.wiley.com/terms-and-conditions) on Wiley Online Library for rules of use; OA articles are governed by the applicable Creative Commons License

**Kaihui Liu** is currently a professor at the State Key Lab for Mesoscopic Physics, School of Physics, Peking University, China. He received his B.S. degree from Beijing Normal University and his Ph.D. degree from the Institute of Physics, Chinese Academy of Sciences in 2009. Afterward he worked as a postdoctoral fellow at UC Berkeley, USA, until 2014. His current research interests are the growth and device physics of meter-scale single crystals including single-crystal copper foils, graphene, BN, TMDCs, and 2D materials-optical fiber.



© 2023 Wiley-VCH GmbH

16163028, 0, Downloaded from https://onlinelibrary.wiley.com/doi/10.1002/adfm.202303519 by Peking University Health, Wiley Online Library on [07/10/2023]. See the Terms and Conditions (https://onlinelibrary.wiley.com/terms-and-conditions) on Wiley Online Library for rules of use; OA articles are governed by the applicable Creative Commons License